ABSTRACT

Title of Dissertation: ATOMISTIC EXPLORATION OF DENSELY-GRAFTED POLYELECTROLYTE BRUSHES: EFFECT OF APPLIED ELECTRIC FIELD AND MULTIVALENT SCREENING COUNTERIONS

Md. Turash Haque Pial, Doctor of Philosophy, 2022

Dissertation directed by: Professor Siddhartha Das, Department of Mechanical Engineering, University of Maryland.

Polyelectrolyte (PE) or charged polymers are ubiquitous under biological and synthetic conditions, ranging from DNA to advanced technologies. PE chains can be grafted on a surface and they extend into solution to form a "brush"-like configuration if the grafting density is high. PE brushes respond to external stimuli by changing their conformation and chemical details, which make them very attractive for numerous applications. Multivalent counterions (neutralizing PE charges) and external electric fields are known to significantly affect the brush behavior. Obtaining fundamental insights into PE brush's response to ions and electric filed is of utmost importance for both industrial and academic research. In this dissertation, we use atomistic tools to improve our understanding of the PE brushes grafted on a single surface and two inner walls of a nanochannel under these two stimuli.

We start by developing an all-atom molecular dynamics simulation framework to test the behavior of the PE brushes (grafted on a single surface) in the presence of externally applied electric fields. It is discovered that the charge density of PE monomers can have significant influence on their response; a smaller monomer charge density helps the brush to tilts along the electric field, while the PE brush with higher monomer charge density bends and shrinks. We

found that counterion condensation to PE chains has a substantial impact in controlling these responses.

In the subsequent study we discuss the effect of counterion size and valence in dictating counterion mediated bridging interaction of two or more negative monomers. By examining the solvation behavior, we identify that bridging interactions are not a sole function of the counterion valence. Rather, it depends on the counterion condensation on the PE chain, as well as the size of the counterion solvation shell. We also test the dynamic properties of the counterions and associated bridges.

Later, we proceeded to simulate PE brush-grafted nanochannels to explore equilibrium and flow behavior in presence of nanoconfinement. We identify the onset of overscreening: there are a greater number of coions than counterions in the bulk liquid outside the brush layer. This specific ion distribution ensures that the overall electroosmotic flow is along the direction of the coions. Furthermore, for a large electric field, some of the counterions leave the PE brush layer into the bulk, resulting in disappearance of overscreening. If the number of counterions is greater than coions, electroosmotic flow reverses its direction and follows the motion of counterions. Finally, we discover that counterion-monomer interactions control the ion distribution. As a result, a diverse range of electroosmotic flow is found for counterions with different valence and size.

ATOMISTIC EXPLORATION OF DENSELY-GRAFTED POLYELECTROLYTE BRUSHES: EFFECT OF APPLIED ELECTRIC FIELD AND MULTIVALENT SCREENING COUNTERIONS

by

Md. Turash Haque Pial

Dissertation submitted to the Faculty of the Graduate School of the
University of Maryland, College Park, in partial fulfillment
of the requirements for the degree of
Doctor of Philosophy
2022

Advisory Committee:
Professor Siddhartha Das, Chair
Professor Peter W. Chung
Professor Amir Riaz
Professor Pratyush Tiwary
Professor Yifei Mo, Dean's Representative

© Copyright by
Md. Turash Haque Pial
2022

Dedication

আম্মুকে

Acknowledgements

This work has been supported by the Department of Energy Office of Science grant DE-SC0017741. I am thankful for the computational support obtained from the Deepthought2 High-Performance Computing cluster at the University of Maryland.

Table of Contents

List of Abbreviations

Polyelectrolyte (PE)

Molecular Dynamics (MD)

Coarse-grained Molecular Dynamics (CGMD)

Electroosmotic (EOS)

Overscreening (OS)

Poly (acrylic acid) (PAA)

Poly (methacrylic acid) (PMAA)

Poly (styrene sulfonate) (PSS)

Particle-Particle Particle-Mesh (PPPM)

Cumulative Distribution Function (CDF)

Electric Double Layer (EDL)

Excluded Volume (EV)

Radial Distribution Function (RDF)

Mean Squared Displacement (MSD)

Lennard-Jones (LJ)

List of Figures

List of Tables

Chapter 1: Background and Motivation

1.1 Overview

Polyelectrolyte (PE) is one of the most important components of our existence since the beginning of life on earth [1]. It is a charged polymer that contains all of our biological information, namely DNA and RNA. With the advancement of human cognitive ability, we ourselves have learnt to create different forms of PEs for our own essential and auxiliary use. Now we know how to modify the behavior of these PEs, how to incorporate them into our medicine, devices, structures, etc. Despite such progress, there is still a significant dearth of understanding and lot of open questions on the complex morphological, chemical, and physical behaviors of different types of PEs. A better understanding of these open questions will be possible with detailed knowledge at the atomistic scale, which is the primary aspiration of this doctoral thesis.

The PE chain contains a charged monomer that can be grafted onto a surface. Depending on the grafting density, type of monomer, and the property of the solution, the grafted chains can behave differently. If the grafting density is high or the chains are very close to each other, they sense the presence of nearby chains and stretch out into the solution. PE chains in such stretched-out configurations are referred to as PE "brush" [2]. A schematic of a PE brush layer, grafted to a planar surface, is shown in Figure 1.1 (a). It is also possible to graft two opposing layers of brushes within a nanochannel [see figure 1.1 (b)]. In this dissertation, these two systems will be understood using an extremely powerful computational tool, namely all-atom molecular dynamics (MD) simulation.

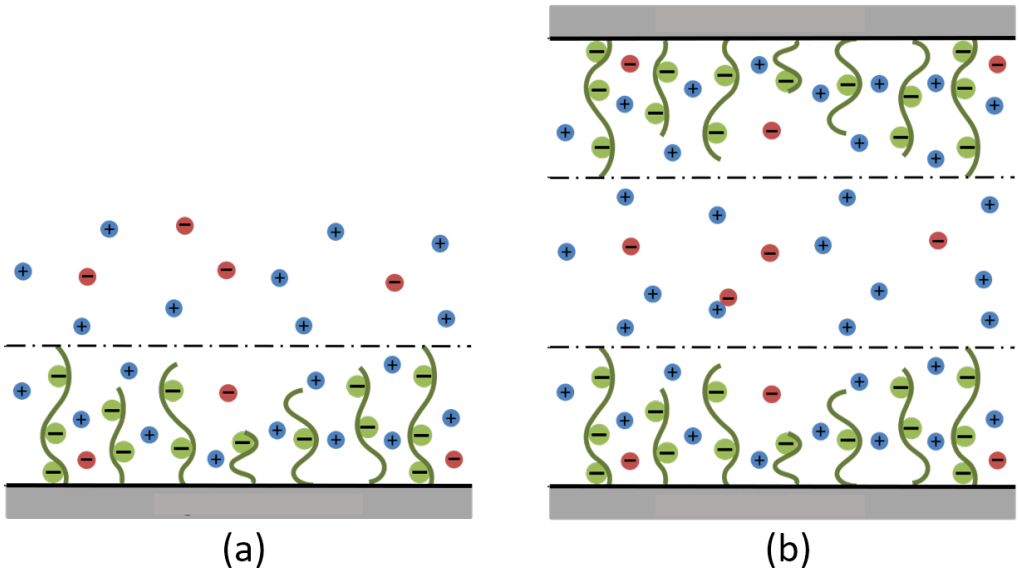

Figure 1.1. Cartoon visualization of the PE brush grafted on a single surface **(**a), and on two inner walls of a nanochannel (b).

Molecular dynamics (MD) simulations employ the Newton's equations of motion to atoms or group of atoms to understand the molecular level behavior. To simplify the calculation and reduce the associated cost required to perform the calculations, coarse-graining of a group atoms can be done. Problem with this coarse-graining is that we lose important information by not taking care of each atom separately. All-atom MD simulations can overcome this challenge; however, the field of PE has not been probed much with all-atom MD simulations. In this dissertation, the behavior of the PE brush grafted to a single surface, and grafted on the opposites surfaces of a nanochannel will be explored. In particular, the effect of multivalent screening counterion and salt, and applied electric field will be investigated.

1.2 Polyelectrolyte Brushes Grafted on a Surface: Effect of Multivalent Counterions and Electric Field

Polyelectrolytes (PEs) are polymers whose repeating unit is an electrolyte. PE chains are ubiquitous: from our very own nucleic acids [2], the articular cartilage and the mineralized collagen in bone [3,4] to those contributing to an overwhelming number of applications in energy [5], sensing [6,7], gene and drug delivery [8,9], oil recovery [10], water harvesting [11], wound healing [12], and many more. PE brushes, on the other hand, have been employed in a myriad of applications such as electrokinetic energy conversion [2], biosensing [13,14], drug delivery [15,16], oil recovery [17], water harvesting [18] etc. The wide-spread use of PE brushes is due to their capability to respond to the changes in the surrounding medium like bulk salt concentration and type, pH, solvent quality, temperature, external applied field, etc. Therefore, it is vital to understand the thermodynamics and response of such PE brush systems in finer details.

PE brush conformation and several of their applications are affected by the applied electric field. Electric field influences the conformation of PE systems which in turn can be used to control lubricity, soft devices' motion, layer-by-layer assembly, etc [19-26]. PE charge density should play a major role in dictating the response of the PE to an applied electric field as electrostatic forces on charged atoms depends on their charge content. Although crucially important, an effort to understand the charge density dependent response has been missing either in experimental or simulation-based approaches because of the atomistic nature of the research question [27-30]. In chapter 2, we have discussed all-atom simulations of PE brush grafted system under axial electric field. We have simulated two different PEs with different monomers to understand the effect of monomer charge density on the brush conformational change. From atomistic data, the mechanism important manipulate the local structure and the overall PE brush configuration is discussed.

Ion specific effects, namely the effects dictated by the sizes and valences of these ions, are

found to be very important in different PE systems. For example, coarse-grained (CG) molecular dynamics (MD) simulations show that smaller ions lead to more compact PE structure [31,32]. On the contrary, recent experiments on PE brushes demonstrated that larger divalent screening counterions lead to smaller PE brush height [33,34]. PE brush layers are found to collapse in the presence of multivalent counterions as a result of the "bridging" interactions, while such collapse does not occur for the case of monovalent counterions [33,34]. On the contrary, there are also studies that report favorable "bridging" like interactions between like-charged systems even in presence of monovalent counterions [35,36]. These discrepancies necessitate the atomistic exploration for understanding the PE-ion interactions and pinpoint the importance of the ion valance and size. In chapter 3, with the help of all-atom MD simulations, the effect of counterions valance and size is discussed. It is found that monovalent counterions can also form "bridging" interactions. Mechanism of this interactions are identified.

1.3 Brushes Grafted on a Nanochannel: Brush Behavior and Electroosmotic Transport in Presence of Multivalent Counterions and Applied Electric Field

Technological advances make it possible for tailoring nanochannels for specific uses. One of the most promising tailoring methods is grafting PE brushes on the inner walls of a nanochannel, with possible applications in fabricating artificial cartilage and nano- and micro-diode as well as in sensing, current rectification, etc [2]. By applying an external electric field to drive the ion-containing (electrolyte) liquids, electroosmotic (EOS) flow can be generated in a nanochannel. In some applications, the direction of EOS flow inside the nanochannel needs to be manipulated in a way that enhances mixing, reaction, separation, and printing [37-41]. The resulting changes in the morphology of the brushes and the associated ion distribution can significantly influence the EOS transport in brush-grafted nanochannels, which can also modify the EOS flow directions. Despite

its tremendous potential, only a few simplified continuum studies [42,43], and a handful of MD simulation studies are available for probing the liquid transport in brush-grafted nanochannels [44-46]. In chapter 4, by using all-atoms MD simulations, it is discovered that nanochannel grafted with PE brushes can enable modifying EOS flow direction just by changing the electric field strength. The atomistic details of the flow as well as brush-ion-water behavior are also discussed.

A charged surface can control the ion distributions in nearby solution [154]. When electrolytes come near a charged surface, free ions from the electrolyte try to neutralize the surface charge and form distinctive ion layer near charged surface [154]. If electrolyte ions are multivalent, there can be an overcompensation of this screening of the surface charge, that results in a charge inversion near the charged surface. This overcompensation caused by the multivalent counterions is known overscreening (OS). These ion distribution near charged surface also has the potential to modify the EOS flow in a nanochannel [155]. In chapter 5, we first probe the equilibrium ion distribution in a nanochannel grafted with PE brushes, where counterions with various valences and sizes neutralize the PE charges. We then apply external electric field and predict the EOS flow for cases where different counterions screen the PE brush charge.

Finally, in chapter 6, we summarize the key findings of this dissertation and end with a discussion of several future problems that can be solved for making further progress in developing our atomistic level understanding of the responses of the PE brushes to different external stimuli.

Chapter 2: Charge-Density-Specific Response of Grafted Polyelectrolytes to Electric Fields: Bending or Tilting?*

Abstract: *Response of polyelectrolytes (PEs) to applied electric fields drive applications in energetics, diagnostics, materials development, and many more. Here we employ all-atom molecular dynamics (MD) simulations to probe the response of grafted PE brushes to axial electric fields. For PEs with large charge densities, the electric field triggers a left-right asymmetric distribution of counterions around the PE backbone: consequently, depending on the location (left or right), there is an unequal screening and an unequal force on the PE functional groups causing a bending-driven brush height reduction. However, for the weakly charged PEs, the electric field causes a uniform distribution of the counterions across the brush enforcing a uniform (without left-right asymmetry) partially unscreened PE brush: therefore, all the brush segments experience similar force causing a brush tilting-driven brush height reduction. Such bending versus tilting responses is commensurate with the electric-field-driven increase (decrease) in the flexibility of strongly (weakly) charged PEs.*

*Contents of this chapter is published as Pial, T. H.; Prajapati, M.; Chava, B. S.; Sachar, H. S.; Das, S. Charge-Density-Specific Response of Grafted Polyelectrolytes to Electric Fields: Bending or Tilting? *Macromolecules* **2022**, DOI: 10.1021/acs.macromol.2c00237.

2.1 Introduction

Polyelectrolyte (PE) molecules, when densely grafted, occupy "brush"-like configurations. Such PE brushes are present in biological interfaces like articular cartilage, mineralized collagen in bone, etc. [3,4]. In terms of engineering applications, synthetic nanochannels grafted with PE brushes, in presence of applied electric fields, can be used as nanofluidic ionic circuits, nanofluidic sensors, and flow controlling devices and gates [48-52]. All these applications rely on the manner in which the applied electric field affects the distribution of the ions around the PE brushes (these ions are typically those that are screening the PE brush charges) and the resulting alterations in the behavior/configurations of the PE brushes. The electric-field-mediated changes in the brush configuration/orientation influence the lubrication action of interpenetrating PE brush bilayer [19,20], trigger a layer-by-layer assembly of grafted PE system [21-23], and possible soft robotics application [24-26].

These applications make it fundamentally important to develop a precise atomistic-level understanding on the manner in which the imposed electric field affects the behavior of the charged monomers of the PE, the counterions screening the charges of these monomers, and the water molecules present within the solvation shell of the PE monomer and the counterions, and the manner in which the variation in the PE charge density affects these behaviors. Such precise, atomistically-resolved understanding, unfortunately, has been missing either in experimental (often limited by its scale [27]) or simulation-based (employing coarse-grained methods [28-30]) approaches that have so far been employed to study the electric-field-response of the PE brush molecules. There are only a handful of related all-atom simulation studies for PE molecules (non-brush systems [53]) and new insight, to be revealed by all-atom MD simulations, is needed for better understanding the responses of PE brush molecules to external electric fields.

In this chapter, we bridge this knowledge gap: we employ all-atom molecular dynamics (MD) simulations and study the responses of densely grafted poly (acrylic acid) (PAA) and poly (styrene sulfonate) (PSS) brushes to axial electric field. These two PE molecules vary significantly in terms of their charge densities. Therefore, our study seeks answer to the following questions: What is the charge-density-dependent electric-field response of PE brush molecules and how well-resolved atomistic simulations can capture such responses and the associated responses of the PE brush supported counterions and solvent molecules? Our all-atom MD simulations, in the process of answering these questions, lead to the following key discovery: we discover that the significant disparity in the charge densities of these two PEs (PAA and PSS) leads to massively varied responses of the corresponding PE-counterion complex to the electric field and the result is a bending-induced and a tilting-induced brush height reduction for the PAA and PSS brushes, respectively. Such responses are also commensurate with the disparate electric-field-induced changes in the intrinsic flexibilities of these two PE systems. Our findings will be significant in a vast number of applications that rely on enforcing a particular configuration of the PE system (e.g., friction reduction [47,54,55]) or on the specifics of the response of the PEs to the applied electric field (e.g., fabrication of electrically-responsive soft devices [24-26]).

2.2 Results and Discussion

Our all-atom MD simulation system consists of densely grafted fully ionized poly (acrylic acid) (PAA), poly (methacrylic acid) (PMAA), and poly (styrene sulfonate) (PSS) brushes. Na^+ counterions are added to neutralize the PE charges. PEs are solvated in a solution of explicit water and 0.2 M NaCl salt. PAA and PMAA monomers both contain carboxylate group (COO^-) whose total charge is -0.9e (please note that 1.0e represents the charge of a proton). This stems from the fact that each O atom of the COO^- group has a charge of -0.8e and the C atom of the COO^- group

has a charge of $0.7e$. On the other hand, the total charge of the SO_3^- group (of the PSS molecule) is -0.56e. This stems from the fact that each O atom of the SO_3^- group has a charge of -0.68e, while the S atom of the SO_3^- group has a charge of $1.48e$. The effect of this disparity in the overall charge of each functional group (or the overall charge density) between the PAA (or PMAA) and the PSS brushes in the electric-field-response of these brushes will be probed here.

We study the responses of the PAA (and PMAA) and PSS brushes to an external axial (in x direction) electric field $\boldsymbol{E}$ (of strength 0.1 V/nm and 1 V/nm) [see Fig. 2.1(a)]. An electric field of strength E induces a force of q_iE on the atom i having a charge of q_i.

Depending on the type of the PE, the electric field changes the configuration of the PE in two separate ways. In the presence of the electric field, the reduction in average *end-to-end brush height* [defined in Fig. 2.1(a)] is similar for both the types of PE. Despite that, the corresponding variation of the *end-to-end distance* [defined in Fig. 2.1(a)] is significantly different between the cases of the two PEs [Fig. 2.1(b)]. For PAA, for example, the electric field reduces both the end-to-end height and end-to-end distance [Fig. 2.1(b)]. On the contrary, for the PSS brush, there is little change in the end-to-end distance with the electric field (in fact, the end-to-end distance even increases a little for the highest electric field) [Fig. 2.1(b)]. The above findings point to an end-to-end height reduction *via* the bending-driven and tilting-driven mechanisms for the PAA and the PSS brushes, respectively. Fig. 2.1(c) providing the average brush profiles along the direction of the electric field hints at these observations, namely the shrinking (or bending) of the PAA brush and the tilting (in a direction opposite to the direction of the applied electric field) of the PSS brush.

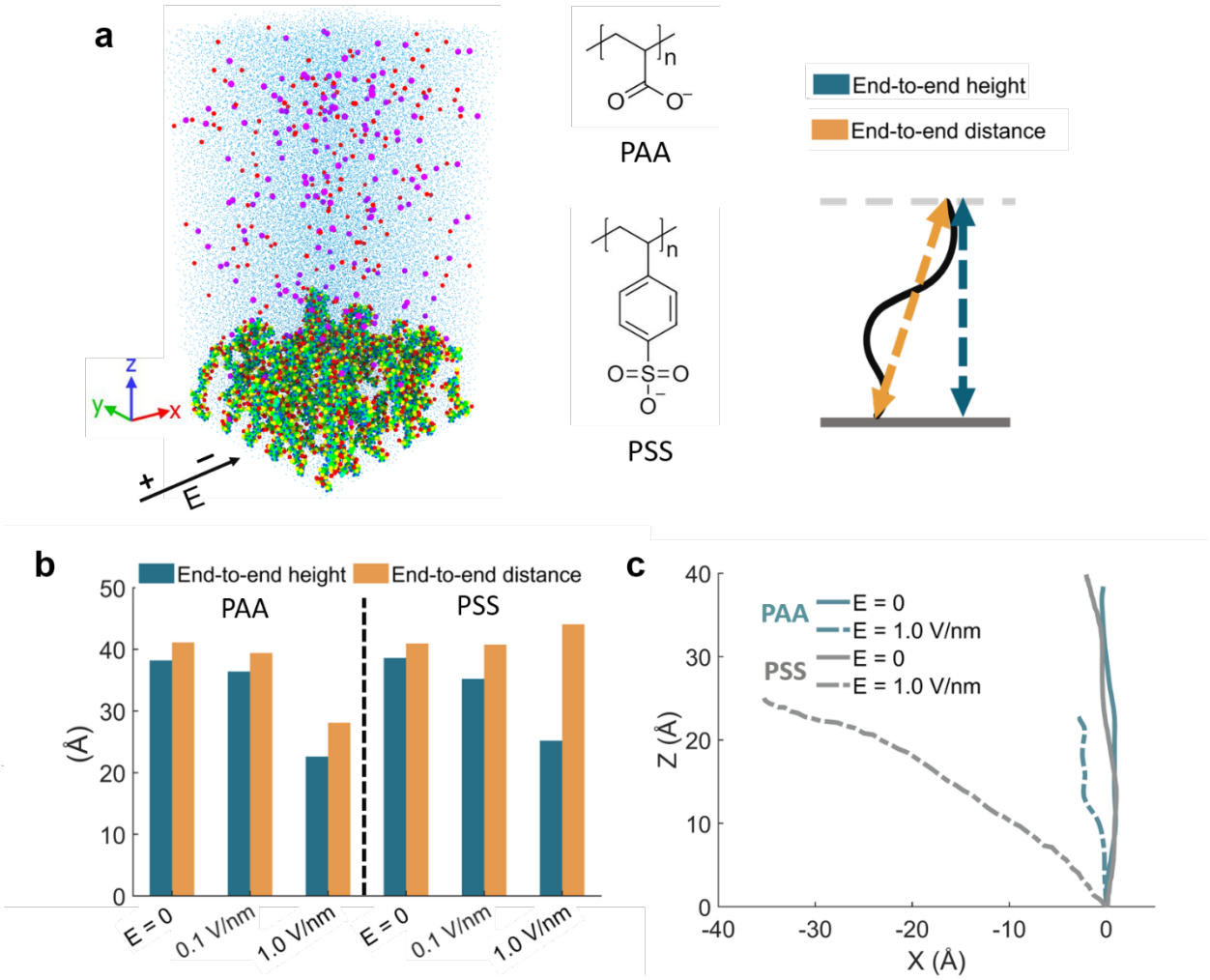

Figure 2.1: (a) (left) Simulation system with grafted PE (PAA) brush, counterions, co-ions, and water molecules for elucidating the effect of an axially employed electric field on the PE molecule. Green, yellow, and blue circles represent the carbon, oxygen, and hydrogen of the PE. Red and purple circles indicate Na^+ and Cl^- ions. Teal dots indicate water. (a) (center) Chemical structures of the studied PEs (PAA and PSS). (a) (right) Considering the black line as a representative PE chain, we define the end-to-end height and the end-to-end distance. (b) Equilibrium (*i.e.*, in the absence of an applied electric field) and steady-state (*i.e.*, in the presence of the applied electric field of different strengths) end-to-end brush heights and end-to-end distances for PAA and PSS. (c) Equilibrium (*i.e.*, in the absence of an applied electric field) and steady-state (*i.e.*, in the presence of an applied electric field of strength 1 V/nm) profile for the PAA and PSS brushes.

In Fig. 2.2, we probe the response of the PAA brushes to the axial electric field. First, in Fig. 2.2(a), we show how a positive counterion surrounds a negatively charged carboxylate monomer (of the PAA polymer) in absence and in presence of the electric field. We assign a (0,0,0) position to every $O_{Carboxylate}$ atom (charged oxygen atom) of the PAA, identify the solvation shell of this $O_{Carboxylate}$ atom, and quantify the locations of the counterions within this solvation shell (please see method section (figure 2.10) in for the corresponding $O_{Carboxylate}$-counterion radial distribution function). The ensemble averages of counterion locations for the cases of E=0 and E=1 V/nm are shown in Figs. 2.2(a-i, a-ii). Counterions are positively charged; therefore, an electric field along the positive x-direction enforces the positively-charged counterions to move in the positive direction (*i.e.*, to the right of the $O_{Carboxylate}$ atom) causing a larger concentration of counterions for $x > 0$ [Fig. 2.2(a-ii)]. Fig. 2.2(a-iii) confirms this observation by depicting a higher value of counterion distribution at a distance of 2 Å away from an $O_{Carboxylate}$ in the positive *x*-direction in presence of the applied electric field. The space integral of this counterion distribution is equal to the average number of counterions in the first solvation shell of an $O_{Carboxylate}$; in other words, if we denote the counterion distribution [as shown in figure 2.2(a-iii)] as *Y* and the average number of counterion in the first solvation shell of an $O_{Carboxylate}$ as *N*, we can write $\int_{-r}^{r} Y dr = N$ (where *r* represents the solvation shell size of the $O_{Carboxylate}$ atom).

We next divide the monomers of the PAA PE brush into two categories: monomers on the left and monomers on the right of the PE backbone (with respect to the grafting position). Figure 2.2(a) confirms that in the presence of the applied electric field, the counterions prefer to localize on the right side of the monomers giving rise to a directional nature to the monomer-counterion (or $O_{Carboxylate}$-counterion) complex. However, for those monomers that are themselves on the left side of the PE backbone, this directional migratory tendency of the complex is impeded due to the

steric hindrance imparted by the presence of the PE backbone and the repulsion (to the counterions) exerted by $C_{Carboxylate}$ (partially positively charged) atoms of the PE backbone [Fig. 2.2(c-i)]. As a consequence, there is an almost uniform counterion distribution around an $O_{Carboxylate}$ (of the monomer) that is on the left side of the PE backbone [see Figs. 2.2(b-i, b-ii)]. This same directional migratory nature of the $O_{Carboxylate}$-counterion complex implies that for the monomers that themselves are on the right side of the PE backbone, the counterion will move to the right of the monomers, *i.e.*, away from the PE backbone (as they are subjected to no retarding effect from the PE backbone). Consequently, there is an asymmetrically larger counterion distribution on the right side of the $O_{Carboxylate}$ (or of the monomer) that themselves are on the right side of the PAA PE backbone [see Fig. 2.2(b-ii, b-iii)].

As the counterions on the right side of the PE backbone are not impeded in their responses to the applied axial electric field [Fig. 2.2(c-ii)], their numbers per monomer remain almost similar with and without the electric field [Fig. 2.2(c-iii, c-iv)]. However, the counterions on the left side of the PE backbone, being impeded by the PE backbone in their (migratory) responses to the axial electric field, are forced to leave the solvation shell of the PE monomer [Fig. 2.2(c-i)] ensuring that at such locations their numbers per monomer become much smaller than that with no electric field [Fig. 2.2(c-iii)]. It should be noted that the average number of Na^+ ions per $O_{Carboxylate}$ atom is 1.4-1.6 (for E=0): this stems from the different bridging behaviors (please figure 2.7 and associated discussion) resulting in a given Na^+ ion being present in the first solvation shell of more than one $O_{Carboxylate}$ atom.

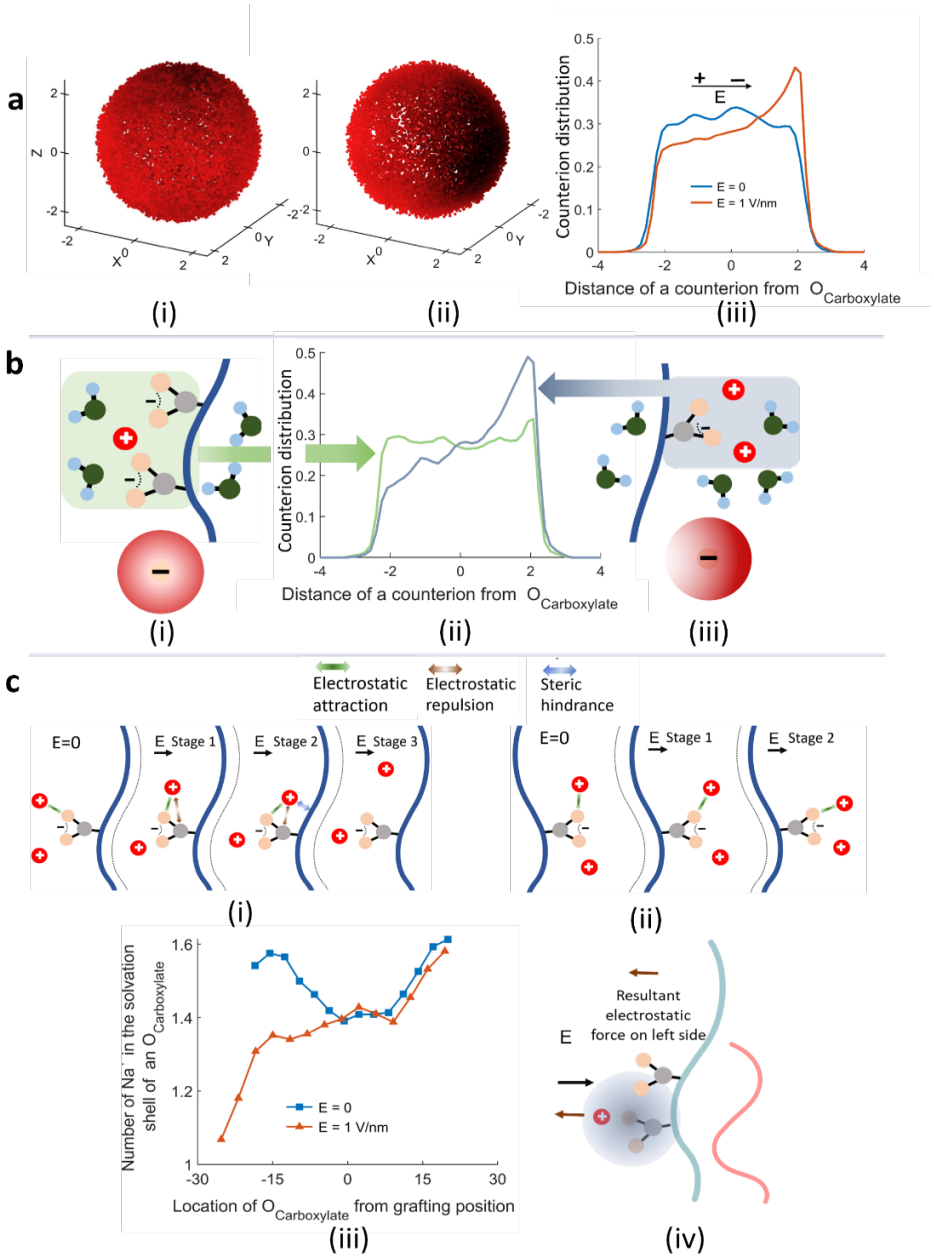

Figure 2.2: (a) Distribution of counterions around an $O_{Carboxylate}$ for the case of (i) E=0 and (ii) E=1 V/nm. Progression from lighter to darker red indicates an increase in the counterion distribution. (a-iii) Distribution profile of the counterion around an $O_{Carboxylate}$ along the electric field direction. (b-ii) Counterion distribution profile around $O_{Carboxylate}$ for two different regions under 1 V/nm electric field. (b-i) A schematic of the left side of the PE backbone (with respect to the grafting position) and a cartoon representation of the uniform counterion distribution around an $O_{Carboxylate}$. (b-iii) A schematic of the right side of the PE backbone and a cartoon representation of the non-uniform counterion distribution. (c-i) Schematic showing the expulsion of counterions from the left side of the PE chain under applied axial electric field. (c-ii) Schematic showing the manner in which the electric field can localize the counterions to the right side of the monomer without exclusion. (c-iii) Symmetric and asymmetric number of counterions per $O_{Carboxylate}$. (c-iv) Schematic showing the mechanism of the reduction of the brush height as a result of the bending. The distances appearing in all the figures have units of Å.

Since in the presence of an axial electric field there are lesser number of counterions on the left side of the PAA backbone, as compared to that on the right side of the PAA backbone, this particular section (on the left of the PAA backbone) behaves like a *locally electronegative segment*. As a consequence, this segment, in presence of the positive electric field, attempts to move in the negative x −direction, gets compressed (and hence undergoes bending and not tilting), and ultimately results in an overall brush height reduction [Fig. 2.2(c-iv)]. The brush profiles [see Fig. 2.1(c)] and the brush monomer probability distributions [see Fig. 2.5(a) and associated discussions] along electric field direction confirm these observations.

Things become significantly different when we change the polymer type from PAA to PSS. Counterion distribution around the $O_{Sulfonate}$ atom (charged oxygen atom) of the PSS brushes, very much like the counterion distribution around the $O_{Carboxylate}$ atom of the PAA, is directional [see Fig. 2.3(a-i, a-ii)]. Interestingly, however, the value of the counterion distribution around the $O_{Sulfonate}$ atom of the PSS is reduced to almost one third of the corresponding value of the counterion distribution around the $O_{Carboxylate}$ atom of the PAA [see Fig. 2.3(a-iii) and compare it with Fig. 2.2(a-iii)]. Given that the space integral of this counterion distribution around the $O_{Sulfonate}$ atom is equal to the average number of counterions in the first solvation shell of an $O_{Sulfonate}$ atom (see the discussions for Fig. 2.2), Fig. 2.3(a-iii) confirms a lesser average number of counterions in the first solvation shell of $O_{Sulfonate}$ than $O_{Carboxylate}$. This can be attributed to a weaker charge density of the PSS. A lesser number of counterions (0.4-0.5) per $O_{Sulfonate}$ is also visible from Fig. 2.3(b) [on the contrary, the average number of counterions per $O_{Carboxylate}$ was 1.4-1.6]. Also, in presence of the electric field, the number of counterions per $O_{Sulfonate}$ reduces uniformly (i.e., unlike the case of PAA, there is no left-right asymmetry in the counterion numbers per O, with respect to the polymer grafting position). As the number of Na^+ counterions is less (as well as nearly uniform)

in all portions of the PSS brush molecule irrespective of the position of a monomer from the grafting location, all the monomers act as *locally electronegative segments with nearly identical net negative (unbalanced) charge*. Accordingly, the application of the electric field tries to move all of these *locally electronegative* segments in a direction opposite to the direction of the electric field. This leads to the tilting of the PSS brush molecule in the direction opposite to the direction of the applied electric field [the mechanism is shown in Fig. 2.3(c) and is also confirmed by the PSS profile shown in Fig. 2.1(c)] eventually causing a decrease in the height of the PSS brush molecule.

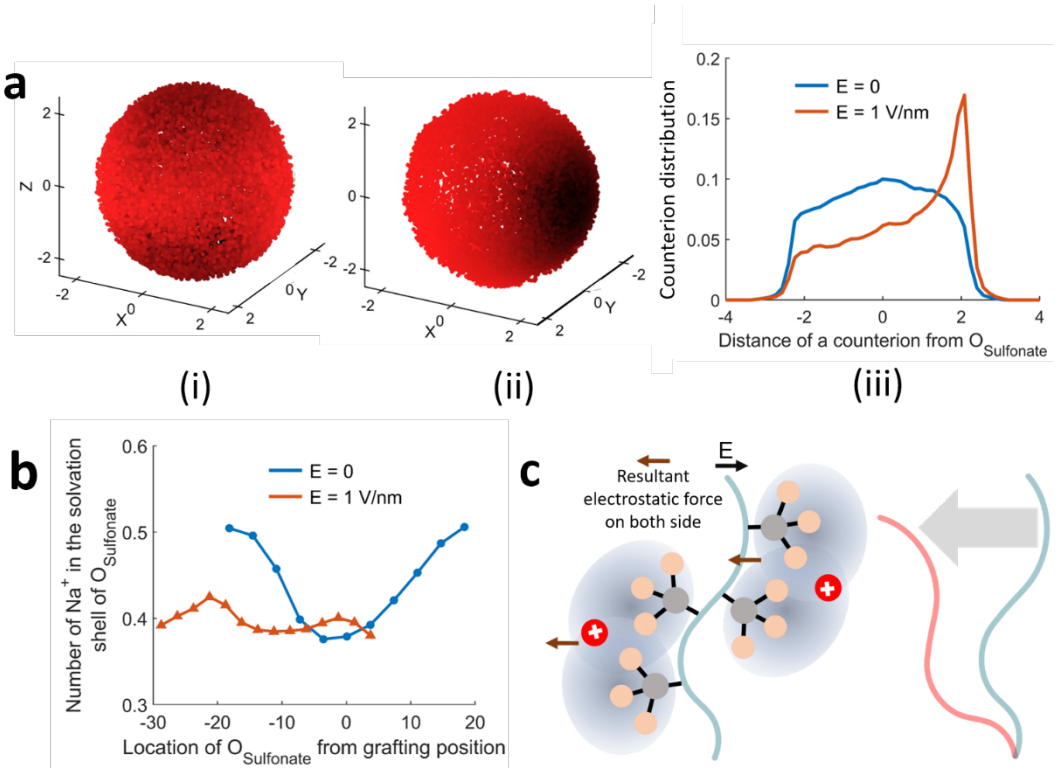

Figure 2.3: (a) Distribution of counterions around an $O_{Sulfonate}$ ($O_{Sulfonate}$ acts as the center of the sphere) for the case of (i) E=0 and (ii) E=1 V/nm. Progression from lighter to darker red indicates an increase in the counterion distribution. (a-iii) Distribution of the counterion around an $O_{Sulfonate}$ in absence and in presence (along the electric field direction) of the applied electric field. (b) Number of counterions per $O_{Sulfonate}$ as function of the distance of the $O_{Sulfonate}$ from grafting position in absence and in presence of the applied electric field. (c) Schematic representation of the mechanism of the tilting of the PSS brush (and the resulting reduction of the brush height) in the presence of the electric field. The distances appearing in all the figures have units of Å.

Fig. 2.4 shows the cumulative distribution function (CDF) of counterions around PAA and PSS monomers. CDF is calculated by considering all the counterions inside brush layer and finding the nearest O of a monomer from it. For the PAA brush molecule, all the counterions remain within the first solvation shell of $O_{Carboxylate}$ and accordingly, the application of the electric field does not significantly change the CDF. On the other hand, as $O_{Sulfonate}$ has a lesser charge density, not all the counterions are inside the first solvation shell; therefore, in presence of the electric field the counterions become even less condensed on the monomers thereby making the PE monomers *locally electronegative.* These results indicate the possibility of independent movement of monomers and Na^+ in PSS and lack of it in PAA grafted systems. Results for CDF also justifies the ion distribution in Fig. 2.3(b): in presence of the electric field, the ion distribution flattens (i.e., the peaks witnessed for E=0 are no longer present) and becomes uniform (without left-right asymmetry) across the PE backbone.

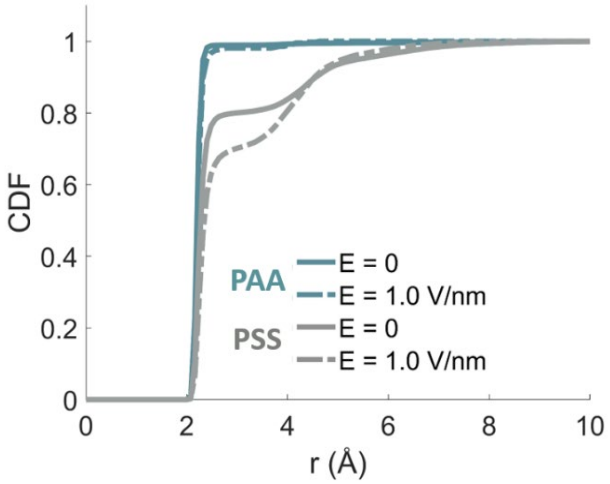

Figure 2.4: Cumulative distribution function (CDF) of counterions around the PE monomer for different PEs in absence and in presence of the applied electric field.

An understanding of the variation of the monomer distribution of the two different types of the PEs (PAA and PSS) in response to the applied electric field is important as that will help verify our explanations (see above) on the charge-density dependent changes in the configurations of the PEs in response to the applied electric field. Such variation in the monomer distribution is studied by quantifying the probability distributions of $O_{Carboxylate}$ (for the PAA brush molecule) and $O_{Sulfonate}$ (for the PSS brush molecule) around their respective grafting position (along the direction of the axial electric field) [see Figs. 2.5 (a-i, a-ii)]. For the PAA brush molecule, we find very little shift in the $O_{Carboxylate}$ probability distribution in presence of the electric field: this indicates that the PAA monomer does not prefer to align in any particular direction in presence of the applied electric field. On the other hand, there is a significant axial shift (towards negative *x* direction) in the $O_{Sulfonate}$ probability distribution for the PSS in presence of the applied electric field. Such electric-field-driven shift of the $O_{Sulfonate}$ probability distribution towards the negative *x* direction is commensurate with the electric-field-driven tilting of the PSS chains in the negative *x* direction.

In order to quantify the electric-field-induced changes in the intrinsic flexibility of the PAA and PSS chains (which might affect the brush conformational changes in presence of the applied electric field), we calculate the backbone angle-angle or orientational correlation as a function of the chemical distance (s) which is defined as:

$$\langle cos\theta(s)\rangle = \langle \vec{a}_i . \vec{a}_j \rangle / {l_b}^2, \quad (2.1)$$

where $s = |i - j|$, $\vec{a}_i = \vec{r}_i - \vec{r}_{i-1}$, $l_b = |\vec{a}_i|$, and $\vec{r}_i$ is the position of each backbone carbon [56]. For more flexible chains, this orientational correlation shows a larger decay (from 2.1) with *s*. Fig. 2.5(b) shows that with no electric field, both types of PEs have similar flexibility. However, in presence of the electric field, there is a quick loss of orientational correlation for the PAA chains,

confirming increased flexibility: this is commensurate with the electric-field-driven bending (and the resulting height reduction) of the PAA brushes. For the PSS chains, on the other hand, the orientational correlation increases with the electric field. Therefore, the presence of the electric field makes the PSS chains stiffer, justifying its behavior as a tilted (and not bent) system (and tilting-driven height reduction).

To check for the similarity among the chains, we have next calculated the dissimilarity matrix based on the cosine criteria [57] [see Fig. 2.5(c)]. For the calculation of the cosine

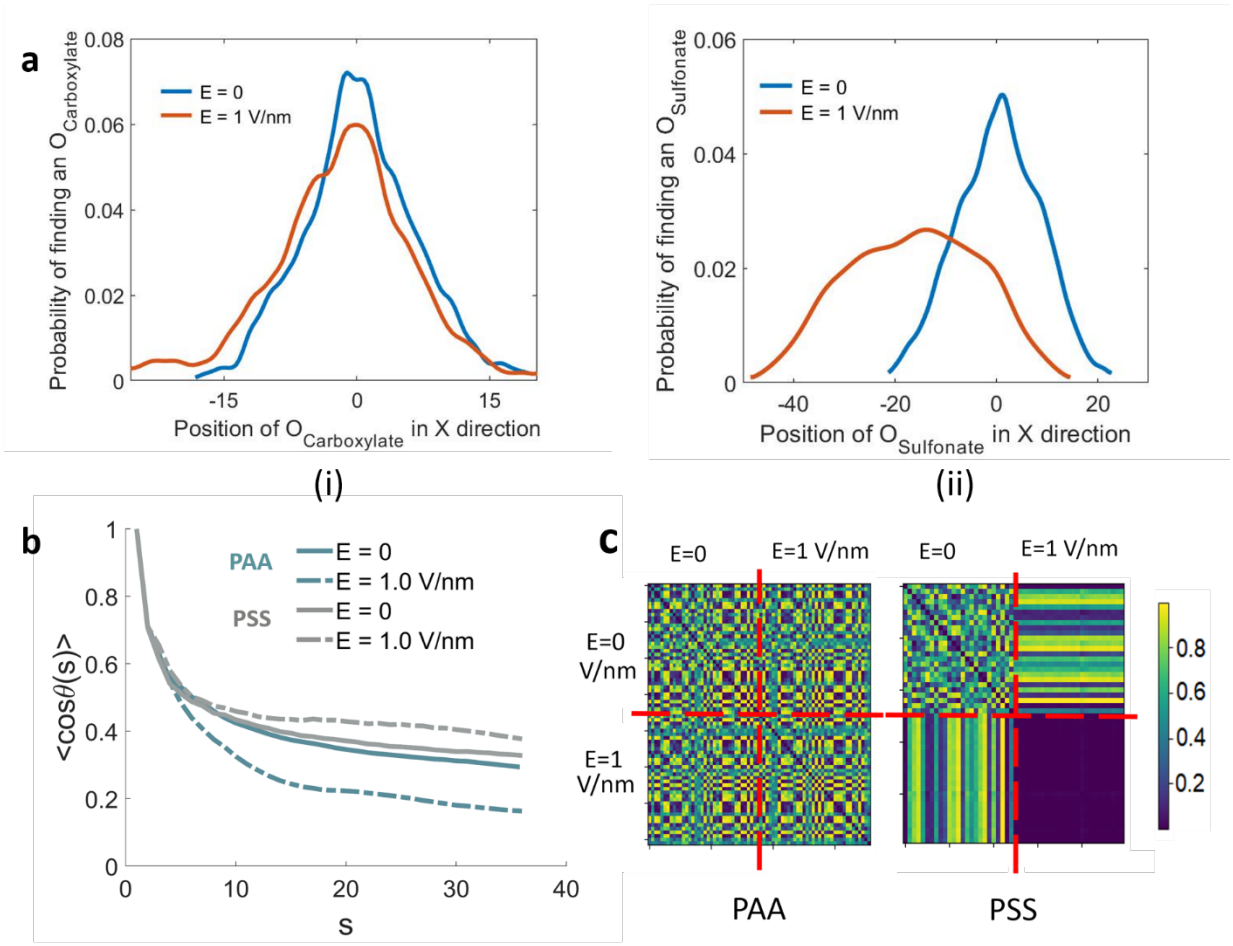

Figure 2.5: (a) Monomer probability distribution for (i) PAA and (ii) PSS in the presence and in the absence of the axial electric field. (b) Orientational correlation function of chemical distance ***s*** for different PEs in the absence and in the presence of the applied electric field. (c) Dissimilarity matrix for the PAA and PSS brush molecules in the absence and in the presence of the applied axial electric field. Blue to yellow in the colorbar indicates the occurrence from similar chains to dissimilar chains.

dissimilarity, we have used the distance of each backbone carbon from their grafting position in the x direction. From Fig. 2.5(c), we can see that the PAA chains are very much dissimilar from each other. The application of the electric field does not introduce any similarity in the PAA PE chains. The chains are also dissimilar for the PSS in equilibrium (i.e., in absence of the applied electric field). However, in the presence of the applied axial electric field, the PSS PE chains tilt in the negative *x* direction and their dissimilarity reduces drastically. This drastic reduction in the dissimilarity for the PSS PE chains confirms that all the PSS chains responds to the electric field similarly and their final configurations are similar to one another.

Main results for the PMAA PE Brushes

To be more confident in our simulations and inferences, we simulated a fully ionized poly (methacrylic acid) (PMAA) brush. PMAA has the same charged functional group (COO^-) as the PAA with an additional methyl group [See Fig. 2.6(a)]. The parameters for the PMAA are similar to that of the PAA. The grafting density for the PMAA brush is similar to that of the PSS brushes. To compare the findings associated with the PMAA brush with those reported in Fig. 2.1, we have analyzed the end-to-end brush height and the distance for the PMAA brush molecule in presence and in absence of the applied axial electric field. It is evident that, with the application of the electric field, both the end-to-end height and the end-to-end distance of the PMAA brush molecule reduces in a manner that is very much similar to that of the PAA brushes [see Fig. 2.6 (b,c)]. Furthermore, no significant tilt is observed in the average PMAA brush profile under the electric field [see Fig. 2.6 (b,c)]. These results again reinforce our inference that the charge density of the pendant group is the main factor contributing to the eventual response of the PE brushes to the electric field. Since, PMAA systems has the same grafting density as PSS, it also signifies that

grafting density does not affect our main interpretations significantly.

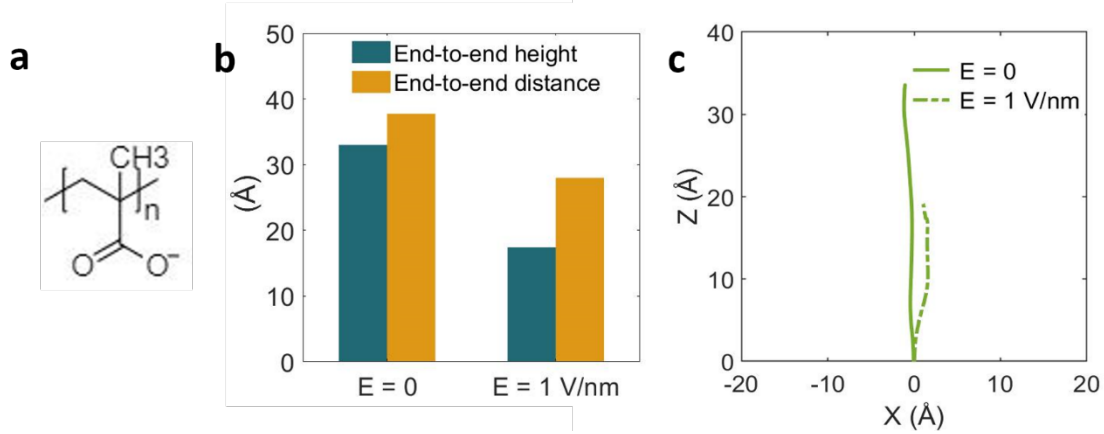

Figure 2.6: (a) Chemical structures of the studied PMAA. (b) Equilibrium (*i.e.*, in the absence of an applied electric field) and steady-state (*i.e.*, in the presence of the applied electric field of different strengths) end-to-end heights and end-to end distances for PMAA brushes. (c) Equilibrium (*i.e.*, in the absence of an applied electric field) and steady-state (*i.e.*, in the presence of an applied electric field of strength 1 V/nm) profile for the PMAA brush molecule.

Relevance of the present study

This study demonstrates that a variation in the charge density of the grafted PE brushes and the resulting response of the counterions (to an external axial electric field) ensures a brush height reduction by virtue of either bending (for cases of PEs with higher charge densities, e.g., PAA and the PMAA) or tilting (for the PE with lesser charge density, i.e., PSS). Such specific PE responses to the electric field have the potential to be employed in a myriad of applications. In the following sections, we will try to briefly summarize a few of the possible impacts of our findings.

Counterion mediated bridging interactions is an important concept that dictates the conformation of PE brushes and regulates the use of the PE brushes in several applications. Bridging interactions occur when a counterion accommodates (in its solvation shell) two or more

monomers from non-neighboring monomers. These non-neighboring monomers can be from the same or different chains; in case they are from the same chain the interactions are denoted as *intrachain bridging*, while the interactions are denoted as *interchain bridging* if the non-neighboring monomers are from different chains. Higher interchain bridging is attributed to higher frictions which hinder the applicability of the PE brushes in lubricity applications [47]. Bridging can also dictate the ion distribution inside the PE brush layer and the surrounding solution, which can be important in ion sensing, flow inside nanochannel, etc. Here we have checked the variation of interchain bridging for all the cases and the results are provided in Fig. 2.7. For this calculation, we considered all the counterions that are present inside the brush layer and checked their first solvation shell for the O from different monomers (see Chapter 3 for the calculation details). With the application of the electric fields, interchain bridging increases for the PAA and PMAA brushes. On the other hand, no such augmentation of interchain bridging is observed for the PSS brushes.

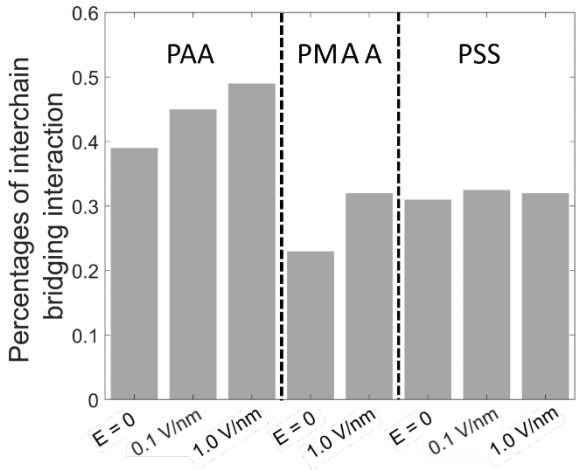

Figure 2.7: Counterion mediated interchain bridging interactions for the PAA, PMAA, and PSS brushes in the absence and in the presence of the applied axial electric fields.

Drummond [20] had shown that the application of the electric field can enhance the lubrication properties of the PE layers; for example, the friction coefficient can sometimes become almost undetectable in the presence of an external electric field. This is because of the electric-field-mediated reduction of the PE brush height which creates a salt-water layer in between two originally interpenetrating PE layers. In our study, too the brush height reduces for all cases; such brush height reduction, following the principle proposed by Ref. 20, can be harnessed for better lubrications in a nanochannel (despite the fact that our study considers the presence of an axial applied electric field, while Ref. 20 considers a transverse electric field). Lubrication properties might also depend on the alignment of the friction-inducing particles with respect to the applied electric field. If a PE chain or other type of connected beads are perpendicular to the electric field, larger friction will be induced [19, 58] as compared to the case when these connected beads are aligned parallelly to the applied electric field. Our study shows that depending on the charge density of the PE brushes, there can be significant differences (with respect to the direction of the applied electric field) in the overall alignment of the PE chains: this, therefore, can significantly alter the lubrication properties as a function of the nature of the PE brushes. PE chain stiffness can also be important when designing a system for a lower friction coefficient. A recent study has shown that [59] stiffer chain can be linked to lower friction. In our calculations [see Fig. 2.5(b)], we showed that the application of the axial electric field will decrease the stiffness of the PSS chains and increase the stiffness of PAA chains. Therefore, our findings also indicate the possibilities of regulating friction in PE grafted systems by leveraging the electric-field-mediated alteration of the stiffnesses of the PE chains.

Researchers [21-23] have proposed an electric field enabled method for fabricating drug and gene carrying multilayered PE complex films (the electric field maintains a particular

configuration of the PEs and speeds up the process). Our simulations establish that depending upon the charge density of the PE, the electric field can enforce a particular configuration (a compressed state or a tilted state) to the PE: this knowledge has the potential to guide researchers to design a more efficient method of electric field enabled PE complex film fabrication.

In a soft device, a soft structure should respond to a given signal by changing its shape to perform a specified task. Study shows that ensuring electric field actuated controlled and specified tilting of PE molecules (constituting a PE gel) is essential in developing soft devices based on such PE gels [24,25,55]. On the other hand, electric field driven periodic bending and shrinking is observed in a PE gel made of PAA and Na^+ counterions [26]. Given that depending on the PE charge density, we observe both of such behaviors (tilting or shrinking) in the system we study (in fact, our results on the shrinking and bending of the grafted PAA brushes screened with Na^+ counterions provide the first possible atomistically-resolved explanation of the response of the PAA to an applied electric field), our findings will be significant for better understanding a myriad of different soft device applications.

Justifications of using different simulation parameters

In our study, we have performed equilibrium and non-equilibrium MD simulations of systems grafted with PE chains. It is important to discuss our computational study in the light of the experiments and the feasibility of the parameters considered in our systems. In this section, we will discuss a few of these important parameters and considerations.

Grafting density:

PAA chains are grafted with a grafting density of $0.05/\sigma^2$ (σ=3.5 Å, is the LJ distance parameter of backbone carbon atoms) whereas PSS chains are grafted with a grafting density of

$0.03/\sigma^2$. As the pendant group of the PAA and the PS chains are of different sizes (large benzene group in the PSS), the same grafting density for the PAA and the PSS brushes would imply a different degree of confinement for the two cases. To nullify any effect of the grafting density, we have modeled the PMAA with a grafting density of $0.03/\sigma^2$. The results for the PMAA (with same grafting density as PSS) are similar to that of PAA: this indicates that the results are mostly grafting density independent. We have also checked the density of water inside the PE to quantify the degree of confinement (see Fig. 2.8). If we have used the same PE chains, a lower grafting density and a consequent lesser degree of confinement would result in a higher density of water inside the brush layer. Here, although we have used a significantly smaller grafting density for the PSS brushes as compared to the PAA brushes, the water density is actually higher inside the PAA brush layer (see Fig. 2.8). Such a finding implies that the strategy of considering different grafting densities for the PAA and the PSS is reasonable and it ensures that the degree of confinement (for the two cases) becomes comparable. Also, these grafting density values used for the PAA and PSS chains are within the range of experimentally reported grafting densities [60,61].

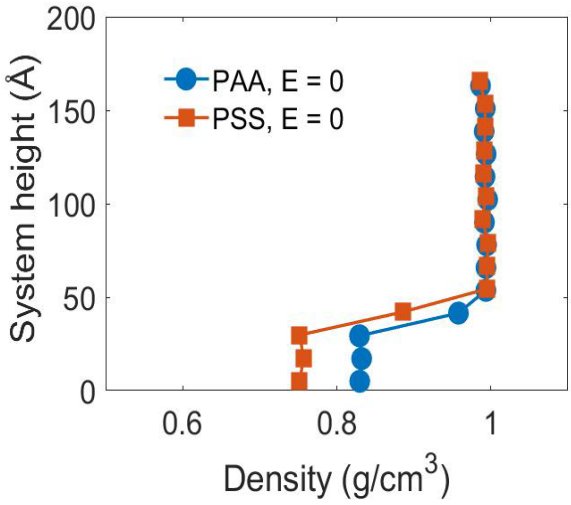

Figure 2.8: Density of water inside the PAA and PSS brush layers and in the solvent in absence of the applied electric field.

Electric field strength:

In our simulations, we have used electric fields in the range of 0.1 V/nm to 1 V/nm. These electric fields are higher than that usually employed in the experiments. A few considerations will be discussed justifying the application of such high electric fields. As we have performed all-atom MD simulations, a high electric field is needed to observe the different results associated with the electric field. As the trends remain the same for 0.1 V/nm and 1 V/nm, we can say that our observed results will remain qualitatively similar even for smaller electric field strengths.

An important concern associated with the employment of large electric field strengths is that for very large electric fields water might dissociate. The reported electric field strength value corresponding to the initiation of water dissociation is around 2.5 V/nm and for frequent dissociation, one needs an applied electric field of 3.5 V/nm [62,63]: these numbers are several times higher than the highest electric field (1 V/nm) used in our simulation.

We also want to discuss the practical applicability of the high external electric field strengths employed in our simulations. Experimental systems involving water have employed electric fields as high as 1-5 V/nm [64]. In fact, electric fields on the order of 0.1−1 V/nm are used in several experimental studies related to bio-polymers. For example, electric fields were calculated to be in the range of 1−2.5 V/nm in a study where protein cytochrome c was immobilized on silver electrodes in the presence of electric fields [65]. Similarly, an electric field of 0.31 V/nm was used for probing the electromechanics of a DNA molecule in a synthetic nanopore [66].

Fully-ionized PAA:

In our study, we tried to quantify the effect of the PE charge density on the on the electric-field response of the PAA and PSS brushes . For this, we tried to have a similar degree of ionization for

both the PAA and PSS molecules. PAA is a weakly dissociating polymer, and its degree of ionization depends on the local pH, salt concentration, etc. For a pH value above its pKa (~5), PAA is likely to be highly ionized [60], which justifies our consideration of fully ionized PAA.

2.3 Methods

Our main simulation contains, fully ionized poly (acrylic acid) (PAA), poly (methacrylic acid) (PMAA), and poly (styrene sulfonate) (PSS) as the polyelectrolytes and SPC/E water [67] molecules. Sodium (Na^+) counterions screen the PE brush charges. In addition, we add 0.2 M NaCl salt. PAA chains are grafted with a grafting density of $0.05/\sigma^2$ (σ=3.5 Å, is the LJ distance parameter of backbone carbon atoms) whereas PSS and PMAA chains are grafted with a grafting density of $0.03/\sigma^2$. Each chain has 49 backbone carbon atoms. Purely repulsive walls are placed at the top and the bottom of the system to prevent the mobile ions and water molecules from escaping the system. 36 (25) PAA (PSS, PMAA) PE chains are grafted on the bottom wall in a 6*6 (5*5) array. The particle trajectories are calculated using the Velocity-Verlet algorithm, with a time step of 2 fs. Non-bonded interactions are modeled via a shifted-truncated 12-6 Lennard Jones potential (U_{LJ}) with a cut-off of 13Å. Long range Columbic interaction is calculated using a PPPM (particle-particle particle-mesh) algorithm [68]. The bonds and angles of water molecules are conserved by using the SHAKE algorithm [69]. Simulations are performed in LAMMPS [70] and OVITO [71] is used to visualize the simulation system.

We use the OPLS-AA [72] force field to model the brush molecules and employ the study by Joung *et al* [73]. for calculating the potentials for the mobile ions. These vastly used parameters for monovalent ions [73] were adjusted to the solvation free energy of ions in water and the lattice energy of ionic crystals. OPLS force field, which is used to model the PE brush molecule, has been

used for modeling a variety of polymer systems [74-76] and is considered as one of the most accurate force field parameters. Geometric mixing rules are used for the LJ interactions between dissimilar atoms, except for the ion-ion and ion -water interactions. For these ion-ion and ion-water, we have used Lorentz-Berthelot mixing rules to remain consistent with the approach of Joung et al. [73].

OPLS-AA force field, when coupled with SPC/E water, shows a very good accuracy for capturing different facets of polymeric systems. For example, Hu et al [77] examined the different force field parameters used for the aqueous polymeric systems and found that combination of OPLS-AA parameters and SPC/E water model gives very good results. With regards to dynamic properties, their calculations showed that the combination of the SPC/E model and the OPLS force field is best in predicting water diffusivity not only in the bulk phase but also within protein crystal [77]. Results also suggest that when coupled with the SPC/E model, ion parameters used in our simulation fairly accurately model the dynamic behavior of the monovalent ions in aqueous solution for a wide range of concentrations [78].

The system is first run in the NP_zT ensemble (the subscript z signifies that only the system height is allowed to change) to obtain the correct simulation box height at 300 K and 1 atm, by applying the Nosé-Hoover thermostat and barostat [79,80]. Then, the system is equilibrated in the NVT ensemble to obtain the correct equilibrium configuration of the system by applying the Langevin thermostat [81]. We performed each simulation until the brush height starts fluctuating around a constant value. Then the production period is performed for 15 ns for all the cases of the simulations. After initial equilibration, we apply the axial electric fields under the NVT ensemble. Again, we performed each simulation until the end-to-end height and distance starts fluctuating around a constant value. Then the final production period is considered to be 15 ns.

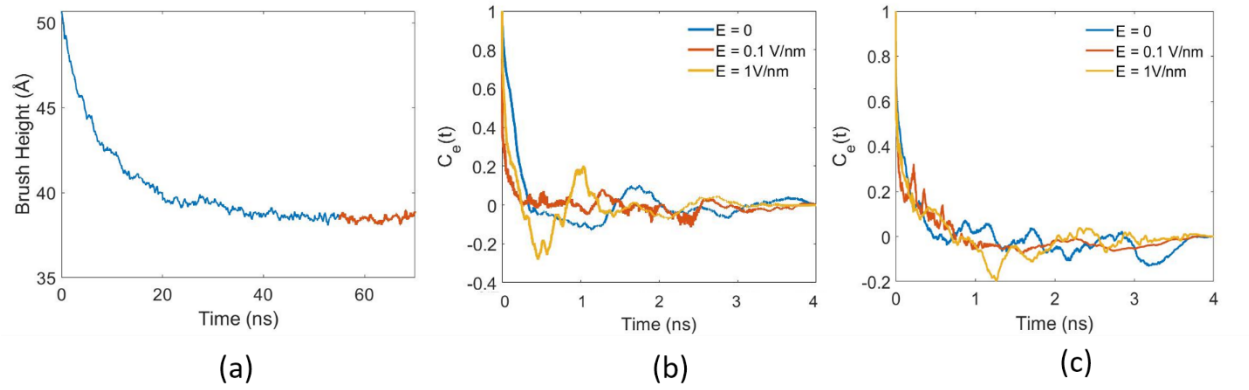

Figure 2.9: (a) Average end-to-end brush height for PAA, E=0. Autocorrelation fucntion of the end point of PE chains for different simulations, (b) PAA and (c) PSS.

We perform each simulation until the brush height starts fluctuating around a constant value. In this production period, the brush height fluctuates around a constant value, confirming the attainment of the equilibrium. In figure 2.9 (a), the average end-to-end brush height for PAA without applied electric field over the total simulation duration is shown. The red line indicates the variation of the end-to-end brush height during the production period. This production period is considered to be 15 ns for all the different simulations. We checked the autocorrelation function of the end-to-end brush height of the PE chains in this production run. The autocorrelation function for a variable Y is given by $C_Y(t) = \frac{(<Y(t)-\langle Y\rangle)(Y(0)-\langle Y\rangle>)}{<Y^2>-<Y>^2}$, where ⟨Y⟩ denotes the mean value of Y. We plot the autocorrelation function $[C_e(t)]$ for average end-to-end brush height corresponding to the cases of different simulations [Fig. 2.9 (b) for PAA and Fig. 2.9 (c) for PSS]. It can be observed that the autocorrelation functions for all the cases start fluctuating around zero very quickly, which indicates proper statistical sampling in total 15ns production run. Also, we shall like to point out here that we have averaged our result for the entire production period (i.e., 15 ns).

In table 2.1 have provided the breakdown of the total simulation for all simulations:

Simulation type	Equilibration time	Production time	Total simulation time
PAA, E = 0	55 ns	15 ns	70 ns

PAA, E = 0.1 V/nm	59 ns	15 ns	74 ns
PAA, E = 1 V/nm	52 ns	15 ns	67 ns
PSS, E = 0	51 ns	15 ns	66 ns
PSS, E = 0.1 V/nm	56 ns	15 ns	71 ns
PSS, E = 1 V/nm	48 ns	15 ns	63 ns
PMAA, E = 0	49 ns	15 ns	64 ns
PMAA, E = 1 V/nm	55 ns	15 ns	70 ns

Table 2.1: Variation of the simulation time for all simulations.

In Fig 2.10 we provide the $O_{Carboxylate}$-counterion radial distribution function (RDF) for the PAA and the PMAA, and the $O_{Sulfonate}$-counterion RDF for the PSS. The first valley of these RDFs is used as a cutoff to calculate the counterion distribution around the negatively charged O atom. These cutoffs are also used to calculate the counterion mediated bridging interactions. In presence of the electric field, there is a slight reduction in the value of the first peak for the RDFs for all the three cases.; other values are negligibly affected by the application of the electric field.

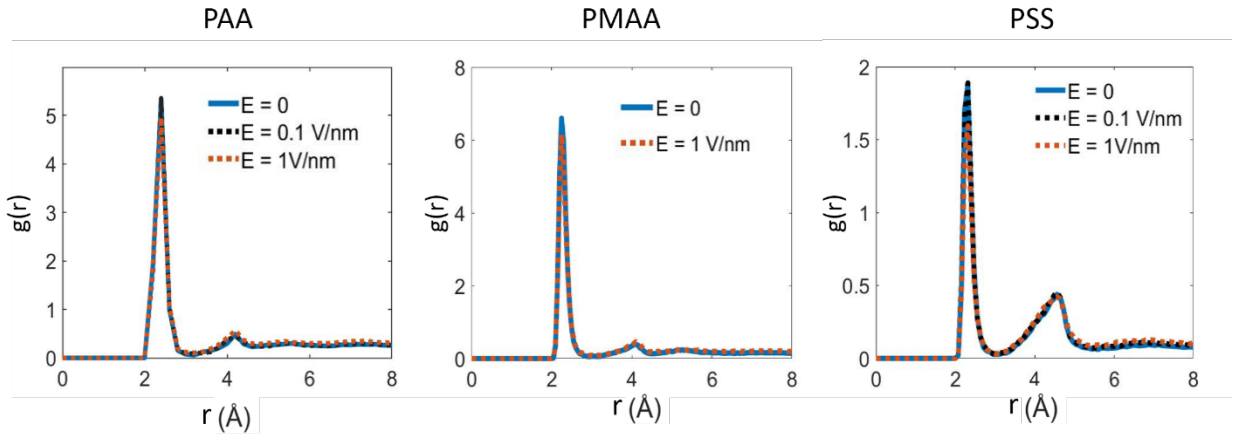

Figure 2.10: $O_{Carboxylate}$-counterion radial distribution function (RDF) for the PAA and PMAA and $O_{Sulfonate}$-counterion RDF for the PSS.

Force field parameter

In Fig. 2.11, we have provided partial schematic representations of the fully ionized poly (acrylic acid) (PAA) and (poly) styrene sulfonate (PSS) molecules. Definition of these atoms and their nonbonded parameters are given in table 2.2 (for PAA) and table 2.7 (for PSS). Bonded parameters (bond, angle, proper and improper dihedral) are discussed in subsequent tables. Please note that same parameters are used for PAA and PMAA.

The Lennard-Jones (LJ) potential (U_{LJ}) used in the simulations can be expressed as:

$$U_{LJ} = 4\epsilon_{ij}\left[\left(\frac{\sigma_{ij}}{r_{ij}}\right)^{12} - \left(\frac{\sigma_{ij}}{r_{ij}}\right)^{6}\right], \qquad (2.2)$$

while the Coulombic pairwise interaction (U_{Coul}) used in the simulation can be expressed as:

$$U_{Coul} = \frac{q_i q_j}{4\pi\epsilon_0\epsilon_1 r_{ij}}. \quad (2.3)$$

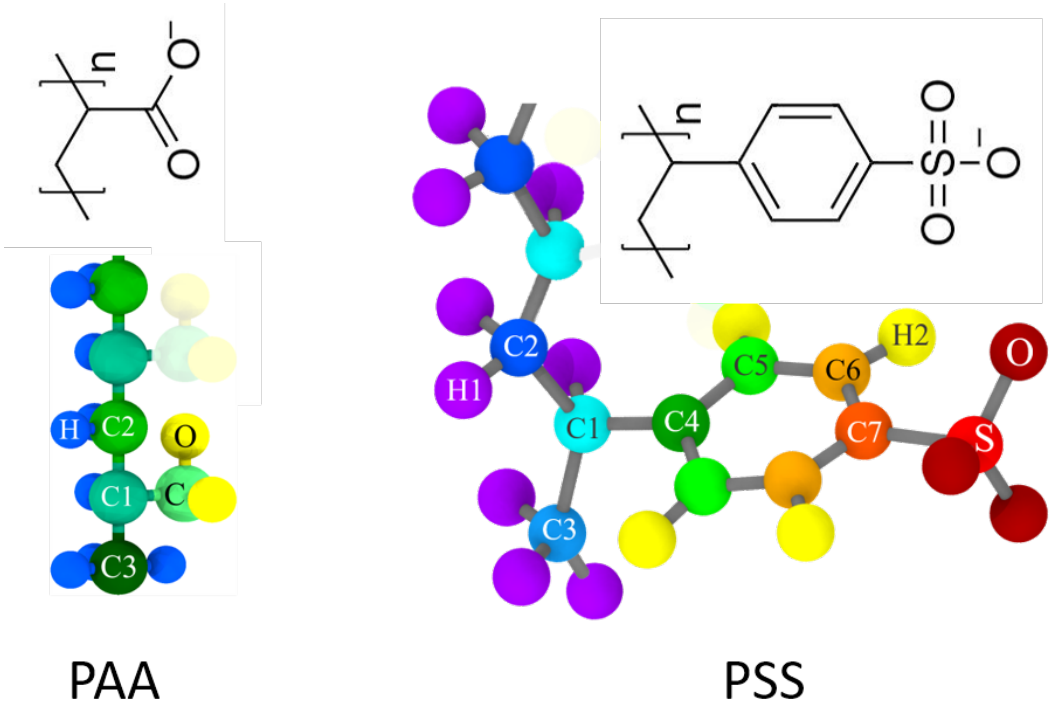

Figure 2.11: A partial schematic representation of the fully ionized PAA and PSS molecule. Different types of atoms are indicated with different colors.

In these equations, ϵ_{ij} is the depth of the LJ potential well between atoms i and j, σ_{ij} is the distance between atoms i and j when the potential energy is zero, q_i and q_j are charges of the i^{th} and j^{th} atoms respectively, r_{ij} is the distance between atoms i and j, $\in_0$ is the permittivity of a vacuum and $\in_1$ the relative permittivity of the background (used as 1).

Atom Type	**Charge (e)**	**Mass (amu)**	**ϵ (Kcal/mole)**	**σ (Å)**
C3 (CH_3)	-0.18	12.011	0.066	3.50
C2 (CH_2)	-0.12	12.011	0.066	3.50
C1 (CH, Attached to COO-)	-0.16	12.011	0.066	3.50
C (COO-)	0.70	12.011	0.105	3.75
H	0.06	1.008	0.03	2.50
O (COO-)	-0.80	15.999	0.210	2.96
O_w (H_2O)	-0.8476	15.999	0.155354	3.166
H_w (H_2O)	0.4238	1.008	0	0
Na	1.00	22.99	0.3526418	2.1595
Cl	-1.00	35.453	0.012785	4.83
Continuous LJ Wall (Parameters remain unchanged for interaction with all atom types)	0.00	15.00794	0.1947	3.00 (LJ cut off length is 3.36 Å)

Table 2.2: Charge, mass and LJ parameters for all the different atom types of PSS

Harmonic bond style is used to calculate the potential energy for the bond which is expressed as:

$$U_{bond} = K_b(r - r_0)^2. \qquad (2.4)$$

Here, r_0 is the equilibrium bond length and K_b is the bond stiffness. The values for r_0 and K_b for all bond types (present in the PAA molecules) are provided in Table 2.3. Please see table 2.8 for all the parameters governing the bonded potentials for the PSS molecule.

Bond Type	$\boldsymbol{K_b}$, $(\frac{\boldsymbol{Kcal}}{\boldsymbol{mol}.\text{Å}^2})$	$\boldsymbol{r_0}$, (Å)
C2-H	340.0	1.09
C2-C1	268.0	1.529
C1-H	340.0	1.09
C3-H	340.0	1.09
C-C1	317.0	1.522
C1-C3	268.0	1.529
C-O	656.0	1.25
O_w-H_w	-	1.00

Table 2.3: PAA bond parameters used in the simulations

The potential energy for the angle between different bonds is calculated using the following harmonic equation:

$$U_{angle} = K_a(\theta - \theta_0)^2. \qquad (2.5)$$

Here, θ_0 is the equilibrium value of the angle and K_a is the angle stiffness. The values for θ_0 and K_a for different angles associated with the PAA and the PSS molecules are provided in Table 2.4 and Table 2.9.

Angle Type	$\boldsymbol{K_a}$, $(\frac{\boldsymbol{Kcal}}{\boldsymbol{mol}.\boldsymbol{rad}^2})$	$\boldsymbol{\theta_0(deg)}$
H-C2-H	33.00	107.8
H-C2-C1	37.5	110.7
C2-C1-H	37.5	110.7
C1-C3-H	37.5	110.7
H-C3-H	33.00	107.8

H-C1-C	35.0	109.5
O-C-O	80.0	126.00
C2-C1-C	63.0	111.1
C3-C1-C	63.0	111.1
H_w-O_w-H_w	-	109.47
C2-C1-C2	58.35	112.7
C2-C1-C3	58.35	112.7
C1-C-O	70.0	117.0
C3-C1-H	37.5	110.7
C1-C2-C1	58.35	112.7

Table 2.4: Angle parameters for PAA used in the simulations

The potential energy for the 4-atom dihedral torsion interactions is given by

$$U_{dihedral} = \frac{1}{2}K_1[1 + \cos(\emptyset)] + \frac{1}{2}K_2[1 - \cos(2\emptyset)] + \frac{1}{2}K_3[1 + \cos(3\emptyset)] + \frac{1}{2}K_4[1 - \cos(4\emptyset)]. \quad (2.6)$$

Here, K_1, K_2, K_3 and K_4 are the four Fourier coefficients for torsional interactions, and $\emptyset$ is the torsional angle. Values of K_1, K_2, K_3 and K_4 associated with the PAA and the PSS molecules are provided in Tables 2.5 and 2.10, respectively.

Dihedral type	$\boldsymbol{K_1}$, $(\boldsymbol{Kcal/mole})$	$\boldsymbol{K_2}$, $(\boldsymbol{Kcal/mole})$	$\boldsymbol{K_3}$, $(\boldsymbol{Kcal/mole})$	$\boldsymbol{K_4}$, $(\boldsymbol{Kcal/mole})$
H-C2-C1-H	0.0	0.0	0.30	0.0
H-C2-C1-C	0.0	0.0	-0.10	0.0
H-C2-C1-C2	0.0	0.0	0.30	0.0
H-C2-C1-C3	0.0	0.0	0.30	0.0
H-C1-C-O	0.0	0.0	0.00	0.0
H-C1-C3-H	0.0	0.0	0.30	0.0
C2-C1-C-O	0.0	0.82	0.00	0.0

C2-C1-C2-C1	1.30	-0.05	0.20	0.0
H-C3-C1-C2	0.0	0.0	0.30	0.0
C3-C1-C-O	0.0	0.82	0. 0	0.0
C1-C2-C1-C	-3.185	-0.825	0.493	0.0
C1-C2-C1-C3	1.30	-0.05	0.20	0.0
H-C1-C2-C1	0.0	0.0	0.30	0.0
H-C3-C1-C	0.0	0.0	-0.10	0.0

Table 2.5: Dihedral parameters for the PAA molecules used in the simulations

The potential energy for the improper torsional dihedrals is calculated by using the harmonic function:

$$U_{improper} = K_i(\varphi - \varphi_0)^2. \quad (2.7)$$

Here, φ_0 represents the equilibrium value of the improper torsional angle and K_i is the improper torsional stiffness. Their values for the C1-O-C-O system (corresponding to the PAA molecule) has been provided in Table 2.6. Kindly see Table 2.11 for the corresponding values associates with the PSS.

Improper Type	$\boldsymbol{K_i}$ $(\frac{\boldsymbol{Kcal}}{\boldsymbol{mol.rad^2}})$	$\boldsymbol{\varphi_0(deg)}$
C1-O-C-O	10.5	180

Table 2.6: PAA improper dihedral parameters used in the simulations

In the following five tables the non-bonded, bond, angle, dihedral, and improper dihedral parameters of PSS have been provided. These parameters are obtained from the OPLS-AA force field with the modifications suggested by Qiao et al. [80].

Atom Type	**Charge (e)**	**Mass (amu)**	$\boldsymbol{\epsilon}$ **(Kcal/mole)**	$\boldsymbol{\sigma}$ (Å)
C2	-0.12	12.011	0.066	3.50
H1	0.06	1.008	0.03	2.50
C1	0.055	12.011	0.066	3.50
C4	-0.115	12.011	0.070	3.55

C5	-0.115	12.011	0.070	3.55
C6	-0.115	12.011	0.070	3.55
H2	0.115	1.008	0.03	2.42
C7	-0.44	12.011	0.070	3.55
S (SO_3^-)	1.48	32.065	0.25	3.55
O (SO_3^-)	-0.68	15.999	0.17	2.96
C3	-0.18	12.011	0.066	3.50
O_w (H_2O)	-0.8476	15.999	0.155354	3.166
H_w (H_2O)	0.4238	1.008	0	0
Na	1.00	22.99	0.3526418	2.1595
Cl	-1.00	35.453	0.012785	4.83
Continuous LJ Wall (Parameters remain unchanged for interaction with all atom types)	0.00	15.00794	0.1947	3.00 (LJ cut off length is 3.36 Å)

Table 2.7: Charge, mass and LJ parameters for all the different atom types of PSS

Bond Type	$\boldsymbol{K_b}$, $(\frac{\boldsymbol{Kcal}}{\boldsymbol{mol}.\text{Å}^2})$	$\boldsymbol{r_0}$, (Å)
C2-H	340.0	1.09
C2-C1	268.0	1.529
C1-H	340.0	1.09
C1-C4	317.0	1.51
C4-C5	469.0	1.40
C5-H2	367.0	1.08
C5-C6	469.0	1.40
C6-H2	367.0	1.08
C6-C7	469.0	1.40
C7-S	340.0	1.77

S-O	700.0	1.44
C3-H	340.0	1.09
C3-C1	268.0	1.529
O_w-H_w	-	1.00

Table 2.8: PSS Bond parameters used in the simulations

Angle Type	$K_a, (\frac{Kcal}{mol.rad^2})$	$\theta_0(deg)$
H1-C2-H1	33.0	107.8
C1-C2-C1	58.35	112.7
C1-C2-H1	37.5	110.7
C2-C1-H1	37.5	110.7
C2-C1-C2	58.35	112.7
C2-C1-C3	58.35	112.7
C3-C1-H1	37.5	110.7
H1-C3-H1	33.0	107.8
C1-C3-H1	37.5	110.7
H1-C1-C4	35.0	109.5
C2-C1-C4	63.0	114.0
C3-C1-C4	63.0	114.0
C1-C4-C5	70.0	120.0
C5-C4-C5	63.0	120.0
C4-C5-H2	35.0	120.0
C4-C5-C6	63.0	120.0
C6-C5-H2	35.0	120.0
C5-C6-H2	35.0	120.0
C5-C6-C7	63.0	120.0
C7-C6-H2	35.0	120.0
C6-C7-C6	63.0	120.0
C6-C7-S	85.0	119.4

C7-S-O	74.0	107.2
O-S-O	104.0	119.0
H_w-O_w-H_w	-	109.47

Table 2.9: PSS angle parameters used in the simulations

Dihedral type	K_1, $(Kcal/mole)$	K_2, $(Kcal/mole)$	K_3, $(Kcal/mole)$	K_4, $(Kcal/mole)$
C2-C1-C2-C1	1.30	-0.05	0.20	0.0
H1-C2-C1-C2	0.0	0.0	0.30	0.0
H1-C2-C1-H1	0.0	0.0	0.30	0.0
C1-C2-C1-C3	1.30	-0.05	0.20	0.0
H1-C2-C1-C3	0.0	0.0	0.30	0.0
H1-C3-C1-C3	0.0	0.0	0.30	0.0
H1-C1-C3-H1	0.0	0.0	0.30	0.0
H1-C1-C2-C1	0.0	0.0	0.30	0.0
H1-C2-C1-C4	0.0	0.0	0.462	0.0
C1-C2-C1-C4	0.0	0.0	0.0	0.0
H1-C3-C1-C4	0.0	0.0	0.462	0.0
H1-C1-C4-C5	0.0	0.0	0.0	0.0
C2-C1-C4-C5	0.0	0.0	0.0	0.0
C3-C1-C4-C5	0.0	0.0	0.0	0.0
C1-C4-C5-C6	0.0	7.25	0.0	0.0
H2-C5-C4-C1	0.0	7.25	0.0	0.0
C4-C5-C6-H2	0.0	7.25	0.0	0.0
C4-C5-C6-C7	0.0	7.25	0.0	0.0
H2-C5-C6-H2	0.0	7.25	0.0	0.0
C7-C6-C5-H2	0.0	7.25	0.0	0.0
C5-C4-C5-H2	0.0	7.25	0.0	0.0
C6-C5-C4-C5	0.0	7.25	0.0	0.0
C6-C7-C6-H2	0.0	7.25	0.0	0.0

C5-C6-C7-C6	0.0	7.25	0.0	0.0
C5-C6-C7-S	0.0	7.25	0.0	0.0
H2-C6-C7-S	0.0	7.25	0.0	0.0
C6-C7-S-O	0.0	0.0	0.0	0.0

Table 2.10: PSS dihedral parameters used in the simulations

Improper Type	$\boldsymbol{K_i}\ (\frac{\boldsymbol{Kcal}}{\boldsymbol{mol.rad^2}})$	$\boldsymbol{\varphi_0(deg)}$
C5-C5-C4-C1	10.5	180
C6-C4-C5-H2	10.5	180
C7-C5-C6-H2	10.5	180
C6-C6-C7-S	10.5	180

Table 2.11: PSS improper dihedral parameters used in the simulations

2.4 Conclusion

In this chapter, we have demonstrated the effect of the monomer charge of PE brushes on the conformational change as a result of external electric field. We have considered two different pendant groups; carboxylate (PAA and PMAA) and sulfonate (PSS), carboxylate having a higher charge density. The axial electric field reduced the total end-to-end brush height for all PE brushes, interestingly, the end-to-end distance tells a different story. For PAA and PMAA, the end-to-end distance decreases with the application of an external electric field; this indicates a bending of the PE chains (bending is also visible from the brush profile). On the other hand, with the application of the applied axial electric field, the end-to-end distance of the PSS brush remains similar, the average chain profile shows that the brush tilts along the electric field. Stronger interaction of highly charged carboxylate monomer and counterion initiates an asymmetric ion distribution; this is associated with the electric field driven asymmetric migration of the counterion-monomer complexes, which results in bended brush conformation. For PSS, weaker monomer-counterion interaction implies that PE chains can be affected by the electric field independently and move along the direction of the electric field. The cumulative distribution function of counterion around PE chains, average brush profile, similarity analysis of chain supports our findings. This study will expand our understanding of PE under external field which can also influence future innovations.

Chapter 3. Quantification of Mono- and Multivalent Counterion-mediated Bridging in Polyelectrolyte Brushes[**]

Abstract: *Multivalent counterion-induced bridging interactions have been identified as the key mechanism of drastic collapse of the height of polyelectrolyte (PE) brushes. In this chapter, we employ all-atom molecular dynamics (MD) simulations to quantify the bridging interactions in PE brushes for counterions of different sizes and valences. We identify that unlike the current notion, bridging interactions are not the sole function of the counterion valence. Rather the bridging interactions depend on the fraction of counterions (of a given type) that get physically condensed on the PE backbone as well as the size of the counterion solvation shell. These mechanisms ensure that certain monovalent counterions demonstrate much stronger bridging interactions than that witnessed for certain divalent and trivalent counterions, while certain counterions of identical valences show drastically different bridging. We argue that these counterion-specific bridging interactions eventually enable not only the significant reduction of the PE brush height in presence of certain multivalent screening counterions, but may also give rise to scenarios where the brush height reduction for certain monovalent counterions is larger than certain divalent and trivalent counterions. This latter observation contradicts the experimental findings where the multivalent counterions invariably led to a larger decrease in the height of the PE brushes: we argue that this discrepancy stems from the fact that in our simulations we only consider densely grafted and short (and hence less flexible) PE brushes that hinder the formation of different laterally inhomogeneous structures (like pinned micelles and cylindrical bundles) that would have led to a larger brush height reduction (in experiments, which invariably consider longer and less densely grafted*

[**] Contents of this chapter is published in Macromolecules as Pial, T. H.; Sachar, H. S.; Das, S. Quantification of mono- and multivalent counterion-mediated bridging in polyelectrolyte brushes, *Macromolecules* **2021** 54, 4154.

brushes, the formation of such inhomogeneous structures are primarily responsible for larger brush height reduction in presence of multivalent counterions). Finally, we also probe the dynamic properties of the counterions (i.e., their time-dependent displacements) and their bridging interactions (i.e., lifetime of bridging interactions).

3.1 Introduction

Polyelectrolyte (PE) brushes, representing the "brush"-like configuration attained by a layer of densely grafted PE molecules in a good solvent [83], are known to have wide applications in sensing, current rectification, drug delivery, oil recovery, etc. [15-18,84-86]. The employability of the PE brushes in these applications stem from the fact that their structural properties, which in turn regulate these applications, can be tuned in response to numerous parameters such as the degree of polymerization, grafting density, solvent quality, concentration and nature of the counterions (that screen the charges on the PE backbone), concentration and nature of the added salts, etc. Ion specific effects (associated with the screening counterions and the added salts), namely the effects dictated by the sizes and valences of these ions, are found to be very important in different PE systems. For example, smaller ions lead to more compact PE structure [30-32]. Coarse-grained molecular dynamics (CGMD) simulations attributed this behavior to the smaller excluded volume effect of the smaller ions as well as the stronger interactions between the charged PE monomer and the smaller ions [30-32]. On the contrary, recent experiments on PE brushes demonstrated that larger divalent screening counterions lead to smaller PE brush height [33,34]: this points to the fact that ion-size-dependent trend of the size/compactness of the PE system may be more complicated than the simplified excluded-volume-effect-driven phenomenon arousing the need to better understand the interactions between a specific PE and a specific ion.

A more interesting observation, associated with the PE brush height, is made with respect to the influence of the valence of the screening counterion: PE brush layers are found to collapse in the presence of multivalent (divalent or higher valent) counterions, while such collapse does not occur for the case of monovalent counterions [33,34,47,87-94]. Motivated by the relevance of multivalent ions in the biological and other applications, there has been a tremendous interest to understand the mechanism of such multivalent-counterion-induced collapse of the PE brushes. It was initially hypothesized that replacement of monovalent counterions with multivalent counterions led to a reduced osmotic pressure of the counterions resulting in the formation of a compact brush [94]. Recently, however, it has been suggested that multivalent counterion mediated "bridging" is responsible for favorable interaction between like-charged polyelectrolytes, which in turn leads to collapse of the PE brush layer [47, 93-96]. This bridging interaction, which is characterized by two or more like-charged atoms being inside the solvation shell of a particular counterion, has been mainly attributed to the presence of multivalent counterions. Interestingly, in addition to these studies, there are also studies that report favorable interactions between like-charged systems even in presence of monovalent counterions. For example, anionic surfactants adsorb at negatively charged mica in presence of Cs^+ (Ref. 35) and K^+ (Ref. 36) counterions. These interactions, while not identified or quantified specifically, appear to be equivalent to bridging interactions. Along with such apparent contradiction where even monovalent counterions appear to induce bridging interactions, a comprehensive quantitative understanding of the counterion-mediated bridging for different types of counterions has been missing. Such an understanding, which will pinpoint not only the different factors that regulate the bridging but also the relative contributions of the different types of bridging (e.g., interchain versus intrachain bridging) for different types of counterions (including monovalent counterions), will eventually enable

designing PE systems that can be manipulated more easily for different purposes.

In this chapter, we have employed all-atom MD simulations to quantify and dissect the counterion-induced bridging for different screening counterions (varying in sizes and valences) in a densely grafted PE brush system with short PE brushes. In addition, in order to observe the effect of an external salt we have simulated two sets of systems: with no salt and with 0.4 M concentration of added chloride salt of the corresponding screening counterions. Our findings confirm the occurrence of three types of interactions: nearest neighbor condensation, intrachain bridging, and interchain bridging. We identify the relative occurrences of these three interactions in PE brush system with screening counterions of different sizes and valences. We further establish that even *monovalent counterions* can trigger substantial amount of bridging. Furthermore, we identify that the presence/absence of condensed (on PE backbone) counterion (and the manner in which they screen the PE charges) and the size of the solvation shell of the counterions govern these specific counterion-size and counterion-valence dependent bridging behavior. We also establish that such specific counterion-valence-dependent bridging behavior ensures that the brush height for the case of certain monovalent counterions can be smaller than that with certain specific divalent and trivalent counterions. Therefore, we contradict the accepted notion (derived from experimental findings) that multivalent counterions will always reduce the brush height much more significantly than the monovalent counterions. We argue that this discrepancy in the counterion-valence-dependence of the PE brush height stems from the fact that in our simulations we only consider densely grafted and short (and hence less flexible) PE brushes that hinder the formation of different laterally inhomogeneous structures (like pinned micelles and cylindrical bundles) that would have led to a larger brush height reduction. On the contrary, experiments are conducted with much longer and less densely grafted brushes, where these inhomogeneous structures are present and are

primarily responsible for larger brush height reduction in presence of multivalent counterions. Finally, we also probe the dynamic properties of the counterions within the PE brush layer. We demonstrate the effect of the counterion type on the time-dependent mean-squared displacements of the counterions within the brush layer and quantify the lifetime of the bridging interactions as a function of the type of counterions.

3.2 Results and Discussions

In our system [shown in Fig. 3.1(a)], fully ionized Polyacrylic acid (PAA) chains (H[-CH2-CH(COO-)-]nCH3) are used as the PEs and explicitly modeled SPC/E water (67) molecules act as the solvent. Different screening counterions, namely Li^+, Na^+, Cs^+, Mg^{2+}, Ca^{2+}, Ba^{2+}, Y^{3+}, La^{3+} are separately considered to neutralize the polyelectrolyte (PE) segmental charge. No external salt was added in the system in one case. Consideration of such an external salt-free system is essential to eliminate the effect of salt induced osmotic pressure, thereby ensuring that one can solely focus on the effect of the size and valence of the screening counterions in triggering the bridging interactions. Additionally, we have conducted simulations for another system, where we have considered a 0.4 M concentration of added salt (which is the chloride salt of same counterions as the screening counterions). This implies that for the case with Li^+ screening counterions, we added a 0.4 M concentration of LiCl salt, for the case with Mg^{2+} screening counterions, we added a 0.4 M concentration of $MgCl_2$ salt, and so on. For both set of systems (with and without the added salt), PE chains are grafted with a grafting density of $0.05/\sigma^2$ [σ=3.5 Å is the Lennard Jones (LJ) distance parameter of the backbone carbon atoms of the PE chains]. Each chain has 49 backbone carbon atoms (24 repeating units). Further details about the simulation have been provided in the Methods section.

Brush Height

We first study the end-point brush height for each type of screening counterion: we obtain a non-monotonic variation of the brush height as a function of counterion size and valence [see Fig. 3.1(b)], although the brush height variation for different counterions is small in all our simulations. This small variation can be attributed to the considerations of high grafting density as well as shorter PE chains (on account of computational resource constraints). The high grafting density ensures that the excluded volume of the PE chains is more dominant than the electrostatic effect, which leads to a lesser freedom for the PE brushes to change their configurations [96]. It is also known that shorter chains are relatively stiffer than longer chains [97,98]. This reduced flexibility of our simulated brushes can be inferred from the high persistence length (ranging from 11.8 Å to 15.71 Å) of the simulated brushes for the cases of different counterions with and without the added salt (please see table B2 and associated discussion in Appendix B). For more densely grafted and stiffer PE brushes, the brush heights do not change very significantly on varying the type of counterions. Furthermore, due to the fact that the brushes are densely grafted and stiffer, we only observe homogeneous collapse and not heterogeneous collapse. Yu et al. [93] had demonstrated that PE brushes, in presence of multivalent counterions, might undergo heterogeneous collapse (this refers to the collapse of the brush height in presence of the formation of heterogeneous structures, similar to pinned micelles and cylindrical bundles). Also, besides this small variation in the brush height for different types of counterions, most interestingly, for Mg^{2+}, Ca^{2+}, and La^{3+} counterions, the brush height is greater than that with monovalent counterions. This contradicts the current notion that the multivalent counterions always lead to a much larger decrease in the PE brush height as compared to the monovalent counterions [47,93]. Given that the total charge of the added counterions should be equal to the total charge of the PAA brushes,

the number of multivalent counterions is always less than the number of the negatively charged atoms of the PAA brushes. This leads to an incomplete neutralization of the local PE charged monomers (i.e., these monomers are surrounded only by the water molecules and not the counterions), although in total the brush layer is rendered charge neutral; accordingly, there arises local monomer-monomer repulsion, which hinders the multivalent-counterion-driven brush height reduction. As already pointed out, a higher grafting density and stiffness (because of the short chains) hinders the formation of different laterally inhomogeneous structures (like pinned micelles and cylindrical bundles [99]), which would have helped the brushes to be more charge neutral and have smaller thickness. Later in the paper, we will see that neutralization by bridging helps some counterions to render shorter brushes. Even with the added salt (0.4 M concentration of the chloride of the corresponding counterions), this trend of the end-to-end brush height as function of the valence of the counterions (as described above) remains similar (please see appendix B). The added salt reduces the brush height slightly (as compared to the no-salt case) for all the counterions considered here. The presence of the added salt creates an additional osmotic pressure outside the brush in the bulk, which leads to this slight brush height reduction (as compared to the no-salt case), although this overall trend where the brush height can be larger for certain multivalent counterions (e.g., Ca^{2+}, Mg^{2+}, and La^{3+}) as compared to the brush height for monovalent counterions, is not altered. From these results we can infer that this trend where the multivalent ions invariably reduce the brush height as compared to the case with monovalent ions is only true for sufficiently long, flexible, and less densely grafted brushes that are typically studied in experiments [93]. For example, in experiments [93] one uses PE chain with degree of polymerization in the order of 1000 monomers grafted with a grafting density of 0.1 to 0.025 chain/nm^2 in a highly grafted scenario, while in the present case, degree of polymerization is 24

and grafting density is 0.408 chain/nm^2. Furthermore, in the CG MD calculations corresponding to this experiment, a persistence length of 2.3 Å was considered; on the other hand, the persistence length calculated in our simulations ranged from 11.8 Å to 15.71 Å. Such long and less stiff PE chains considered in the experiments led to the formation of laterally inhomogeneous structures like pinned micelles and cylindrical bundles, which in turn led to a significant multivalent-counterions-driven brush height reduction; for shorter and densely grafted brushes (as considered for our simulations), where the formation of these inhomogeneous structures are prevented, this trend may get reversed for certain choices of multivalent and monovalent counterions. Below, we shall discuss the effect of the bridging in this overall height reduction of the brushes and the manner in which the counterion-dependence of the bridging explains this non-monotonic trend in the variation of the brush height with the valence of the counterions.

Bridging Interactions

To check the presence of the bridging, we define the first solvation shell of a counterion by taking the first valley of the $O_{Carboxylate}$-counterion radial distribution function (RDF) ($O_{Carboxylate}$ refers to the oxygen atoms of the COO^- functional group of the PAA monomers). These RDFs corresponding to all the counterions are provided in the appendix B. If there is one or more $O_{Carboxylate}$ from the PE monomer inside the first solvation shell of a counterion, we consider this counterion to be condensed on the PE chain. We categorize this condensed counterion in three groups following Yu *et al.* [93]: counterions contributing to (1) nearest neighbor condensation, (2) intrachain bridging, and (3) interchain bridging. If the $O_{Carboxylate}$ atoms inside the solvation shell of a counterion are from a single monomer or from two neighboring monomers of a particular PE molecule, we identify it as the occurrence of "nearest neighbor condensation". If $O_{Carboxylate}$ atoms are from two different non-neighboring monomers, the corresponding counterion is identified to

trigger intrachain bridging (if the monomers belong to the same PE chain) and interchain bridging (if the monomers belong to the different PE chains). These definitions are schematically represented in Fig. 3.1(c). In Fig. 3.1(d), the relative extent of different bridging contributions for different counterions (or the number of counterions of a particular type that contribute to any of the three phenomena described above) has been provided. This is the central result of this chapter. *Our results confirm that bridging is not a strictly counterion-valence-driven phenomenon and it does not increase monotonically with an increase in the counterion valence.* For each type of studied counterion there is a substantial amount of intrachain bridging. What is more interesting is interchain bridging: it ranges from almost being negligible for Mg^{2+} counterions to being 27% for Na^{+} counterions. In fact, for monovalent counterions, we find that at least a small amount of interchain bridging is present for a wide range of counterion sizes (i.e., for Li^{+}, Na^{+}, and Cs^{+}). Very interestingly, however, despite some noticeable variation in the amount of interchain and intrachain among the different types of monovalent counterions, we find relatively less difference among the corresponding brush heights. For the case of monovalent counterions, there is a parity (approximately) in the number of counterions and charge-bearing monomers inside the brushes, which ensures efficient screening of the monomer charges even in the absence of interchain/intrachain bridging. Thus, the impact of inter/intrachain bridging on the local neutralization of monomers is relatively small for the case of monovalent counterions; accordingly, the extent of variation in the brush height for the cases of different monovalent screening counterions is relatively less even though there is a significant variation in the extent of bridging (interchain and intrachain) corresponding to these different monovalent counterions.

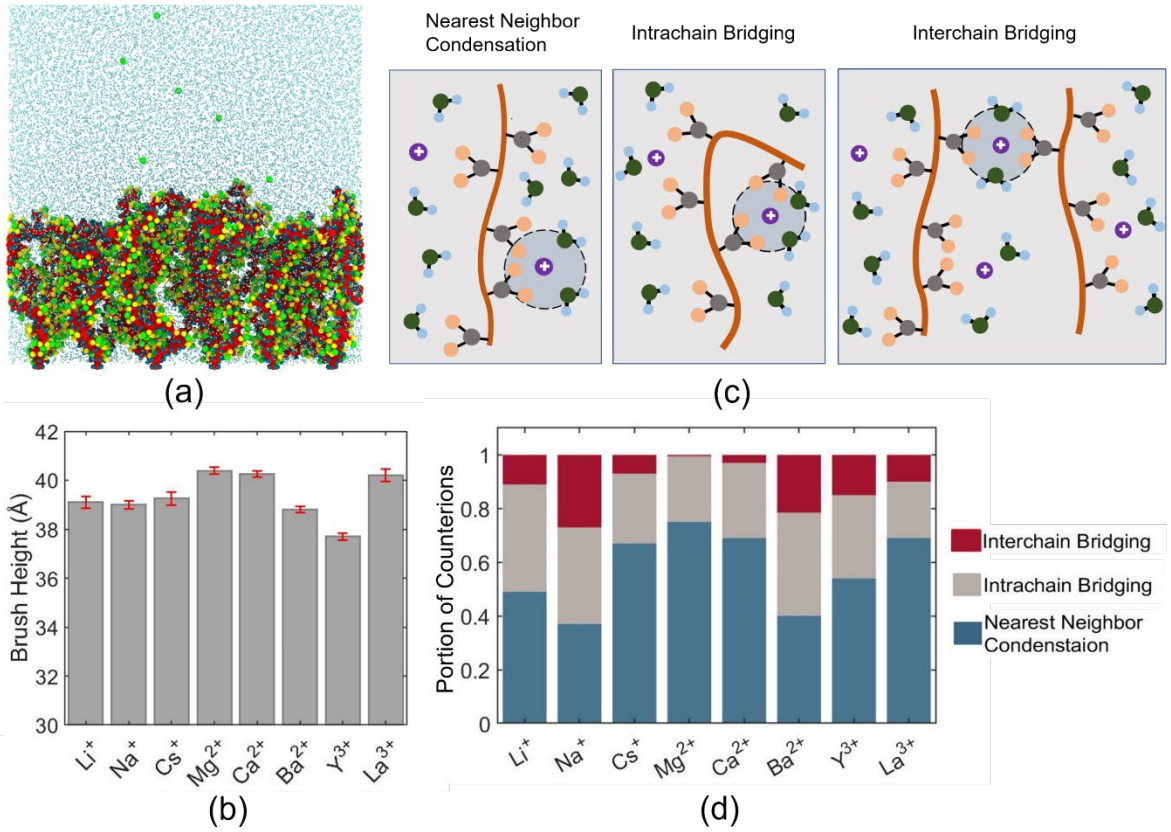

Figure 3.1: Snapshot, brush height and bridging interaction. (a) Snapshot (truncated from the top) of the simulation system. Green circles are the counterions. Other circles are atoms of PE. Green small dots indicate water. (b) End-to-end PE brush height for different counterions for the case of no added salt. The error bars in the plot are obtained from the fluctuations of the average brush height over the period in which the data is produced. (c) Schematic of different types of bridging. Purple circles indicate counterions, while the surrounding gray dashed circles indicate the first solvation shells of these counterions. It can be seen that oxygen atoms from water (teal circles) and carboxylate of PE (golden circles) are inside the solvation shell of a counterion. (d) Percentage of counterions participating in different types of bridging for different types of counterions for the case of no added salt

For smaller divalent counterions like Mg^{2+} and Ca^{2+}, there is almost no interchain bridging and only Ba^{2+} demonstrates 22% interchain bridging. Accordingly, the brush height is very similar for the cases corresponding to Mg^{2+} and Ca^{2+} counterions but much smaller for the case of Ba^{2+} counterions. Finally, for trivalent counterions, both interchain and intrachain bridging are more pronounced for Y^{3+} counterion than La^{3+} counterion, leading to much reduced brush height for the case corresponding to Y^{3+} counterion as compared to the case corresponding to La^{3+} counterion. Such non-monotonic bridging interactions will be discussed later. The brush height closely follows these trends in intrachain and interchain bridging interactions since enhanced bridging interactions enable a counterion to neutralize a greater number of negative monomers of the PE chain, which in turn reduces the monomer-monomer repulsion and therefore lowers the brush height. Therefore, the brush height is smallest for the cases of Ba^{2+} and Y^{3+} counterions among the studied cases of divalent, and trivalent counterions, respectively stemming from the fact that interchain and intrachain bridging interactions are maximum for these particular ions (among the ions of specific valence). As has been already pointed out earlier, for the case of multivalent counterions, the number of brush-trapped counterions is significantly lower than the number of charge-bearing monomers of the grafted PE chains. This leads to an incomplete neutralization of the monomer charges at the local length scales. As a result, there is an increase in the magnitude of intersegmental repulsions associated with the PE chains, thereby leading to an enhanced brush height. Therefore, for such cases, the interchain and intrachain bridging serve as a much more dominant mechanism (as compared to the case of monovalent counterions, where an approximate parity in the number of counterions and charge-bearing monomers inside the brushes ensures an efficient screening of the monomer charges even in the absence of interchain/intrachain bridging) to mitigate the issue of incomplete neutralization of the PE segments by screening a greater number

of charge-bearing monomers, which can reduce the electrostatic repulsion between the PE segments. That is why we observe a considerable reduction in the PE brush height (with either divalent or trivalent screening counterions) with increasing contribution of interchain and intrachain bridging interactions in the divalent and trivalent counterions.

To explain such non-monotonic bridging contributions, we study the distributions of the counterions within the PE brush layer for different counterions. Accordingly, in Fig. 3.2(a), we depict the probability density distribution [ρ(r)] of finding the nearest $O_{Carboxylate}$ atom at a distance r from a given counterion. For all types of counterions, the distance of the first peak in the corresponding probability density distribution closely resembles the size of the counterions, as elucidated in Table B.1 in appendix B. For those counterions (e.g., Li^+, Na^+, Ca^{2+}, Ba^{2+}, and Y^{3+}), where there exists only a single peak in their ρ(r), given the fact that the location of this peak is very close to the size of these counterions, we can infer that these ions condense almost fully on the PE backbone. Interestingly, for Cs^+, Mg^{2+} and La^{3+} counterions, *second peaks* in their ρ(r) are observed [see inset of Fig. 3.2(a)]. *Therefore, we can infer that a fraction of these counterions (Cs^+, Mg^{2+} and La^{3+}) physically condense on the PE chain, while the remainder of these counterions remain non-condensed.* The distances of the locations of these second peaks in the ρ(r) of these ions (Cs^+, Mg^{2+}, and La^{3+}) are close to distance of location of the second peak in the corresponding (*i.e.*, the case with these counterions) $O_{Carboxylate}$-H_{water} RDF (or the distance of H_{water} or hydrogen of the water molecule from the $O_{Carboxylate}$ in the second solvation shell of $O_{Carboxylate}$) [see Fig. 3.2(b)]. As a result, these ions (Cs^+, Mg^{2+}, and La^{3+}) will be able to replace some of the H_{water} atoms from the second solvation shell of the $O_{Carboxylate}$ atom; this will imply that these counterions will be able to neutralize COO^- by replacing some H_{water} from the second solvation shell of the $O_{Carboxylate}$ atom. Therefore, these counterions screen the PE charges by a combination

of physical condensation on the PE backbone and screening the charge from a non-condensed state by replacing some H_{water} atoms at the location of their (counterions') second solvation shell.

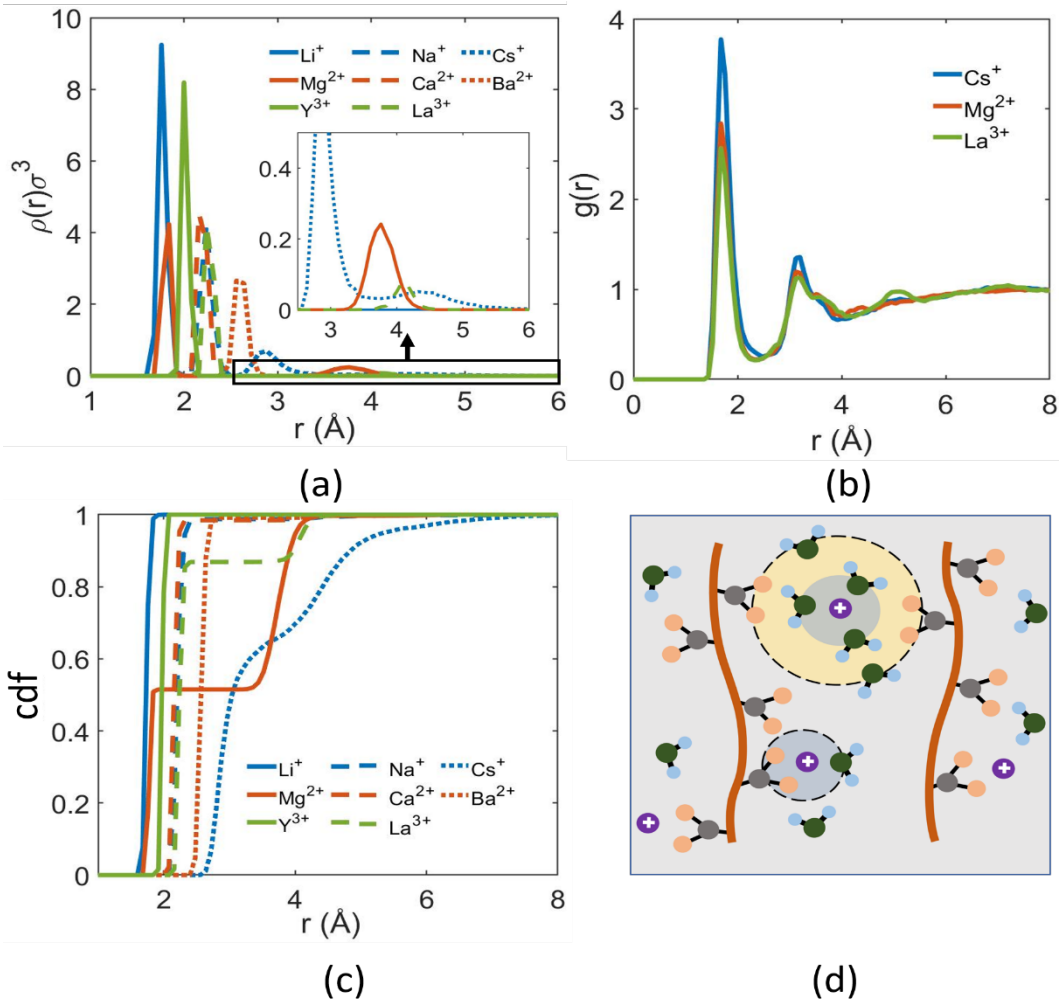

Figure 3.2: Counterion distribution around PE. (a) Normalized probability distribution [$\boldsymbol{\rho(r)}$] of finding the nearest $O_{Carboxylate}$ atom around different counterions within the PE brush layer. Region around the second peak (occurring for the cases of Cs^+, Mg^{2+}, and La^{3+}) has been magnified in the inset. (b) $O_{Carboxylate}$-H_{water} RDF for system with different counterions. (c) The cumulative distribution function (cdf) [$\text{cdf}(\boldsymbol{r}) = \int_0^r \boldsymbol{4\pi r^2 \rho(r) dr}$] for different counterions. The results are for the case of no added salt. (d) Schematic showing $O_{Carboxylate}$ from different PE chains in the second solvation shell (shown in yellow) of a non-condensed (Cs^+, Mg^{2+}, and La^{3+}) counterion (shown in yellow circle). These $O_{Carboxylate}$ in the second solvation shell of these counterions are too far from each other to take part in any bridging interactions. These $O_{Carboxylate}$ in the second solvation shell of these counterions are too far from each other to take part in any bridging interactions.

In figure 3.2(c), we plot the cumulative distribution function (cdf) [100] obtained by integrating the probability density over a sphere of radius r. This provides the overall probability for the case of no added salt of finding the nearest $O_{Carboxylate}$ atom within a distance r from a given counterion. For counterions that have only one clear peak in ρ(r) (e.g., Li^+, Na^+, Ca^{2+}, Ba^{2+}, and Y^{3+}), cdf becomes equal to unity at the "r" value that corresponds to the location of the single peak [see Fig. 3.2(a)], providing further demonstration that these counterions screen the PE charges entirely by condensation on the PE backbone. On the other hand, for Cs^+, Mg^{2+}, La^{3+} cdf is less than unity at the location of the first peak [of their ρ(r)] and becomes unity only at that *r* value where the second peak [of their ρ(r)] ends.

The above results indicate that unlike Li^+, Na^+, Ca^{2+}, Ba^{2+}, and Y^{3+} ions, a large portion of the Cs^+, Mg^{2+}, La^{3+} ions are not fully condensed on the PE backbone at a distance equal to the size of these ions. Interestingly, the cases of Cs^+, Mg^{2+}, La^{3+} ions correspond to the lowest bridging interactions for their corresponding valences. To trigger the bridging interactions, $O_{Carboxylate}$ from different monomers need to be inside the first solvation shell of a counterion that has already condensed on a PE chain. On the other hand, counterions that are not entirely condensed on the PE chain [i.e., some of the Cs^+, Mg^{2+}, La^{3+} counterions] can accommodate $O_{Carboxylate}$ from non-neighboring PE monomers in these counterions' second solvation shell [see Fig. 3.2(d)] and ensure that charges of some of these PE monomers are already partially neutralized by these non-condensed counterions in their second solvation shell. Possible replacement of H_{water} atoms from the second solvation shell of the $O_{Carboxylate}$ atom by these counterions (see above) will aid in such neutralization. Under these circumstances, $O_{Carboxylate}$ atoms from non-neighboring monomers have a lesser tendency to enter the first solvation shell of a condensed Cs^+, Mg^{2+}, and La^{3+} counterion (i.e., that fraction of Cs^+, Mg^{2+}, and La^{3+} counterions that are condensed on the PE backbone). Of

course, this partial neutralization of the monomer charge by these non-condensed Cs^{+}, Mg^{2+}, and La^{3+} counterions in these counterions' second solvation shell will ensure that the monomers remain far apart, which in turn will hinder bridging interactions. To confirm this, we have calculated the probability of having $O_{Carboxylate}$ from different PE chains in the second solvation shell of Mg^{2+} (this is similar to the interchain bridging, but using the second valley of the RDF as cutoff distance instead of the first valley). We have found that 53% of the non-condensed Mg^{2+} counterions have $O_{Carboxylate}$ from different PE chains, while 31% of the condensed Mg^{2+} counterions have $O_{Carboxylate}$ from different PE chains. This confirms that in the process of neutralizing the PE charge by the non-condensed counterions (from their second solvation shell), it is ensured that a significant number of monomers remain far apart so that they cannot participate in bridging interactions. This explanation is schematically shown in Fig. 3.2(d).

Other than having the ability to condense on the PE chain, another important factor determining the bridging is the counterion solvation number. Counterion solvation number indicates how many O atoms (from water or charged carboxylate) are present inside the first solvation shell of the counterion. When counterion size increases, their solvation shell gets larger which can accordingly accommodate a greater number of oxygen atoms, leading to a larger solvation number. This variation in the counterion solvation number, for both the cases of the counterion inside the brush layer as well as the counterion in the bulk (i.e., outside the brush layer), as a function of the nature of the counterion, has been provided in Fig. 3.3. The counterion solvation numbers in the bulk water are in good agreement with previous findings [101-107]. It can be further observed that the counterion solvation number inside the brush layer is similar to the counterion solvation number in bulk for the different types of counterions considered here. However, a key difference is that while in the bulk the counterions are solvated or neutralized by

the water, inside the brush layer some of the $O_{Carboxylate}$ replace water molecules from the counterion solvation shell. This replacement of water in the solvation shell of a counterion by $O_{Carboxylate}$, which is analogous to the "water in salt" phenomena [108], is observed inside the brush layer for all the different types of counterions considered here (see Fig. 3.3). In this context, it is useful to discuss the favorable entropy changes associated with such replacement of water molecules from the counterion solvation shell by $O_{Carboxylate}$ inside the PE brush layer. Water molecules lose considerable entropy while solvating the counterions, thereby reducing the free energy of the system. Thus, a greater number of water molecules participating in the solvation process (i.e., being present inside the first solvation shell of a counterion) is unfavorable to the system from an entropic point of view. Therefore, such replacement of water molecules from the counterion solvation shell by $O_{Carboxylate}$ inside the PE brush layer will imply the release of water molecules from their 'solvation duties' inside the grafted PE layer (with the carboxylate oxygen atoms, which do not undergo significant change in their mobilities as they enter the counterion solvation shell, serving as their replacements) in an attempt to further reduce the free energy of the PE brushes-counterion-water system. The release of each water molecule can contribute approximately $-1k_BT$ to the total free energy of the system, thus signifying the important role played by the entropic effects in conjunction to the enthalpy mediated screening of the PE functional groups (via counterion condensation).

When the counterions can be condensed on the PE chain, the counterion size and the consequent counterion solvation number become important factors for dictating the bridging interactions. For example, when the counterion size and the consequent solvation number are small, a lesser number of O atoms can be present inside the first solvation shell of a counterion, which in turn hinders the formation of a bridge. For example, Li^+ and Na^+ ions are both condensed

on the backbone of PE chain [see Fig. 3.2(a) and the associated discussions]; however, as its solvation shell cannot accommodate enough O atoms to form more bridges, there is a lesser chance for Li^+ ion to form bridging interactions. On the other hand, for Na^+ counterion, which can accommodate a greater number of O atoms, bridging is enhanced. In Fig. 3.3, the solvation from $O_{Carboxylate}$ (O_{PE}) is similar for Li^+ and Na^+. However due to the smaller solvation shell of the Li^+ ion, the $O_{Carboxylate}$ present within the Li^+ ion solvation shell is only from the same or nearby monomers; accordingly, we do not see significant bridging interaction for the case of Li^+ ion. On the other hand, a larger solvation shell (larger total solvation number) makes it possible for the Na^+ ion to bring $O_{Carboxylate}$ from non-neighboring monomers and therefore trigger a more pronounced bridging interaction. This same larger total solvation number helps Cs^+ to bring $O_{Carboxylate}$ from non-neighboring monomers and form bridge. Here it should be mentioned that this solvation number is calculated for all the counterions inside brush layer; therefore, the non-condensed counterions also contribute to the lesser number of $O_{Carboxylate}$ solvation number for Cs^+. The same scenario plays out for divalent counterions: Ca^{2+} and Ba^{2+}. The ability to accommodate a greater number of O atoms from non-neighboring monomers makes Ba^{2+} ion, with a larger solvation shell, more capable of supporting the bridging interactions as compared to the Ca^{2+} ion (having a smaller solvation shell). For the trivalent counterions, such larger solvation shell (and hence a larger solvation number) driven enhanced bridging is possible for La^{3+} counterions. Therefore, a higher solvation number helps to trigger substantial bridging interactions in Cs^+ and La^{3+} counterions despite these ions not having condensed fully on the PE backbone. Therefore, very interestingly, for Cs^+ and La^{3+} ions, there are two countering factors, where one factor (presence of non-condensed counterions) hinders bridging, while the other factor (larger sizes of the ions) aids in bridging.

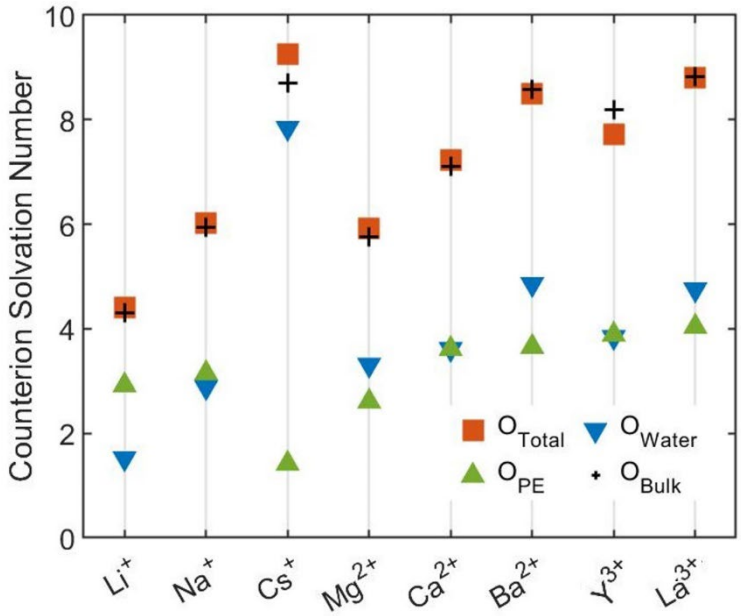

Figure 3.3: Solvation number of different counterions. "O_{Total}" represents the solvation number of the counterions inside the PE brush layer. "O_{Total}" is constituted by the combination of O_{Water} (the number of water molecules in the first solvation shell of the counterion) and O_{PE} (number of $O_{Carboxylate}$ atoms inside the first solvation shell of the counterion). Finally, "O_{Bulk}" represents the solvation number of the same counterions in the bulk.

Dynamics of the Counterions

Finally, we want to observe the dynamic behavior of the counterions inside PE brush layer. From previous all-atom MD simulation studies on PE brushes [100,108], it is known that the mobilities of the counterions inside the PE brush layer get significantly reduced in comparison to their bulk mobility values due to the steric effects and the electrostatic attraction from the PE molecules. This is reflected in a significant reduction of the mean square displacement (MSD) values of the counterions within the brush layer as compared to their MSD values in the bulk. Here we want to study to what extent these MSD values vary for different counterions. Fig. 3.4(a) shows that with increasing valence, MSD of the counterions inside the PE brush layer reduces, which can be attributed to the stronger binding of the larger-charged counterions to the PE. As Cs^+ is not fully condensed and some of them are not bound to the PE, they can move more freely than the

counterions that are completely bounded to the PE; as a result, the averaged MSD for the Cs^+ ion is much larger (the result is shown in the inset).

We have also probed the dynamic relaxation time of the bridging interactions of the counterions [see Fig. 3.4(b)]. For this analysis, we chose three counterions with highest interchain bridging interactions: Na^+, Ba^{2+}, and Y^{3+}. This dynamic interaction is quantified by calculating the average residence time of an interchain bridge. This residence time $[R(t)]$ is calculated from the time correlation function defined as:

$$R(t) = \frac{1}{N_h}\sum_{i=1}^{N_h} \theta_i(t_0)\theta_i(t_0 + t). \qquad (3.1)$$

Here θ_i is the Heaviside unit step function (if one counterion forms an interchain bridge with few $O_{Carboxylate}$ and maintains the same bridging interaction, θ_i =1; otherwise, θ_i =0), N_h is the number of counterions forming inter-chain bridging, and t_0 is the initial time step. If some $O_{Carboxylate}$ atoms were present outside the bridge for less than 20ps, we did not consider it as bridge breaking. $R(t) = 1/e$ can be taken as the relaxation time of the bridging interaction. It can be observed that with increasing valence, the bridges become more stable and they decay or break much less frequently. Stronger interactions between the PE and counterions with higher valence make the residence time of the bridge much larger [see Fig. 3.4(b)]. This behavior agrees with previous literature [109] which suggested that relaxation in a system with trivalent counterions is much slower than monovalent counterions.

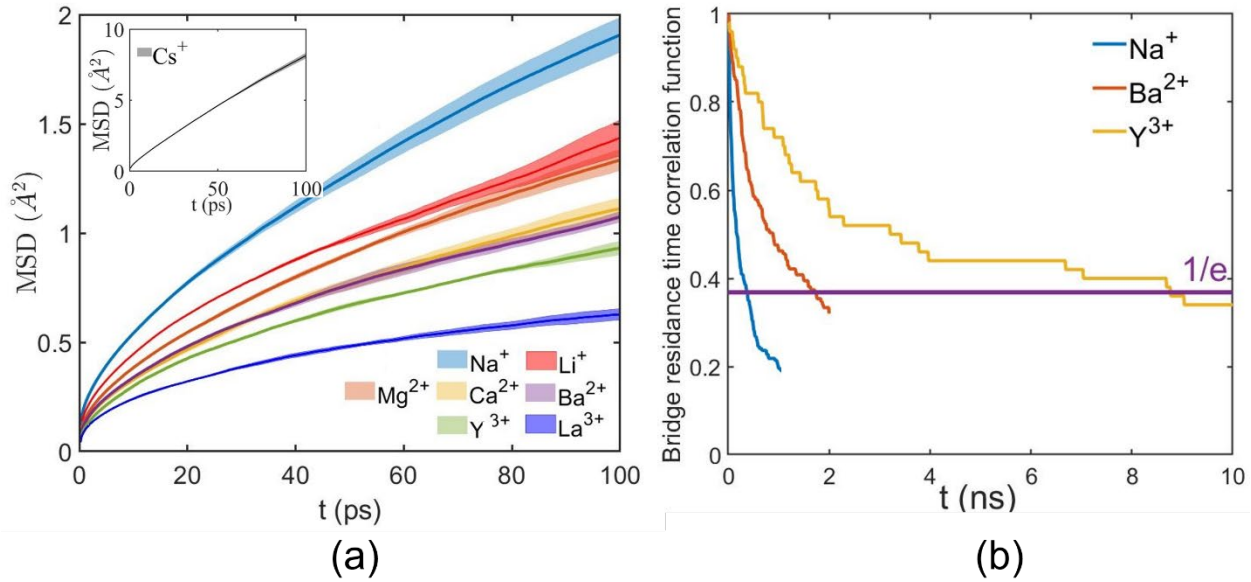

Figure 3.4: Dynamics behavior. (a) MSDs of the different counterions inside the PE brush layer. MSD for the Cs^+ counterion is shown in the inset for better visualization. (b) Bridge residence time correlation function for three different counterion. Relaxation time is shown by the purple line. The results are for the case of no added salt.

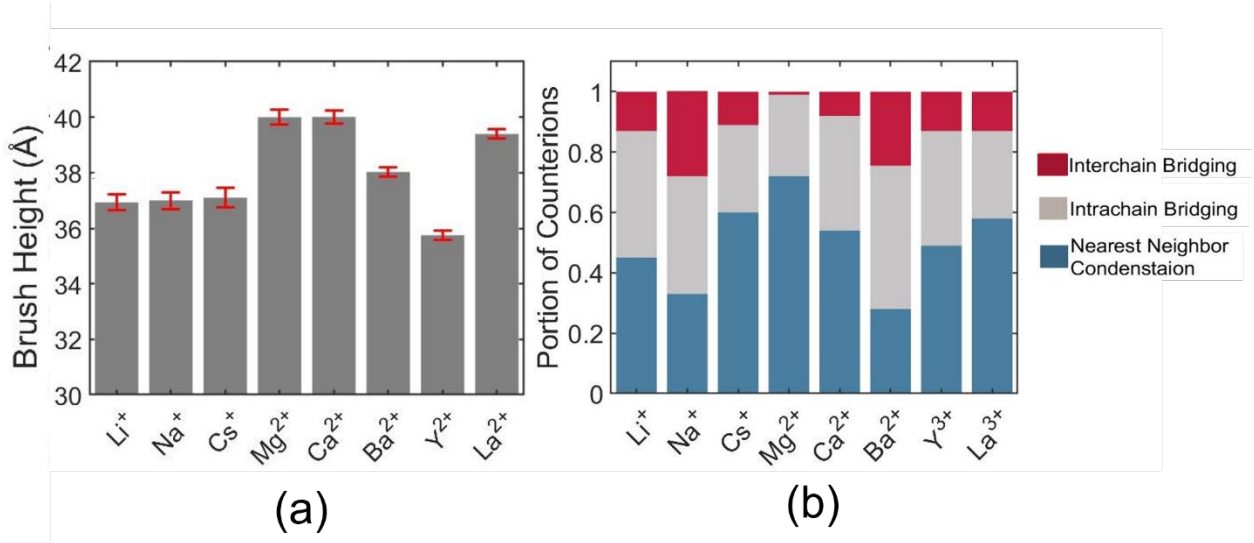

Figure 3.5: The results for the case with an added salt. (a) End-to-end brush height for different counterions. (b) Percentage of counterions participating in different types of bridging for different types of counterions. The results are for the case when there is an added salt (0.4 M concentration of the chloride salt of the corresponding counterions).

Discussion

Here the two main results (the PE brush height and the percentage of counterions participating in different types of bridging interactions) for simulations with 0.4 M concentration of the chloride salt (of the corresponding counterions) is presented. It can be observed that the trends of the brush height and bridging interaction remain almost same as the simulations without salt.

Finally, we want to paint a generic picture from our analysis on the role of the counterion valence and size on the overall bridging interactions and the resulting changes in the brush height. Counterion valance and size are indeed two of the most important parameters for determining the bridging interactions and thereby significantly affecting the brush height. With increasing valance, the number of counterions required to neutralize the charged monomers decreases. As a result, the effect of counterion mediated bridging on the brush height becomes more important. In other words, for a given extent of counterion-mediated bridging interactions, the variation in brush height for monovalent counterions is modest while multivalent counterions produce much larger differences in brush height. Size of the counterions dictates their tendency for condensation on the PE chains as well as their solvation number. These two factors, on the other hand, dictate the overall extent of the bridging interactions. For example, an incomplete condensation enforces the PE monomers to remain far apart, thereby hindering the bridging interactions. Counterion condensation on the PE chains also depends on the specific interactions between the monomers and counterions. For example, counterion condensation on the sulfonate group (a common pendant group for PE chains is the sulfonate group) can be considerably different from condensation on the carboxylate group as the charge density of these two pendant groups is different. Furthermore, solvation number of the counterions increases with their size, and a higher solvation number helps

to create more bridging interactions. Larger size and higher solvation number of the counterions can lead to a smaller brush height if the counterions can condense on the charged monomers (by replacing water molecules in the first solvation shell of the PE functional groups). However, this behavior is not exhaustive: for example, counterion and monomer specific energetics as well as the structure of the complex formed by the counterions, monomers and water molecules (with all of these depending on the counterion size and valence) can also be important factors in dictating the brush height.

The effect of the excluded volume (EV) interactions and ion solvation [110] of the counterions as well as the phobicity/philicity (of the polyelectrolytes) to the solvent on the conformations of free PEs and PE brushes have been extensively explored by coarse grained (CG) MD simulations. It is critical, therefore, to place the key findings of our all-atom MD simulations in the context of these CG MD simulation results. For example, for free PE chains, CG MD simulations have revealed that increasing the size of the counterions leads to a higher value of the radius of gyration of the PE chain [31,32]. When the counterion size becomes very large as compared to the PE monomer size (i.e., the case of bulky counterion), the counterion-PE Coulomb interactions become weaker and the large EV effects of the bulky counterion makes the chain swollen. On the other hand, CG simulations show that smaller counterions interact with the PE chains more strongly leading to a denser chain. CG simulations have also revealed similar ion-size-dependent effects even for the PE brushes. It is found that a smaller counterion leads to a compact brush structure compared to the larger counterion [30]. In these studies, the EV effect was found to be important as the range of the ratio (σ_c/σ_m) of the size of counterion (σ_c) to the size of the PE monomer (σ_m) lay between 0.5 to 3. On the contrary, when one considers only metal ions, this ratio σ_c/σ_m becomes very small as the size of the metal ions are very small compared to the

monomer molecules. For such cases, therefore, as revealed by CG MD simulations, ion-specific interactions between the metal counterions and the PE brushes became critical with relatively less influence of the ion EV interactions [33,34]. One such ion-specific interaction is ion solvation effect: a combination of the counterion size and the counterion charge (or valence) dictates the extent of solvation of that ion and to what extent the ions can successfully interact with the PE brushes. A combination of experiments and CG MD simulations established that valence dependent ion-specific interactions with the PE brushes eventually triggered the generation of laterally inhomogeneous structures like pinned micelles and cylindrical bundles for the case of certain multivalent counterions leading to a drastic brush height reduction for such multivalent counterions [92]. For our case of all-atom MD simulations, we too are able to explicitly capture the ion-specific interactions of the metallic (hence very small and with negligible EV interactions effects) screening counterions with the PE brushes. However, unlike experiments and CG simulations, we consider PE brushes that are very densely grafted and are significantly shorter (and hence less flexible). Accordingly, we do not encounter the occurrences of the inhomogeneous structures that would have led to a significant brush height reduction: therefore, for our case, the brush height varies non-monotonically with the counterion valence and is dictated by the ion-specific bridging interactions.

Similar to the role of counterions, the role of the solvent in causing the changes in the configurations of the PE brushes have been studied in details. For example, Ref. 111,112 delineated the effect of poor solvent in generating various morphologies in collapsing (forming different types of aggregates) PE brushes. Interestingly, recent analysis by Jackson et al. [92] has compared the multivalent-counterion-mediated brush collapse *versus* the poor-solvent-mediated brush collapse. It was found that counterion can form ordered brush structure and has a global free

energy minimum, whereas disordered and metastable free energy minimum is observed in poor solvent condition. This ordered and global free energy minimum can be a result of multivalent counterion mediated bridging. Work presented in this chapter does not probe the effect of the poor solvent in brush height reduction; however, it will be a very interesting study to compare the mechanism and the energetics of the multivalent-counterion-mediated versus poor-solvent-mediated densely grafted and short (stiff) PE brushes resolved in an all-atom MD simulation framework.

3.3 Methods

We simulated 36 fully charged Polyacrylic acid (PAA) chains grafted in a 6*6 (x*y) array. Different counterions, namely Li^+, Na^+, Cs^+, Mg^{2+}, Ca^{2+}, Ba^{2+}, Y^{3+}, La^{3+} were separately considered (as screening counterions) to neutralize the polyelectrolyte (PE) segmental charge in a solvent of explicitly modeled SPC/E water [67]. Continuous Lennard Jones (LJ) and reflective walls were placed at the bottom and the top of the simulation box respectively to prevent mobile ions and water molecules from leaving the simulation system. The particle trajectories were calculated using the Velocity-Verlet algorithm, maintaining a time step of 2 fs. Non-bonded interactions were modelled as the sum of a shifted-truncated 12-6 Lennard Jones potential (U_{LJ}) where the cut-off was 13Å. To calculate the long-range Columbic interactions, PPPM (particle-particle particle-mesh) algorithm [68] was used. The bonds and angles of water molecules were conserved with the help of the SHAKE algorithm [69]. Periodic boundary conditions were applied in x and y directions, while the fixed boundary condition was incorporated in z direction. Simulation system height was more than $N\sigma$ (σ=3.5 Å is the LJ distance parameter of backbone carbon atoms of the PE chains) in all simulations. Simulations were performed in LAMMPS [70]. OVITO was used to visualize the simulation system [71].

After creating the initial configuration, the system was first run in the NP_zT ensemble (the subscript Z means that only the system height was allowed to change) to obtain the correct simulation box height at 300 K and 1 atm, by applying the Nosé-Hoover thermostat and barostat [79,80]. Subsequently, the system was equilibrated in the NVT ensemble to obtain the correct equilibrium configuration of the system by applying the Langevin thermostat [79]. We performed each simulation until the brush height starts fluctuating around a constant value. After equilibration, we performed the production run for 12ns. For visualizing this brush height in equilibration and production, we plotted the time evolution of end-to-end brush height after NP_zT for the case of Ba^{2+} as an example (please see Fig. 3.6). We also checked the autocorrelation function of the end point of PE chains in the production period: the autocorrelation function started fluctuating around zero very quickly which indicates proper statistical sampling in total 12ns production run.

We have calculated the end-to-end brush height using the following equation:

$$H = \langle Z_i \rangle - Z_b. \qquad (3.2)$$

Here H is the end point brush height, Z_i is the position of the free end backbone carbon of the i^{th} chain, Z_b is the fixed position of the grafted backbone carbon. Bracket indicates that this is averaged over the full production period.

We have used OPLS-AA force field [72] to model the interaction parameters for the PAA chains. The bonded and non-bonded parameters for the PAA chains were taken from the OPLS database. The Lennard Jones (LJ) parameters for the monovalent counterions were taken from the work of Joung and Cheathan [73]. Parameters for multivalent counterions were employed from Li *et al.* [113,114]. These parameters are very accurate for monovalent and multivalent ions in an aqueous system. These parameters have been calibrated with hydration free energy of the ions and

they match accurately with quantum calculations for respective van der Waals distance. Of course, for ions with increased charges this accuracy decreases slightly. For example, with increased charges slight inaccuracy sets in the ion−oxygen distance (IOD) prediction because of the polarizability of highly charged ion. The highest error estimated is 8.9% for Y^{3+}. These errors are tabulated in Ref. [73,113,114]. In the context of using all-atom model for multivalent counterions with PE, there are also recent studies that have successfully employed OPLS-AA and homemade nonpolarizable force field for probing the effect of multivalent ions in ionic liquid system [115,116]. We have checked the effect of polarizability of Y^{3+} on overall brush height, bridging interaction, and counterion condensation condensation to the PE chain by incorporating 12-6-4 lj parameters [114]. These results are given in Appendix B. We see a very little variation in brush height and bridging interactions. We also find that all of the Y^{3+} is condensed to the PE chain, although the condensation distance is slightly increased. So, we can say that our consideration of non-polarizable force-field has little effect on the results resented in this chapter.

To visualize equilibration, we have plotted the end-to-end brush height at different time for the case of Ba^{2+} screening counterion (with added salt) as an example [see Fig. 3.6(a)]. We have checked this equilibration for all the simulations. The red region in the plot in Fig. 3.6(a) indicates the production period, i.e., the time period that is utilized to generate the results. In this production period, the brush height fluctuates around a constant value, confirming the attainment of equilibrium. This production period is considered to be 12 ns for the simulations for all cases of counterions both in absence and presence of the added salt (see Table 3.1). We also checked the autocorrelation function of the end point of PE chains in this production run. The autocorrelation function for a variable Y is given by $C_Y(t) = \frac{(<Y(t)-\langle Y\rangle)(Y(0)-\langle Y\rangle>)}{<Y^2>-<Y>^2}$, where ⟨Y⟩ denotes the mean value of Y. We plot the autocorrelation function for average end-point brush height

$C_e(t)$ corresponding to the cases of different screening counterions for the case of with and without the added salt (i.e., 0.4 M concentration of the chloride salt of the corresponding counterions) in Figure 3.6 (b, c). It can be observed that the autocorrelation functions for all the cases start fluctuating around zero very quickly, which indicates proper statistical sampling in total 12ns

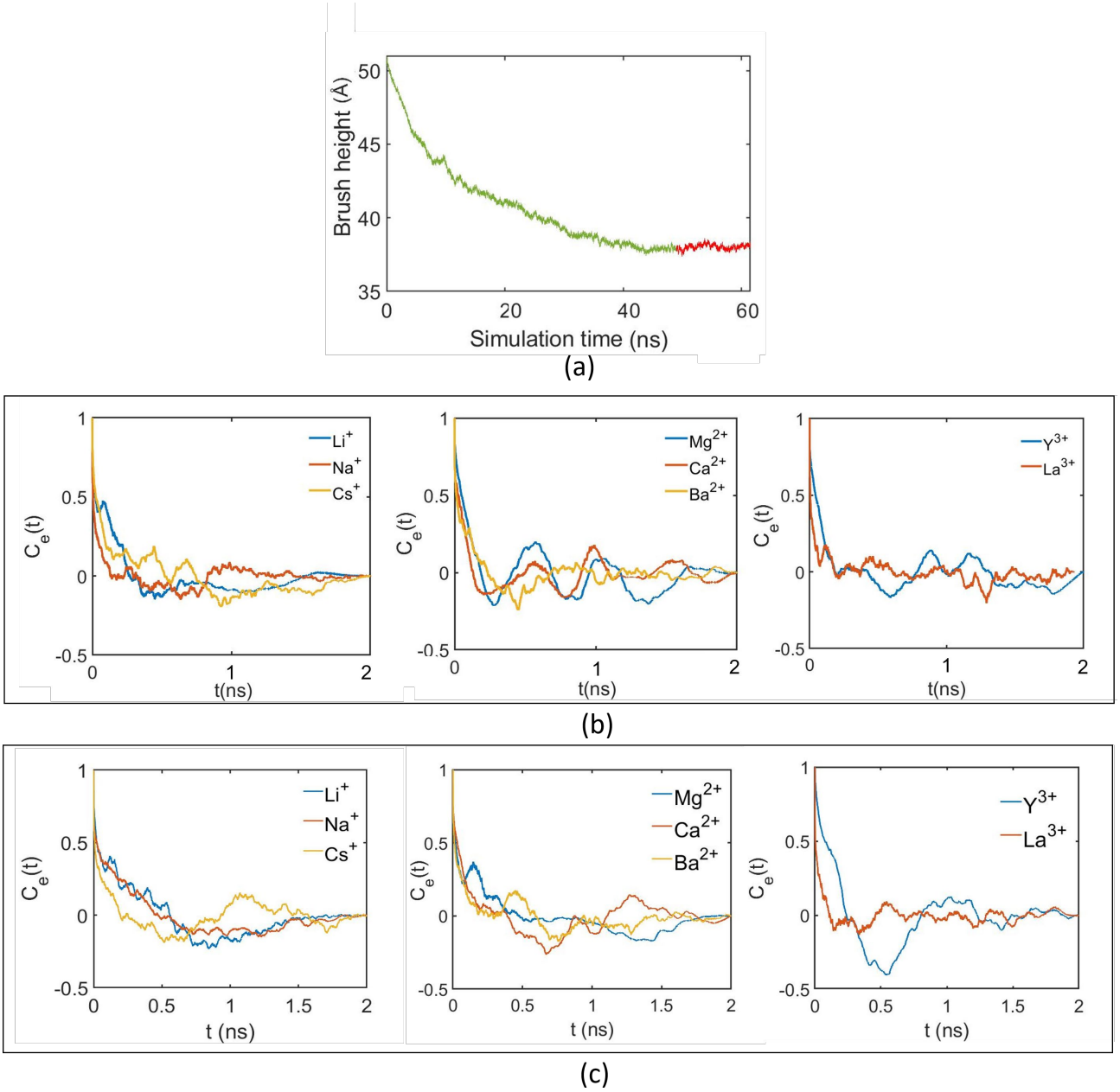

Figure 3.6: Simulation equilibration check**.** (a) Time variation of the End-to-end brush height for the case of Ba^{2+} screening counterion in presence of the added salt. In this plot, the green part indicates equilibration period, while the red part production period. Autocorrelation function of the end point of PE chains for the cases of different screening counterions for the case of (b) without salt and (c) with salt (0.4 M concentration of chloride salt of the corresponding counterions).

production run. Also, we shall like to point here that we have averaged our result for the entire production period (i.e., 12 ns).

In table 3.1 have provided total simulation time breakdown for all simulations:

Simulation type	Equilibration time	Production time	Total simulation time
Li^+ (without salt)	28 ns	12 ns	40 ns
Na^+ (without salt)	30 ns	12 ns	42 ns
Cs^+ (without salt)	22 ns	12 ns	34 ns
Mg^{2+} (without salt)	29 ns	12 ns	41 ns
Ca^{2+} (without salt)	31 ns	12 ns	43 ns
Ba^{2+} (without salt)	36 ns	12 ns	48 ns
Y^{3+} (without salt)	43 ns	12 ns	55 ns
La^{3+} (without salt)	29 ns	12 ns	41 ns
Li^+ (with salt)	50 ns	12 ns	62 ns
Na^+ (with salt)	36 ns	12 ns	48 ns
Cs^+ (with salt)	48 ns	12 ns	60 ns
Mg^{2+} (with salt)	40 ns	12 ns	52 ns
Ca^{2+} (with salt)	50 ns	12 ns	62 ns
Ba^{2+} (with salt)	50 ns	12 ns	62 ns
Y^{3+} (with salt)	52 ns	12 ns	64 ns
La^{3+} (with salt)	40 ns	12 ns	52 ns

Table 3.1: Simulation time scale for the simulations corresponding to different counterions without and with the added salt (0.4 M concentration of chloride of the corresponding counterions)

The Lennard-Jones (LJ) potential (U_{LJ}) used in the simulations is expressed as:

$$U_{LJ} = 4\epsilon_{ij}\left[\left(\frac{\sigma_{ij}}{r_{ij}}\right)^{12} - \left(\frac{\sigma_{ij}}{r_{ij}}\right)^{6}\right], \quad (3.3)$$

while the Coulombic pairwise interaction (U_{Coul}) used in the simulation is expressed as:

$$U_{Coul} = \frac{q_i q_j}{4\pi\epsilon_0\epsilon_1 r_{ij}}. \quad (3.4)$$

In these equations, ϵ_{ij} is the depth of the LJ potential well between atoms i and j, σ_{ij} is the distance between atoms i and j, q_i and q_j are charges of the i^{th} and j^{th} atoms, r_{ij} is the distance between atoms i and j, ϵ_0 is the permittivity of vacuum and ϵ_1 the relative permittivity of the background (taken to be 1). Geometric mixing rules were used for calculating the LJ interactions between the different atom types. For mobile-ion-mobile-ion and mobile-ion-water interactions, we used the Lorentz-Berthelot mixing rules to be consistent with Joung et al. [73] and Li et al. [113,114].

In Fig. 3.5, we have provided a schematic representation of the fully ionized Polyacrylic acid molecule. Parameters required for eqs. 3.3 and 3.4 for atom mentioned in figure 3.7 is shown in Table 3.2.

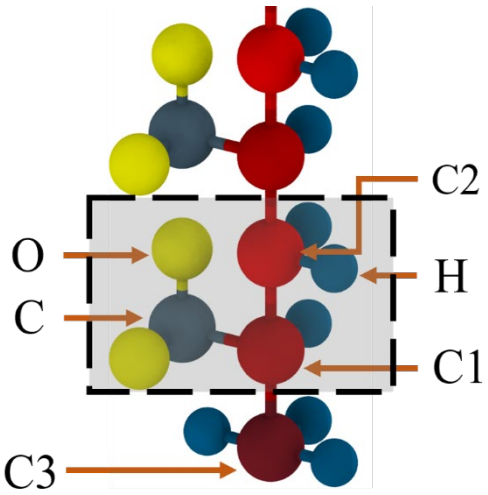

Figure 3.5. A partial schematic representation of the fully ionized PAA molecule. Different atom types are indicated with arrows. Polyelectrolyte's (PE's) repeating unit is indicated with the shaded box.

Atom Type	**Charge (e)**	**Mass (amu)**	**ϵ (Kcal/mole)**	**σ (Å)**
C3 (CH_3)	-0.18	12.011	0.066	3.50
C2 (CH_2)	-0.12	12.011	0.066	3.50
C1 (CH, Attached to COO-)	-0.16	12.011	0.066	3.50
C (COO-)	0.70	12.011	0.105	3.75
H	0.06	1.008	0.03	2.50
O (COO-)	-0.80	15.999	0.210	2.96
O_w (H_2O)	-0.8476	15.999	0.155354	3.166
H_w (H_2O)	0.4238	1.008	0	0
Li	1.00	6.941	0.3367344	1.4094
Na	1.00	22.99	0.3526418	2.1595
Cs	1.00	132.9	0.0898565	3.6010
Mg	2.00	24.305	0.00417787	2.294955
Ca	2.00	40.078	0.04560206	2.7083
Ba	2.00	137.327	0.23380842	3.2518
Y	3.00	88.906	0.02759	2.5996
La	3.00	138.91	0.09454	2.903
Cl	-1.00	35.453	0.012785	4.83
Continuous LJ Wall (Parameters remain unchanged for interaction with all atom types)	0.00	15.00794	0.1947	3.00 (LJ cut off length is 3.36 Å)

Table 3.2: Charge, mass and LJ parameters for all the different atom types

Harmonic bond style is used to calculate the potential energy for bond:

$$U_{bond} = K_b(r - r_0)^2. \qquad (3.5)$$

Here, r_0 is the equilibrium bond length and K_b is bond stiffness. The values for r_0 and K_b for all

bond types are provided in Table 3.3.

Bond Type	$\boldsymbol{K_b}, (\frac{\boldsymbol{Kcal}}{\boldsymbol{mol}.\text{Å}^2})$	$\boldsymbol{r_0}, (\text{Å})$
C2-H	340.0	1.09
C2-C1	268.0	1.529
C1-H	340.0	1.09
C3-H	340.0	1.09
C-C1	317.0	1.522
C1-C3	268.0	1.529
C-O	656.0	1.25
O_w-H_w	-	1.00

Table 3.3: Bond parameters used in the simulations

The potential energy for the finite angle between different bonds is calculated using the following harmonic equation:

$$U_{angle} = K_a(\theta - \theta_0)^2. \qquad (3.6)$$

Here, θ_0 is the equilibrium value of the angle and K_a is the angle stiffness. The values for θ_0 and K_a for different angles are provided in Table 3.4.

Angle Type	$\boldsymbol{K_a}, (\frac{\boldsymbol{Kcal}}{\boldsymbol{mol}.\boldsymbol{rad}^2})$	$\boldsymbol{\theta_0(deg)}$
H-C2-H	33.00	107.8
H-C2-C1	37.5	110.7
C2-C1-H	37.5	110.7
C1-C3-H	37.5	110.7
H-C3-H	33.00	107.8
H-C1-C	35.0	109.5
O-C-O	80.0	126.00
C2-C1-C	63.0	111.1
C3-C1-C	63.0	111.1

H_w-O_w-H_w	-	109.47
C2-C1-C2	58.35	112.7
C2-C1-C3	58.35	112.7
C1-C-O	70.0	117.0
C3-C1-H	37.5	110.7
C1-C2-C1	58.35	112.7

Table 3.4: Angle parameters used in the simulations

The potential energy associated with the 4-atom dihedral torsion interactions is given by

$$U_{dihedral} = \frac{1}{2}K_1[1 + \cos(\emptyset)] + \frac{1}{2}K_2[1 - \cos(2\emptyset)] + \frac{1}{2}K_3[1 + \cos(3\emptyset)] + \frac{1}{2}K_4[1 - \cos(4\emptyset)]. \quad (3.7)$$

Here, K_1, K_2, K_3, and K_4 are the four Fourier coefficients for torsional interactions, and $\emptyset$ is the torsional angle. Values of K_1, K_2, K_3, and K_4 are provided in Table 3.5.

Dihedral type	$\boldsymbol{K_1}$, $(\boldsymbol{Kcal/mole})$	$\boldsymbol{K_2}$, $(\boldsymbol{Kcal/mole})$	$\boldsymbol{K_3}$, $(\boldsymbol{Kcal/mole})$	$\boldsymbol{K_4}$, $(\boldsymbol{Kcal/mole})$
H-C2-C1-H	0.0	0.0	0.30	0.0
H-C2-C1-C	0.0	0.0	-0.10	0.0
H-C2-C1-C2	0.0	0.0	0.30	0.0
H-C2-C1-C3	0.0	0.0	0.30	0.0
H-C1-C-O	0.0	0.0	0.00	0.0
H-C1-C3-H	0.0	0.0	0.30	0.0
C2-C1-C-O	0.0	0.82	0.00	0.0
C2-C1-C2-C1	1.30	-0.05	0.20	0.0
H-C3-C1-C2	0.0	0.0	0.30	0.0
C3-C1-C-O	0.0	0.82	0. 0	0.0

C1-C2-C1-C	-3.185	-0.825	0.493	0.0
C1-C2-C1-C3	1.30	-0.05	0.20	0.0
H-C1-C2-C1	0.0	0.0	0.30	0.0
H-C3-C1-C	0.0	0.0	-0.10	0.0

Table 3.5: Dihedral parameters used in the simulations

The potential energy associated with the improper torsional dihedrals are modelled using the harmonic function:

$$U_{improper} = K_i(\varphi - \varphi_0)^2. \quad (3.8)$$

Here, φ_0 represents the equilibrium value of the improper torsional angle and K_i is the improper torsional stiffness. Their values for the C1-O-C-O system is provided in Table 3.6.

Improper Type	$\boldsymbol{K_i}\ (\frac{\boldsymbol{Kcal}}{\boldsymbol{mol.rad^2}})$	$\boldsymbol{\varphi_0(deg)}$
C1-O-C-O	10.5	180

Table 3.6: Improper dihedral parameters used in the simulations

3.4 Conclusion

In this chapter, we have employed all-atom MD simulations to quantify the counterion-dependent bridging interactions in PE brushes for the first time: our results confirm that incomplete condensation and lower solvation number (for smaller counterions) lead to reduced bridging interactions. Non-condensed counterions help to neutralize the PE monomers in its second solvation shell, which hinders the bridging interaction. On the other hand, lower solvation numbers imply lesser space to accommodate different $O_{Carboxylate}$ in the first solvation shell of a counterion, which also hinders bridging interactions. These more involved factors, rather than the previously hypothesized counterion valence, dictate bridging. Accordingly, we witness bridging interactions even for cases of monovalent counterions, which in turn leads to more augmented brush height reduction for certain monovalent counterions as compared to some cases of multivalent counterions. This observation is in contradiction to the experimental findings where the multivalent counterions invariably led to a larger decrease in the height of the PE brushes. We explain this discrepancy by noting that in our simulations we only consider densely grafted and short (less flexible) PE brushes that ensure that the reduction in brush height does not occur through the formation of different laterally inhomogeneous structures like pinned micelles and cylindrical bundles; on the contrary, in experiments, which invariably consider longer and less densely grafted brushes, these inhomogeneous structures are formed and dictate the brush height reduction (and hence causes a significantly high degree of brush height collapse) in presence of multivalent counterions. Finally, we argue that this study will be a good indicator of what might happen qualitatively in other PE brush systems. For example, for Polystyrene Sulfonate (PSS) PE brushes, sulfonate acts as the negatively charged group and the partial charge for $O_{sulfonate}$ is different from that of $O_{Carboxylate}$. Accordingly, the condensation of counterions on the PE chain will change

altering the counterion-dependent bridging interactions quantitatively, although the qualitative effect of the counterion size and valence (and the corresponding charge density) in affecting the bridging interactions should be similar to that proposed in our results.

Chapter 4: Overscreening, Coion-Dominated Electroosmosis, and Electric Field Strength Mediated Flow Reversal in Polyelectrolyte Brush Functionalized Nanochannels[***]

Abstract: *Controlling the direction and strength of nanofluidic electrohydrodyanmic transport in presence of an externally applied electric field is extremely important in a number of nanotechnological applications. Here, we employ all-atom molecular dynamics (MD) simulations to discover the possibility of changing the direction of electroosmotic (EOS) liquid flows by merely changing the electric field strength in a nanochannel functionalized with polyelectrolyte (PE) brushes. In exploring this, we have uncovered three facets of nanoconfined PE brush behavior and resulting electroosmotic (EOS) transport. First, we identify the onset of an overscreening effect: such overscreening refers to the presence of more counterions (Na^+) within the brush layer than needed to neutralize the negative brush charges. Accordingly, as a consequence of the overscreening, in the bulk liquid outside the brush layer, there is a greater number of coions (Cl^-) than counterions in the presence of an added salt (NaCl). Second, this specific ion distribution ensures that the overall EOS flow is along the direction of motion of the coions. Such coion-dictated EOS transport directly contradicts the notion that EOS flow is always dictated by the motion of the counterions. Finally, for large-enough electric fields, the brush height reduces significantly enforcing some of the excess overscreening-inducing counterions to squeeze out of the PE brush layer into the brush-free bulk. As a result, the overscreening effect disappears and the number of coions and counterions outside the PE brush layer becomes similar. Despite that there is an EOS transport: this EOS transport, unlike the standard EOS transport that occurs due*

[***] Contents of this chapter is published in *ACS Nano* as: Pial, T. H.; Sachar, H. S.; Desai, P.R.; S. Das, Overscreening, Co-Ion-Dominated Electroosmosis, and Electric Field Strength Mediated Flow Reversal in Polyelectrolyte Brush Functionalized Nanochannels, *ACS Nano* **2021** 15, 6507.

to the imbalance of the coions and counterions, occurs since a larger residence time of the water molecules in the first solvation shell of the counterions (Na^+) ensures a water transport in the direction of motion of the counterions. The net effect is the reversal of the direction of the EOS transport by merely changing the strength of the electric field.

4.1 Introduction

In nanofluidic transport of liquids, ions, and (bio)particles, application of electrokinetics span a large range of disciplines from geoscience [117], energy engineering [118, 119], sensing and separation [120, 121], gating of ions and liquids [122,123] to advancing biomimetic and bioinspired engineering [124, 125]. Electroosmotic (EOS) flow, a type of electrokinetic transport, can be generated in a micro-nanochannel by applying an external electric field to drive the ion-containing (electrolyte) liquids. In some practical scenarios, the direction of EOS flow inside the nanochannel (positive or negative, relative to the applied electric field) needs to be manipulated in a way that enhances mixing, reaction, separation, and printing [37-41]. Previous research has shown that one needs to modify the system's overall environment to get a modified flow behavior. For example, changing the sign of the zeta potential or the surface charge density of the channel wall [126, 127], or controlling the buffer pH value [128] may help to control the EOS flow direction in some simplified systems. Reversed and patterned flows inside a nanochannel can also be induced by suitable surface modifications [129, 130]. These experimental studies have been supplemented by atomistic simulation studies on modulating nanochannel EOS flows by changing the surface charge density or hydrophobicity of the channel wall [131, 132]. All of these modifications eventually change the mobile ion distribution in the nanochannel, which in turn leads to different flow directions inside the nanochannel. Therefore, in order to control the direction of the EOS transport in a nanochannel by merely changing the strength of the driving electric field, one needs to trigger a situation where the ion distribution (or more generally, the mechanism that drives the EOS transport) gets altered by the variation in the strength of the electric field. To the best of our knowledge, such a scenario has rarely been accomplished.

Surfaces grafted with polyelectrolyte (PE) brushes [83] are well-known for their

responsiveness to different environmental stimuli and have been used in a myriad of applications like ion and bioanalayte sensing [14, 133], fabrication of ionic diodes [48, 134], nanofluidic current rectification [84, 85], oil recovery [18], targeted nanoparticle-based delivery [16, 17] etc. Such grafting with PE brushes has also enabled functionalizing nanochannels for applications in sensing and current rectification. The applied axial electric field will invariably cause an EOS transport in such brush-grafted, electrolyte-solution filled nanochannels given the fact that the charged brushes develop their own mobile ion distribution around them neutralizing their charges and this ion distribution respond to the applied electric field. In fact, the response of the PE brushes to the applied electric field and the resulting changes in the morphology of the brushes and the associated ion distribution makes it possible to significantly influence the EOS transport in brush-grafted nanochannels. Despite its tremendous potential, EOS flow in PE-brush-grafted nanochannels has not been well studied in an atomistically-resolved scale. Along with a few simplified continuum studies [42, 43] there are only a handful of MD simulation studies available for liquid transport in brush-grafted nanochannels [44-46, 135]. However, none of these studies have considered an all-atom description of the brushes and solvent molecules, which can be important in obtaining the appropriate brush, water and ion behavior in PE brush grafted system, and therefore providing an atomisticially-resolved description of such EOS transport in brush-functionalized nanochannels [108].

In this chapter, we have studied the EOS transport in nanochannels functionalized with PE brushes in an all-atom MD setup that couples the PE brush system with an external electric field. We first discover that for zero to intermediate electric field strengths the large confinement enforces an overscreening effect, which implies the presence of greater number of counterions within the PE brush layer than that required to screen the PE charges. Second, as a result of such

overscreening, the number of coions (from the added salt) is larger than the number of counterions within the brush-free bulk. As a result, in conjunction with the fact that the flow within the brushes is severely retarded, the EOS flow for small and medium strength electric fields is in the same direction as the motion of the coions. Such coion-dictated EOS transport is a most intriguing of finding, given the fact that the EOS transport is always believed to occur in the direction of the counterions. Finally, for larger electric fields, the brush height is significantly reduced enforcing a reduction in the overscreening effect and creating parity in the number of coions and counterions within the brush-free bulk. Therefore, the EOS transport does not occur to the imbalance of the counterions and coions. On the contrary, we establish that the residence time of the water molecules is larger within the first hydration shell of the considered counterions (Na^+) than the coions (Cl^-): we hypothesize that the EOS transport is triggered by this difference of the residence time and accordingly, occurs in the direction of the motion of the counterions. These circumstances enable us to obtain the situation where there is an electric field strength mediated reversal in the direction of the EOS transport in nanochannels functionalized with PE brushes.

4.2 Results and Discussions

In our system [shown in Fig. 4.1(A)], fully ionized Polyacrylic acid (PAA) chains (H[-CH_2-$CH(COO^-)$-]nCH_3) are used as the polyelectrolytes and explicitly modeled water molecules act as the solvent. Sodium counterions (Na^+ ions) are added to neutralize the PE segmental charge. In addition, 0.1 M NaCl salt is added to the system. All other details associated with the simulation are provided in method section. For driving the flow in the PAA-brush-grafted nanochannel, we applied electric field whose strengths ranged from 0.1 to 1 V/nm in axial (or x) direction. While such large electric fields are not routinely employed in experiments [136-138], it is possible to generate electric fields in the range of 1-5 V/nm for certain applications [139]. In fact, several

experimentally probed biological problems involving proteins and DNA have considered electric fields in the order of 0.1-1 V/nm. For example, there have been studies probing the behavior of protein cytochrome c immobilized on silver electrodes in the presence of electric fields that were calculated to be in the range of 1-2.5 V/nm [65]. Similarly, Heng *et al*. probed the electromechanics of a DNA molecule in a synthetic nanopore in the presence of an electric field of 0.31 V/nm [66]. Furthermore, such large electric fields are needed for the typical MD simulation studies [44-46] for suppressing the thermal noise in order to increase the signal-to-noise ratio. It is also interesting to note here that the threshold value of the electric field strength that triggers the initiation of the water ionization has been reported to be around 2.5 V/nm and the ionization becomes more frequent around an applied electric field of 3.5 V/nm [62, 63], which is several times higher than the electric field strength (0.1-1 V/nm) considered in our simulations. When an electric field $\boldsymbol{E}$ is applied to the system, a force of $q_i\boldsymbol{E}$ acts on the atom i having a charge of q_i. In figure 1(B), we depict the electroosmotic (EOS) velocity profiles (*i.e*., the velocity profiles of the water molecules) as a function of the applied electric field. The following key results emerge: (1) for smaller magnitude of electric fields ($|\boldsymbol{E}|$=0.1, 0.5 V/nm), the EOS flow occurs in the direction opposite to the applied electric field (negative *x* direction or the direction in which the coions move, see later), (2) for larger electric field ($|\boldsymbol{E}|$=1 V/nm), the direction of the EOS flow is reversed, *i.e.*, water flows in the same direction as the applied electric field (positive *x* direction or the direction in which the counterions move, see later), and (3) for all the electric fields, the EOS flow occurs primarily outside the brushes, while the flow inside the brushes is very small. These EOS velocity profiles, therefore, confirm a coion-dictated EOS flow for small electric fields (the standard EOS flow is invariably counterion-dictated) and an electric field strength driven reversal in the direction of the EOS flow profile (usually the EOS flow increases in strength, but never reverses, with an increase in electric field strength). In the rest of this chapter, we shall try to identify the fundamental factors

responsible for such highly non-intuitive EOS transport in brush-functionalized nanochannels.

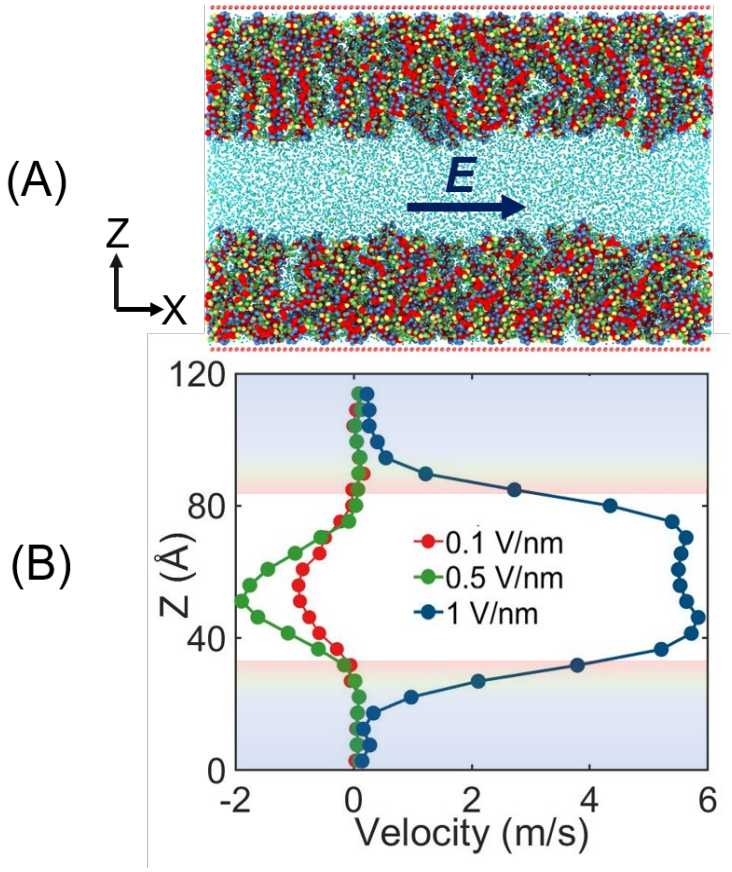

Figure 4.1: (A) A schematic of the PE brush grafted nanochannel system. (B) Velocity of the water (solvent) molecules along the system height for different electric fields.

We first study the distribution of the coions (resulting from the added salt) and counterions (resulting from the added salt and charge neutralizing counterions) inside and outside the brush layer for different electric field strengths. We clearly find that for no or small electric fields, there is an overscreening effect within the brushes, quantified by the presence of a larger number of counterions than needed to screen the PE charges [see Fig. 4.2(A) and Table 4.1]. This excess counterions come from the added salt: accordingly, the number of coions will be greater than the number of counterions in the brush-free bulk [see Fig. 4.2(A) and Table 4.1]. This is also evident from the spatial distribution of the coions and counterions for $|\boldsymbol{E}|$ = 0.1 V/nm [see Fig. 4.2(B)].

The significantly larger concentration of the Cl^- ions (coions) in the bulk ensures that net direction of the motion of the solvent will be in the direction of the motion of the coions, leading to the case of coion-dominated EOS transport for lower applied electric field. For a larger electric field, *i.e.*, $|\boldsymbol{E}|$ =1 V/nm on the other hand, we find a significant reduction in the overscreening effect within the PE brush layer, leading to an almost equal number of coions and counterions within the brush-free bulk [see Figs. 4.2(A, C) and Table 4.1].

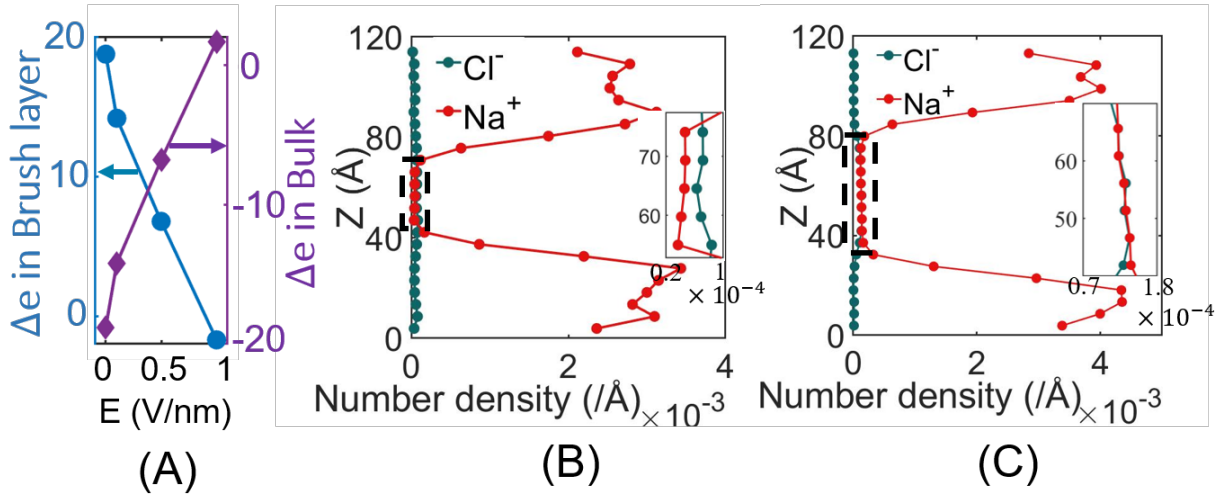

Figure 4.2: Overscreening in nanochannel. (A) Excess of the positive charges $\Delta e = (e^+ - e^-)$ inside brush and in brush-free bulk as a function of the electric field. e^+ and e^- indicate total number of positive charges (Na^+) and negative charges (Cl^- and PE charges) respectively. Number density of ions in the system for electric field strength of (B) 0.1 V/nm, and (C) 1 V/nm. In the insets of (B) and (C), the number density of ions (having the same unit as the main figure) near the bulk region have been zoomed. Please see Fig. C.4 (A) for the ion number distribution for $|E|$=0.5 V/nm.

In order to understand such non-intuitive electric field mediated disappearance of the overscreening effect, which will also affect the direction of the EOS transport, we study the response of the PE brushes to the electric field. We find that there is an overall reduction in the vertical end-to-end brush height with an increase in the electric field strength [see Fig. 4.3(A)]. Previously, Netz showed the unfolding of a PE globule to a rod-like chain under applied electric fields [28, 140]: this knowledge will help us to explain brush height reduction with electric field.

In these studies [28, 140], without an electric field, the PE is neutralized by counterions to form a PE-counterion globule. Applied electric filed tends to orient the counterion distribution around the PE and a net dipole-moment is induced in the PE-counterion complex in the direction of the electric field. This finite dipole moment (which also indicates a polarization) tends to orient a coil or unfold a globule to a rod-like chain that aligns in the direction of the electric field [28, 140]. In this study, COO^- are the functional groups of the PAA PE molecule, which are neutralized by the counterions. We first obtain the probability of finding a counterion around the oxygen atoms of the COO^- groups [see Fig. 4.3(B) and appendix C]. For the case of $|\boldsymbol{E}|$=1 V/nm, the counterions prefer to localize on the positive side (X > 0; note that $\boldsymbol{E}$ is directed from X < 0 to X > 0) of these oxygen atoms. However, no such direction-dependent preference is observed for the case where no electric field is applied. This electric field mediated orientation of O^--Na^+ ion-pair indicates that we enforce a directional dependence of the charge distribution, which is similar to the induced dipole moment identified previously [28, 140,141]. Therefore, we can infer that this aligned ion-pair will try to align the brush in the applied electric field direction. To verify this, we study the probability distribution of monomer in *x* and *y* directions: for that purpose, we consider the position of grafted carbon atom as center (0,0) and count the number of backbone carbon atoms in *x* and *y* directions around (0,0). We can see that in the *x* direction, monomers become sparser which means they become aligned in *x* direction [see Fig. 4.3(C, top)], while no such change is observed in the probability of finding monomer in the *y* direction [see Fig.4. 3(C, bottom)]. Therefore, we can infer that due to the electric field driven alignment of the ion pairs in *x* direction, polymers tend to be aligned in the *x* direction, which eventually reduces the brush height in *z* direction and increases

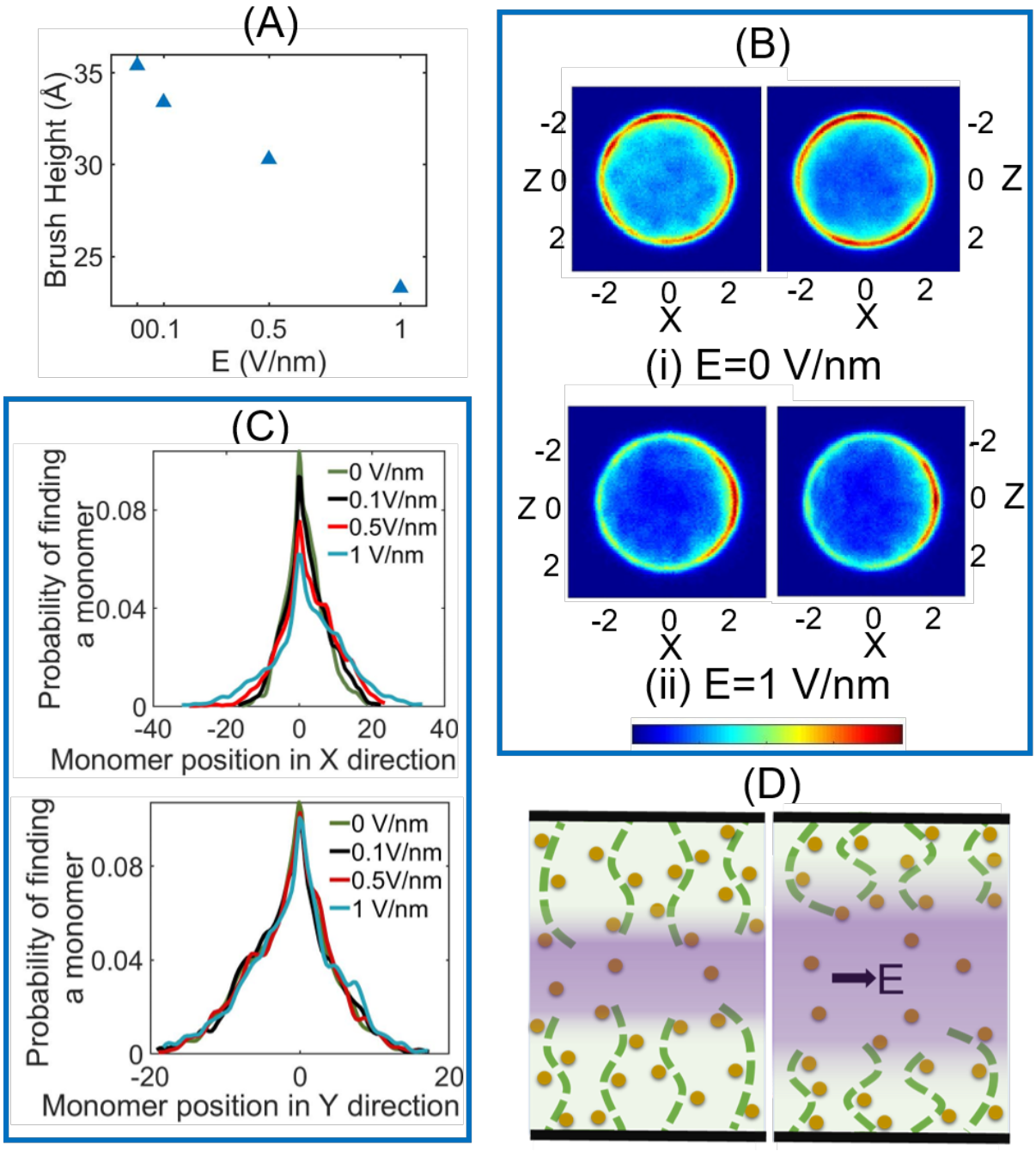

Figure 4.3: Brush height reduction. (A) End to end brush height as a function of applied electric field. (B) Na^+ ion distribution contour around an O^- of COO^- for $|E| = 0$ and $|E| = 1$ V/nm. Colorbar indicates concentration from low to high (blue to red). (C) Probability distribution of finding a backbone carbon in x and y direction under different electric field strength. (D) An illustration showing the electric field induced reduction in brush height also causing an increase in the volume of the brush-free region (shown in purple). In (D), dashed lines and circles represent PE chains and counterions, respectively.

the effective volume of the brush-free region [shown schematically in Fig. 4.3(D)]. As a consequence, there is a lesser available volume for the ions within the brush layer, enforcing a squeezing-out (or exclusion) of primarily most of the overscreening causing counterions (and a few coions, especially for very large $|\boldsymbol{E}|$, see Table 4.1) from within the brush-layer to the bulk: this explains the reduction in overscreening (or attaining a parity in the number of coions and counterions within the brush-free bulk) with an increase in the strength of $|\boldsymbol{E}|$.

In addition to the difference in the ion concentration distributions, the electric field dependent velocities of the Na^+ and Cl^- ions are also important for quantifying the electric field dependent EOS flow profiles. Fig. 4.4(A) and appendix C establish that the velocity of the Cl^- ions is larger than the velocity of Na^+ ions at low electric field strengths ($|\boldsymbol{E}|$=0.1, 0.5 V/nm), while at larger electric field ($|\boldsymbol{E}|$=1 V/nm) the velocity of the two ions are similar [see Fig. 4.4(B)]. Previous studies have shown that at low electric field strength, the mobility of Cl^- ions is higher than the mobility of the Na^+ ions [142] and this difference in the mobility reduces on increasing the electric field strength. This justifies the significantly larger velocities of the Cl^- ion for $|\boldsymbol{E}|$=0.1, 0.5 V/nm and similar velocities of the Cl^- and Na^+ ions for $|\boldsymbol{E}|$=1 V/nm. Results from experiments [143] are also consistent with our MD simulation predictions for smaller $|\boldsymbol{E}|$ values. This higher velocity coupled with a larger concentration of Cl^- for smaller $|\boldsymbol{E}|$ also drives the EOS flow along the direction of the coion at low electric field strengths.

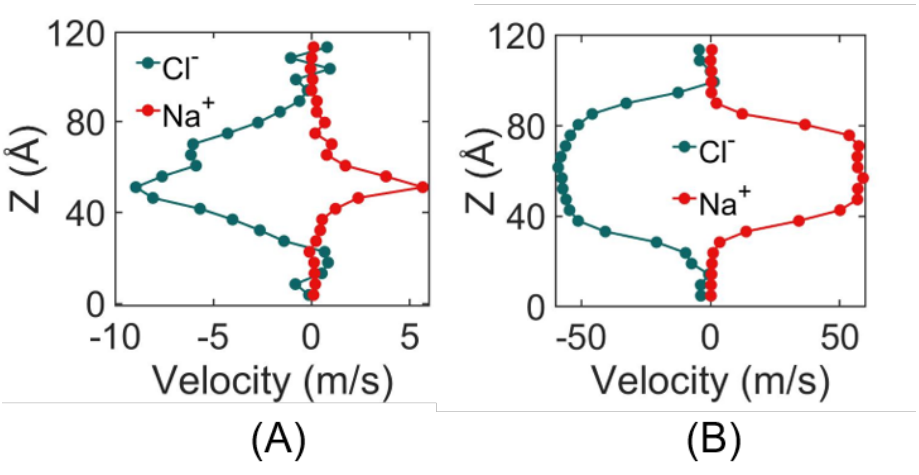

Figure 4.4: Velocity profiles of ions for (A) $|E|$ = 0.1 V/nm and (B) $|E|$ = 1 V/nm.

We finally quantify the strength of the dynamic interaction of the water molecules with the ions: such quantification is essential to pinpoint the extent to which the overall flux of the ions (which is a combination of its concentration and the mobility/velocity) dictates the EOS velocity of the water. This dynamic interaction is quantified by calculating the average residence time of a water molecule (oxygen atom) within the first solvation shell of ion [which closely resembles interaction strength (hydration free energy)] [144]. The residence times [R(t)] are calculated from the time correlation function defined as:

$$R(t) = \frac{1}{N_h}\sum_{i=1}^{N_h} \theta_i(t_0)\theta_i(t_0 + t). \qquad (4.1)$$

Here θ_i is the Heaviside unit step function (if one water molecule i resides inside the first solvation shell of an ion, θ_i =1; otherwise, θ_i =0), N_h is the number of water molecules in the first solvation shell (the radial distribution functions needed for calculating solvation shell size have been provided in the appendix C), and t_0 is the initial time step. This residence time is averaged for all ions in the bulk and over 50 different initial time steps. Fig. 4.5 shows that for both small and large electric fields, the residence time of water in the first hydration shell of the Na^+ ion is much larger than that of the Cl^- ion, which implies that the water molecules reside for much longer within the Na^+ solvation shell allowing the Na^+ ions to drag the water molecules with them for much longer. On the other hand, for Cl^- ion, where this timescale is smaller, water can diffuse out of the solvation shell of the Cl^- ion much faster, and can be dragged for lesser time. Therefore, for large field strengths where both the bulk concentration as well as the velocities are very similar for the Na^+ and Cl^- ions, this significantly larger residence time for the Na^+ ion ensures that the water molecules will preferentially move in the direction in which the Na^+ ion moves: accordingly, we find that the EOS flow is counterion-dictated. On the other hand, for smaller electric field strengths, the larger bulk concentration and velocity of the Cl^- ions overwhelm the effect of smaller residence time leading to the water transport and the EOS flow to be coion-dictated. Finally, the very small EOS velocity inside the brushes [as compared to the bulk region, see Fig. 4.1(B)] can be explained by noting that the motion of the counterions inside the brush layer is severely hindered due to the fact that the positive counterions are bound to the negatively charged PE chains by strong

electrostatic forces and the fact that the densely grafted brushes exert a large confinement effect on the brush-supported counterions and water molecules [108]. To explain further, such a large electrostatic attraction between the counterions and the PAA brush molecules ensures that a very large portion of the counterions is condensed on the charged PAA chains, and accordingly, the motion of these condensed counterions is restricted by the motion of the densely grafted PAA chains. Such condensation of ions on charged polymer chains is also known to dictate the mobility of ions in polyelectrolyte gels [145]. Also, as elucidated in our previous study, for densely grafted PAA brushes a large confinement effect is triggered due to a strong steric hindrance effect: as a result, there is a large reduction in the freedom of movement of the ions and water reducing their mobilities within the brush layer [108].

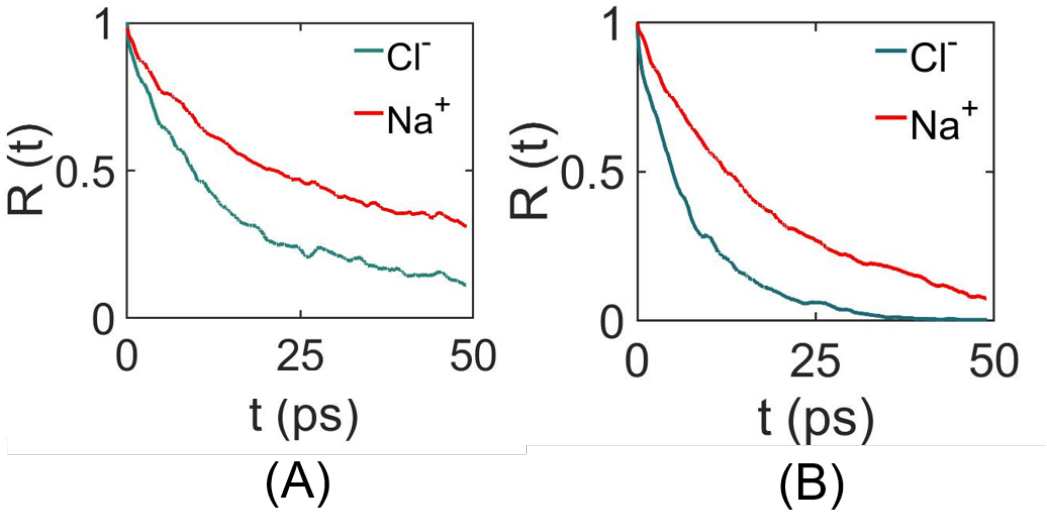

Figure 4.5: Residence time correlation function for both ions for (A) |E| = 0.1 V/nm and (B) |E| = 1 V/nm**.**

Generality and reasoning of overscreening

From the previous subsection, it is clear that the overscreening is the main phenomenon that drives the coion-dominated flow and subsequent electric field strength mediated flow reversal. Before probing the detailed mechanism dictating the occurrence of overscreening, it is useful to

probe the generality of the overscreening phenomenon. To check this generality, we have performed a few more simulations with PE brush grafting density, salt concentration, and PE brushes that are different as compared to those studied and discussed in the previous section. The main flow simulations discussed so far is performed in a nanochannel grafted with PAA PE brushes with a grafting density of $0.05/\sigma^2$ (with Na^+ screening counterions) in presence of 0.1 M NaCl added salt. We have considered three more systems by varying the grafting density (grafting density of $0.03/\sigma^2$), concentration of the added salt (0.2 M of added NaCl salt), and the nature of the PE brushes [nanochannels grafted with Poly-methacrylic acid (PMAA) brushes)]. The details of these simulations can be found in method section. For all these three cases, we have observed overscreening (as confirmed by the ion number density distributions provided in Fig. 4.6 and values reported in Table 4.1). The confirmation of overscreening for these three cases as well as the overscreening for the case reported in the previous subsection establish that the overscreening in a PE brush grafted nanochannel is indeed a generic phenomenon that occurs (with the added NaCl salt) for different PE brush grafting densities, salt concentration, and PE brush type.

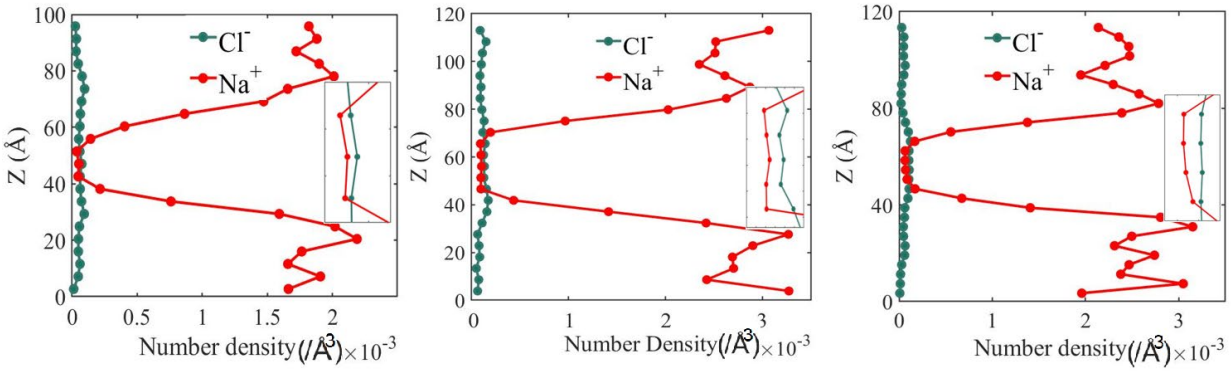

Figure 4.6: Ion distribution profiles for (A) System ***i*** [the nanochannel grafted with PAA PE brushes with a grafting density of $\mathbf{0.03/\sigma^2}$ (with Na^+ screening counterions) in presence of 0.1 M NaCl added salt], (B) System ***ii*** [the nanochannel grafted with PAA brushes with a grafting density of $\mathbf{0.05/\sigma^2}$ (with Na^+ screening counterions) in presence of 0.2 M NaCl added salt], and (C) System iii [the nanochannel grafted with PMAA PE brushes with a grafting density of $\mathbf{0.05/\sigma^2}$ (with Na^+ screening counterions) in presence of 0.1 M NaCl added salt.] In each of the subfigures (A-C), the ion distribution in the bulk is shown in the inset of these subfigures.

To understand the mechanisms responsible for overscreening, we have performed simulations for two more systems. In the first one, PAA brushes are grafted to a single interface (*i.e.*, not a nanochannel) with significantly large bulk volume [see figure 4.7 (A)]. In the second simulation, the nanochannel is grafted with PAA brush layers with Cs^+ ions acting as screening counterions and 0.1 M CsF as the added salt. Details of these two simulations can be found in method section. For the ease of explaining in this section, we are referring the main simulation of the previous section with nanoconfinement and NaCl salt as system N1, the system without nanoconfinement as system N2, and the system with nanoconfinement, Cs^+ as screening counterions, and CsF as the added salt as system N3.

To quantify overscreening, we have calculated the number of positive and negative charges (including the charges of the co-ions and counterions as well as the charges of the PE brushes) for all the main simulation (system N1), the simulation discussed for showing generality of the overscreening (i.e., systems i-iii), simulation without nanoconfinement (system N2) and simulation with CsF salt (system N3). In the following table, these values are provided.

	Main Simulation Syst. N1 (E= 0 V/nm)	Syst. N1 (E= 0.1 V/nm)	Syst. N1 (E= 0.5 V/nm)	Syst. N1 (E= 1 V/nm)	$0.03/\sigma^2$ Grafting density Syst. i	0.2 M Salt Syst. ii	PMAA Brush Syst. iii	No nano-confinement Syst. N2	CsF Salt Syst. N3
Total negative charges from PE brush	4320	4320	4320	4320	2010	2880	2880	2880	864
Positive charges inside brush-layer	4441	4437	4427	4365	2091	3032	2964	2922	862

Negative charges inside brush-layer	4423	4423	4420	4367	2086	3022	2955	2944	865

Table 4.1: Number of charges inside the PE brush-layer for all cases.

Figures 4.7(B) and 4.7(D) illustrate the ion distribution profiles for systems N2 and N3. No overscreening is observed in these two cases, which indicates that the presence of nanoconfinement and the types of coions and counterions play critical roles in determining overscreening. Identification of these roles is critical to pinpoint the onset of overscreening.

We identify that overscreening results from interplay of three phenomena. First is the possible lowering of the osmotic pressure caused by the migration of the salt ions from within the bulk to inside nearby brush layer. The second is the dependence of such migration on the sizes of the salt cations and anions. The third is the stabilization (or the lack of it) of the cations within the PE brush layer induced by their strong (or weak) attraction to the COO^- group of the PE brushes. We discuss the occurrences of these three phenomena to different extents in the three systems that we have studied and from that pinpoint the mechanism of overscreening within the PE brush layer for the system N1.

The osmotic pressure (Π) can be simplistically expressed as $\Pi = Nk_BT/V$, where N is the number of non-interacting species and V is the volume where the species are present. For the case of nanochannel grafted with the PE brushes, the bulk volume (*i.e.*, the volume where the brushes are absent) is significantly small. Accordingly, if all the added salt ions (or N) remain confined in this small bulk volume (V), the osmotic pressure will become very large. Therefore, in order to grafted reduce this large osmotic pressure inside the bulk (with a small volume), some of the salt ions tend to migrate and localize inside the brushes, which is also helped by the fact that all the

salt in the nanochannel bulk is in close proximity to the brush layer (on account of the nanochannel induced confinement). This will be true for both the systems N1 and N3. On the other hand, for system N2, where there is no nanochannel and the bulk is significantly more extended, the osmotic pressure in the bulk is not large enough to enforce a migration of the salt ions towards and inside the PE brushes which is not in close proximity to most of the ions. Therefore, in system N2, overscreening is not observed in the absence of nanoconfinement.

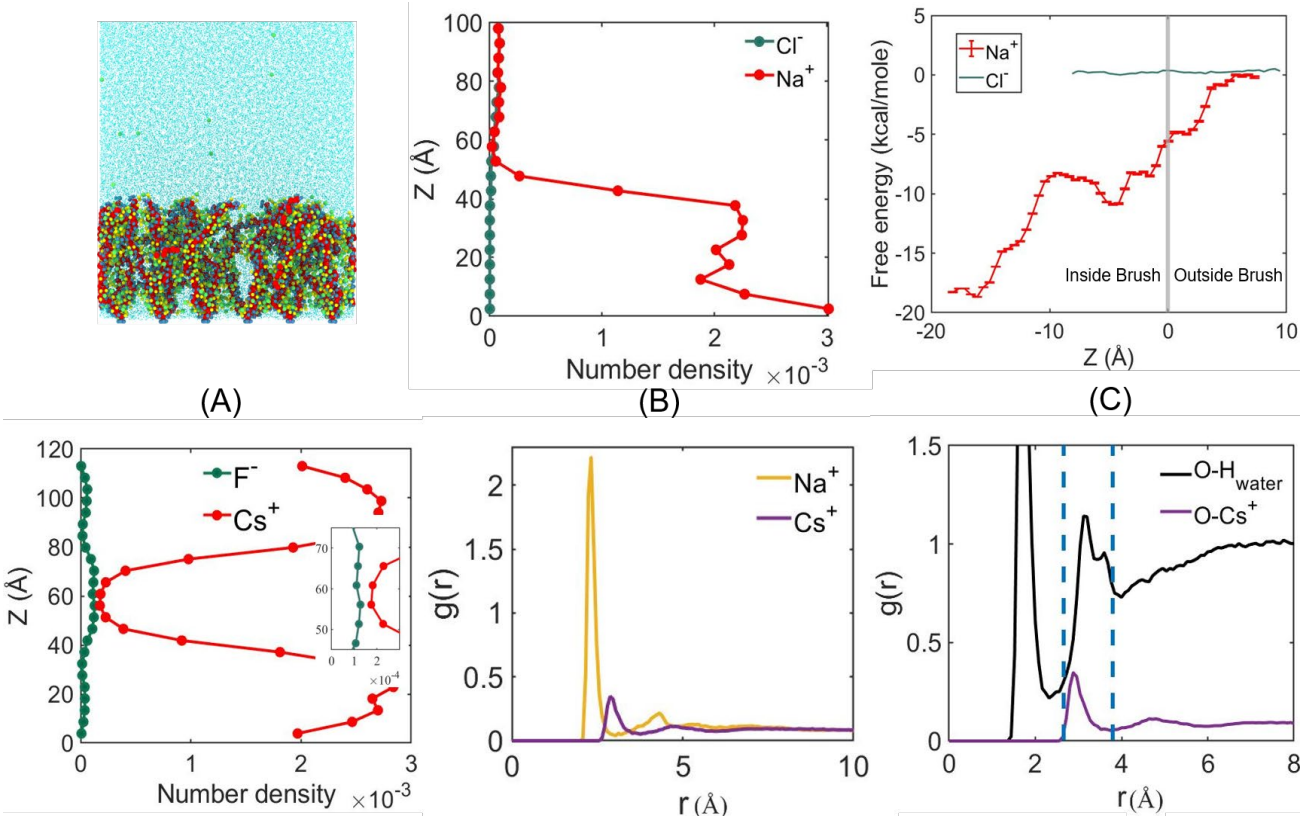

Figure 4.7: Understanding overscreening. (A) Simulation snapshot of the simulation without any confinement where PE brushes are grafted to a single interface (system N2). (B) Ion distribution profile for the system without confinement (system N2) (Y axis is truncated after 100 Å). (C) Free energy curves of Na^+ and Cl^- ions with Z coordinates of the ion serving as the reaction coordinates. These free energies are obtained from the simulation with nanochannel and NaCl salt (system N1). Here, Z=0 roughly indicates the interface of brush layer and brush-free bulk. For the curve corresponding to the Cl^- ion, the size of the error bar is less than the line thickness. (D) Ion distribution profile for system N3 (nanochannel grafted with PAA brush layers with CsF as added salt). (E) RDF of Na^+ and Cs^+ with O^- of carboxylate group. (F) RDF of H and Cs^+ with O^- of carboxylate group. The location of the first peak of the O^-- Cs^+ RDF is indicated with dashed line [Y axis is truncated after g(r)=1.5].

As discussed above, for both systems N1 and N3, osmotic pressure in the bulk will drive some salt ions from the bulk to inside the brush layer. The size of the Na^+ ion is smaller than the Cl^- and the size of the Cs^+ is distinctly larger than the F^- ion. Accordingly, there will be a much larger tendency of the Na^+ ions than Cl^-, and F^- ions than Cs^+ to migrate from the bulk to within the PE brush layer. For example, the solvation radii of the different ions considered here are as follow: 3.76 Å for Na^+, 3.84 Å for Cl^-, 4.52 Å for Cs^+, 3.33 Å for F^-. This size-based larger tendency of the Na^+ and F^- ions to enter the PE brush layer is effectively a size-based exclusion (or steric effect). The third and final issue, which also depends on the relative sizes (and hence the charge densities) of the Na^+ and Cs^+ ions (although this is not a size-based exclusion effect), is related to what extent the Na^+ and Cs^+ ions neutralize the O^- of the COO^- group, *i.e.*, form the $–COO^-Na^+$ or $–COO^-Cs^+$ ion pair. Formation of such ion pair, induced by the attraction between opposite charges, is of course energetically very favorable. Larger the extent of this neutralization, larger will be the favorability of the cations (that have entered the PE brush layer) to remain (in a stabilized configuration) within the brush layer. In this regard, we first computed the percentage of $–COO^-$ groups neutralized by the Na^+ ion for system N2 (*i.e.*, without nanoconfinement). In order to do so, we considered the O of COO^- and checked if one or more Na^+ ions were present inside the first solvation shell of this O or not. We found that around 80% of the O atoms of COO- are neutralized with the help of Na^+ ions, while the remaining O^- atoms were fully surrounded by the hydrogen of water (H_{water}). On the other hand, in the PE-brush-grafted nanochannel case with NaCl as the added salt (*i.e.* system N1), 95.3% of the O atoms of the COO- were neutralized by Na^+ ions. From these two observations, we can infer that in an equilibrium, while it suffices if 80% of the O atoms of COO^- are neutralized by the Na^+ ion, availability of higher number of Na^+ ions within the PE layer makes it feasible for some of these Na^+ to replace the H of water and themselves

neutralize the O atoms of the COO-. The larger charge density of the Na^+ ions ensures that such replacement (and the subsequent formation of the COO-Na^+ ion pair) is energetically more favorable. All these factors eventually ensure that the PAA brush layer grafted on the inner walls of the nanochannels can have more cations (in a stable configuration) than it requires for being in an equilibrated state, and eventually causes the overscreening. To observe this energy favorability of Na^+ ions within the PE brush layer, we have performed two free energy calculations for system N1. From the free energy curves, we can see that it is distinctly more favorable for the Na^+ ion to remain inside the brush layer [see Fig. 4.7(C)]. It is also clear that, energy favorability of the Na^+ ion is more around a COO^- functional group (present at Z=-5 Å and Z=-16Å), as confirmed by the presence of the local minima in the plot for these Z values. On the other hand, for Cl^- ion no such energy favorability is observed inside the brush layer. Obviously, such free energy calculations also confirm the tendency of the Na^+ to accumulate within the PE layer in concentrations that is much more than that needed to screen the PE charges, which in turn leads to the occurrence of the overscreening effect.

In this context, we also study what happens for the system N3, where the cations are the Cs^+ ions. Cs^+ ions are found to neutralize only around 53% of the O of COO^- of the PE brush layer. Two factors are responsible for it with both being related to the size of the Cs^+ ions. Cs^+ ion is larger than Na^+ ion. As a result, much lesser amount of Cs^+ ions can enter the PE brush layer (being driven by the osmotic pressure in the bulk), as discussed above. Secondly, again due to the large size of the Cs^+ ions, the first peak of the O-Cs rdf (radial distribution function) is very far from the location of the peak of the O-Na rdf [see Fig. 4.7(E)]. More interesting is the fact that the first peak of the O-Cs rdf occurs at a distance (from O of the COO-) that is similar to the distance (from O of the COO-) where the second peak of the O-H_{water} rdf occurs [see Fig. 4.7(F)]. Therefore, if

anything, Cs^+ ion will only be capable of replacing the H_{water} from the second solvation shell of O of COO^-. This implies that Cs^+ ions are unable to replace the neutralizing H_{water} of the *first* solvation shell of the O atoms of COO^-. The energy gain associated with replacing the neutralizing H_{water} from the second solvation shell by Cs^+ ions is significantly smaller than the energy gain associated with replacing the neutralizing H_{water} from the first solvation shell by the Na^+ ions, stemming from the fact that H_{water} in the first solvation is much more tightly bound to the O of COO^-. So, the possible energy favorability associated with the Cs^+ ions remaining localized (*via* electrostatic attraction) within the PE brush layer is significantly smaller as compared to the Na^+ ions remaining localized (*via* electrostatic attraction) within the PE brush layer. Accordingly, a significantly more number of Na^+ ions can be present within the PE brush layer thereby leading to eventual overscreening, while the number of Cs^+ ions that can remain localized within the PE brush layer is much less and hence there is no overscreening for the case N3.

We want to conclude this section with a discussion on the effect of the degree of ionization of the PAA brushes on the possible overscreening effect. It is known that PAA is a weakly dissociating polymer, although its degree of ionization depends on several parameters like the pH of the solvent, the concentration of the added salt, *etc*. For example, at a pH value that is above its pK_a (~5), PAA is likely to be highly ionized [60], which will be similar to what is considered in our study. On the other hand, in a prior all-atom MD simulation study [100], we showed that the extent of Na^+ counterion condensation in the PE brush remained very high even for weakly ionized PAA brushes. For example, even with f=0.25 (where f is the ratio of the deprotonated functional groups to the total number of functional groups of the PAA chains; therefore f=0 implies a neutral PAA brush, while f=1 implies a fully ionized PAA brush), we found that more than 90% of the counterions were condensed on the PAA chains [100]. Such a large extent of counterion

condensation will imply that even for weakly ionized PAA brushes, $–COO^-Na^+$ interactions (in presence of Na^+ screening counterions) will make a significant contribution to the overall free energy of the system. As discussed above, such a strong counterion-(PE-functional-group) interaction is a major driver of the overscreening effect. Therefore, we believe that even for the case of a nanochannel grafted with weakly ionized PAA brushes, the strong $–COO^-Na^+$ interactions will ensure that there will be overscreening effect within the PAA brush layer.

Experimental relevance of the present study

Charge inversion or overscreening is observed in experiments involving silicone nanochannels [146,147] in presence of large concentrations of salts with multivalent ions. Overpopulation of multivalent counterions in the Stern layer adjacent to nanochannel wall causes the overscreening. On the other hand, in our study we have observed this overscreening with monovalent counterions, where the interplay of the presence of a strong nanoconfinement and the presence of the densely grafted charged PE brushes create an environment that force an accumulation of more than required counterions within the PE brush layer and triggers overscreening. Also, in these studies [146,147], this overscreening scenario cannot be altered by the application of electric field, while in our study we can make the overscreening disappear at significantly larger electric field. A recent experiment, coupled with DFT calculations on protein−spherical nucleic acid conjugates, showed that above a certain salt concentration, a monovalent cation (Rb^+) can overcompensate the negative charges of the DNA molecules (densely grafted on gold nanoparticles), thereby causing an overscreening-like scenario [148]. This study, along with our all-atom MD simulation results demonstrating overscreening in presence of monovalent Na^+ screening counterions, suggest that explicit solvent all-atom MD simulations and quantum calculations can potentially play an important role in furthering our understanding of the

overscreening of local charges of polyelectrolyte molecules even in presence of monovalent counterions.

It is well known that in a nanochannel due to the surface charge of the wall, there will be an electric double layer or an EDL and hence an imbalance in the number density of the positive and negative ions within the EDL: in presence of an applied electric field, the mobile ions are transported and this imbalance ensures that the water molecules are transported in the direction of the migration of the ions that are larger in number within the EDL. For our case, at low electric field strengths, the presence of the overscreening effect within the PE brush layer implies that the coions are excess in number in the bulk and hence the EOS transport, in presence of the applied electric field, occurs in the direction of migration of the coions. Therefore, for this case, we indeed find that the EOS (electroosmotic) motion occurs due to the imbalance in the number of coions and counterions, albeit for the classical scenario the EOS transport primarily occurs due to the excess of counterions within the EDL. On the other hand, for larger electric field, the overscreening within the PE brush layer becomes negligible and there is equal number coions and counterions within the bulk: under such circumstances, the EOS transport occurs (in the direction of migration of the counterions) due to the larger residence time of water molecules within the counterions (Na^+ ions) than the coions (Cl^- ions). Therefore, the key mechanism of our reported EOS transport at large electric fields is different from that of the classical EOS transport. Despite that, the order of magnitude of our reported EOS transport at large electric fields is very similar to that reported in our previous experiments. For example, the EOS mobility, which is defined as EOS velocity per unit applied electric field has been reported to be in the order of $(1-10)\times 10^{-9}\, m^2/(Vs)$ for experiments [137, 138, 149] while that computed for our simulations (for large electric field strength of 1 V/nm) is ~ $5.5\times 10^{-9}\, m^2/(Vs)$.

Also, in an experimental setup, there can be a reservoir of solution connected to a nanochannel and water and ions can move from the nanochannel to the reservoir and vice versa. To check the effect of reservoir in the overscreening scenario, we have performed one more simulation where the nanochannel is connected to two reservoirs at its two ends. We find that the density of coions are larger within the bulk, confirming the occurrence of overscreening within the PE brush layer of the nanochannel even when the nanochannel is connected to two reservoirs on its two ends (figure 4.8). Details of the simulation can be found in the method section.

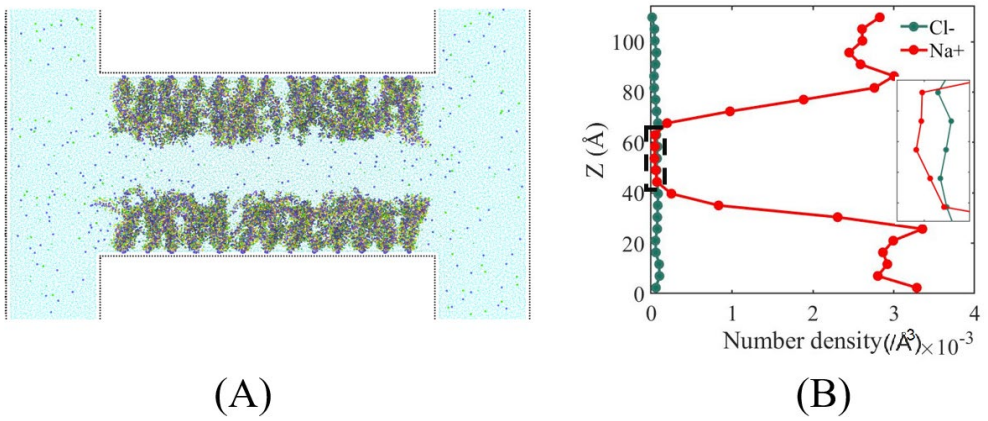

Figure 4.8: Nanochannel with reservoir. (A) Simulation setup of the PE brush grafted nanochannel with the nanochannel being connected to two reservoirs at its two ends (system 7). (B) Ion distribution profile in the nanochannel. Yellow shaded region in (A) is considered for calculating the ion distribution profile [reported in (B)] within the nanochannel.

4.3 Method

Our main simulation contains [shown in Fig. 4.1(A)], fully ionized Polyacrylic acid (PAA) chains (H[-CH_2-CH(COO^-)-]nCH3) as the polyelectrolytes and SPC/E water molecules [67]. Sodium (Na^+) counterions screen the PE brush charges. In addition, we add 0.1 M NaCl salt. PE chains are grafted with a grafting density of $0.05/\sigma^2$ (σ=3.5 Å, is the LJ distance parameter of backbone carbon atoms). This grafting density of PAA chains is within the range of experimentally reported [60] grafting densities of 0.12-2.15 chain/nm^2 (in the chain/nm^2 unit, the grafting density

considered for our case is 0.408 chain/nm^2). Each chain has 49 backbone carbon atoms. Purely repulsive walls are placed at the top and the bottom of the system to prevent the mobile ions and water molecules from escaping the system. 90 PE chains are grafted on each wall in a 15*6 (x*y) array. The particle trajectories are calculated using the Velocity-Verlet algorithm, with a time step of 2 fs. Non-bonded interactions are modelled as the sum of a shifted-truncated 12-6 Lennard Jones potential (U_{LJ}) with a cut-off of 13Å. Long range Columbic interaction is calculated using a PPPM (particle-particle particle-mesh) algorithm [68]. The bonds and angles of water molecules are conserved by using the SHAKE algorithm [69]. Our simulation system consists of a total of 277340 atoms. Dimensions in x, y, and z directions are 23.5 nm, 9.4 nm, and 12 nm respectively. Periodic boundary conditions are applied in x and y directions while the fixed boundary condition is incorporated in z direction. Simulations are performed in LAMMPS [70] and OVITO [71] is used to visualize the simulation system.

The system is first run in the NP_zT ensemble (the subscript z signifies that only the channel

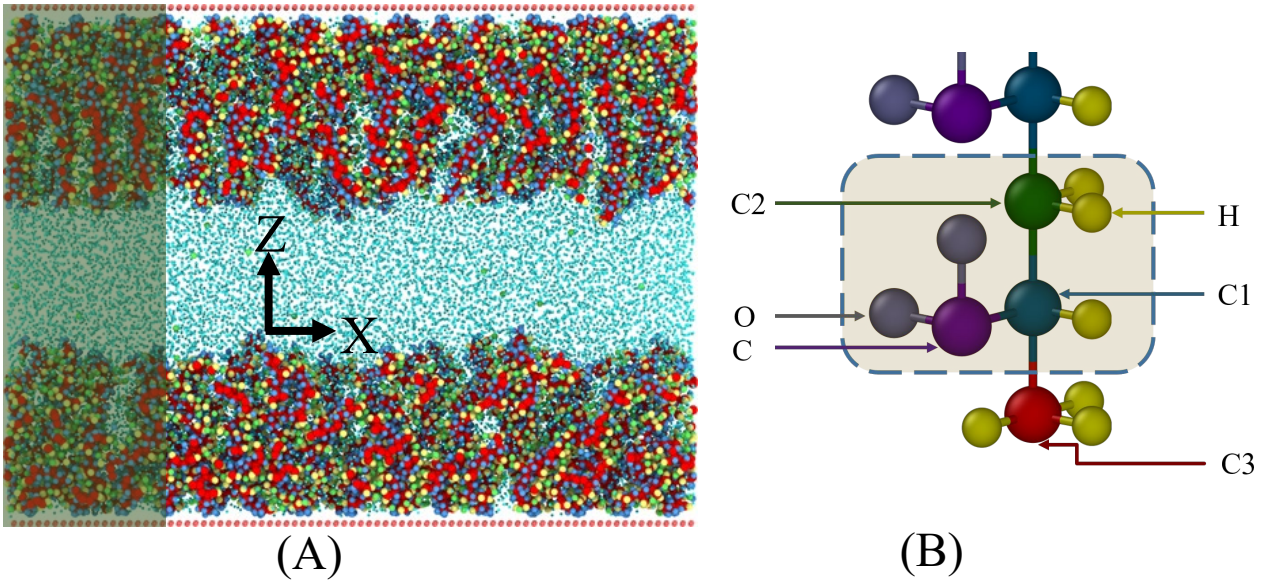

Figure 4.9. Schematic showing thermostated region and atomic structure**.** (A) A schematic of the PE brush grafted nanochannel system. Left shadowed section indicates the thermostated solvent region. (B) A schematic representation (not to scale) of the fully ionized PAA molecule. Atom types are indicated with arrows. Polyelectrolyte's (PE's) repeating unit is indicated with the shaded box.

height is allowed to change) to obtain the correct simulation box height at 300 K and 1 atm, by applying the Nosé-Hoover thermostat and barostat [79,80]. Subsequently, the system is equilibrated in the NVT ensemble for 16 ns to obtain the correct equilibrium configuration of the system by applying the Langevin thermostat [81]. After initial equilibration, we have applied the electric field under the NVT ensemble to remove the heat dissipated due to the flow. NVT is applied only in the direction perpendicular to the axial electric field and to avoid a flow profile bias, we have removed bias velocity with the help of a binning method employed in a direction perpendicular to the flow field. For more caution, only polymers are thermostatted in the entire system, this mimics the experimental scenario where temperature can be controlled form the outer surface. Only, the water molecules and mobile ions in the extreme left quarter of the simulation domain (in the x-direction) were thermostatted as depicted in figure 4.9(A). These simulations are performed for 8 ns to get steady-state velocity profile followed by a 12 ns production run.

We have used the OPLS-AA [72] force field to model the brush molecules and employed Joung *et al*. [73] for calculating the potentials for the mobile ions. These vastly used parameters for monovalent ions were adjusted to the solvation free energy of ions in water and the lattice energy of ionic crystals. OPLS force field, which is used to model the PE brush molecule, has been used for modeling a variety of polymer systems such as hydrocarbons, proteins, rubbers, [74-76] *etc*. as the most accurate force field parameter. Geometric mixing rules are used for the LJ interactions between dissimilar atoms, except for the ion-ion and ion -water interactions. For these ion-ion and ion-water, we have used Lorentz-Berthelot mixing rules to be consistent with Joung *et al.*

Applied electric field might add additional complexities in the atomic interactions between various species, thereby raising concerns about the validity of the force field. Applied electric field

introduces electroosmotic flow inside the PE brush grafted nanochannel; so, accuracy of water model under electric field is important to consider. Saitta et al [62] showed that characteristic order parameters changed by less than 2% under electric fields of up to 2 V/nm. We also haven't observed significant change in the atom distribution (e.g.; RDF) in the electric field of up to 1 V/nm. Shafiei et al. [150] also checked the effect of polarizability of water model under the influence of the applied electric field. They performed simulations with SPC/E (nonpolarizable), SWM4-NDP (polarizable), and BK3 (polarizable) water models. All these models show qualitatively similar behavior for hydrogen bonds and static and kinetic properties of other order parameters. Diffusivity of water in presence of an electric field also shows qualitatively similar behavior, although SPC/E slightly overestimates the diffusivity in very large electric field. These studies suggest that our use of SPC/E water model as explicit solvent is accurate under the range of electric field strengths that we have considered.

To calculate free energy calculations in our main simulation setup [results shown in Fig. 6(C)], a Na^+ ion and a Cl^- ion located inside the brush layer have been chosen. These two ions are pulled out from brush layer to the bulk by specifying the reaction coordinate in Z direction that varies by 1 Å in every successive reaction coordinate. For Na^+ and Cl^- ions, 26 and 18 reaction coordinates are considered, respectively. These ions were constrained to their windows by a harmonic potential with spring constant of 5 kcal/mol.$Å^2$. All these simulations lasted for 2 ns and the data collected from the last 1.5 ns was used for analysis. The axial positions of the sample molecules were outputted every 20 fs and the weighted histogram analysis method (WHAM) [151, 152] was used to analyze the data generated from umbrella sampling.

The Lennard-Jones (LJ) potential (U_{LJ}) used in the simulations is expressed as:

$$U_{LJ} = 4\epsilon_{ij}\left[\left(\frac{\sigma_{ij}}{r_{ij}}\right)^{12} - \left(\frac{\sigma_{ij}}{r_{ij}}\right)^{6}\right], \quad (4.1)$$

while the Coulombic pairwise interaction (U_{Coul}) used in the simulation is expressed as:

$$U_{Coul} = \frac{q_i q_j}{4\pi \in_0 \in_1 r_{ij}}. \quad (4.2)$$

In these equations, ϵ_{ij} is the depth of the LJ potential well between atoms i and j, σ_{ij} is the distance where the LJ potential between atoms i and j, q_i and q_j are charges of the i^{th} and j^{th} atoms, r_{ij} is the distance between atoms i and j, $\in_0$ is the permittivity of vacuum and $\in_1$ the relative permittivity of the background (taken to be 1).

The values for these parameters [required for eqs. (4.1,4.2)] for all atom types, shown in Fig. 4.9(B), have been summarized in Table 4.2.

Atom Type	**Charge (e)**	**Mass (amu)**	**ϵ (Kcal/mole)**	**σ (Å)**
C3 (CH_3)	-0.18	12.011	0.066	3.50
C2 (CH_2)	-0.12	12.011	0.066	3.50
C1 (CH, Attached to COO-)	-0.16	12.011	0.066	3.50
C (COO-)	0.70	12.011	0.105	3.75
H	0.06	1.008	0.03	2.50
O (COO-)	-0.80	15.999	0.210	2.96
O_w (H_2O)	-0.8476	15.999	0.155354	3.166
H_w (H_2O)	0.4238	1.008	0	0
Na	1.00	22.99	0.3526418	2.1595
Cl	-1.00	35.453	0.012785	4.83
Continuous LJ Wall (Parameters remain unchanged for interaction with all atom types)	0.00	15.00794	0.1947	3.00 (LJ cut off length is 3.36 Å)

Table 4.2: Charge, mass and LJ parameters for all the different atom types

Harmonic bond style is used to calculate the potential energy for bond:

$$U_{bond} = K_b(r - r_0)^2. \qquad (4.3)$$

Here, r_0 is the equilibrium bond length and K_b is bond stiffness. The values for r_0 and K_b for all bond types are provided in Table 4.3.

Bond Type	$\boldsymbol{K_b}$, $(\frac{\boldsymbol{Kcal}}{\boldsymbol{mol.\text{Å}^2}})$	$\boldsymbol{r_0}$, (Å)
C2-H	340.0	1.09
C2-C1	268.0	1.529
C1-H	340.0	1.09
C3-H	340.0	1.09
C-C1	317.0	1.522
C1-C3	268.0	1.529
C-O	656.0	1.25
O_w-H_w	-	1.00

Table 4.3: Bond parameters used in the simulations

The potential energy for the finite angle between different bonds is calculated using the following harmonic equation:

$$U_{angle} = K_a(\theta - \theta_0)^2. \qquad (4.4)$$

Here, θ_0 is the equilibrium value of the angle and K_a is the angle stiffness. The values for θ_0 and K_a for different angles are provided in Table 4.4.

Angle Type	$\boldsymbol{K_a}$, $(\frac{\boldsymbol{Kcal}}{\boldsymbol{mol.rad^2}})$	$\boldsymbol{\theta_0(deg)}$
H-C2-H	33.00	107.8
H-C2-C1	37.5	110.7
C2-C1-H	37.5	110.7
C1-C3-H	37.5	110.7

H-C3-H	33.00	107.8
H-C1-C	35.0	109.5
O-C-O	80.0	126.00
C2-C1-C	63.0	111.1
C3-C1-C	63.0	111.1
H_w-O_w-H_w	-	109.47
C2-C1-C2	58.35	112.7
C2-C1-C3	58.35	112.7
C1-C-O	70.0	117.0
C3-C1-H	37.5	110.7
C1-C2-C1	58.35	112.7

Table 4.4: Angle parameters used in the simulations

The potential energy associated with the 4-atom dihedral torsion interactions is given by

$$U_{dihedral} = \frac{1}{2}K_1[1 + \cos(\emptyset)] + \frac{1}{2}K_2[1 - \cos(2\emptyset)] + \frac{1}{2}K_3[1 + \cos(3\emptyset)] + \frac{1}{2}K_4[1 - \cos(4\emptyset)]. \quad (4.5)$$

Here, K_1, K_2, K_3 and K_4 are the four Fourier coefficients for torsional interactions, and $\emptyset$ is the torsional angle. Values of K_1, K_2, K_3 and K_4 are provided in Table 4.5.

Dihedral type	$\boldsymbol{K_1}$, $(\boldsymbol{Kcal/mole})$	$\boldsymbol{K_2}$, $(\boldsymbol{Kcal/mole})$	$\boldsymbol{K_3}$, $(\boldsymbol{Kcal/mole})$	$\boldsymbol{K_4}$, $(\boldsymbol{Kcal/mole})$
H-C2-C1-H	0.0	0.0	0.30	0.0
H-C2-C1-C	0.0	0.0	-0.10	0.0
H-C2-C1-C2	0.0	0.0	0.30	0.0
H-C2-C1-C3	0.0	0.0	0.30	0.0
H-C1-C-O	0.0	0.0	0.00	0.0
H-C1-C3-H	0.0	0.0	0.30	0.0
C2-C1-C-O	0.0	0.82	0.00	0.0
C2-C1-C2-C1	1.30	-0.05	0.20	0.0

H-C3-C1-C2	0.0	0.0	0.30	0.0
C3-C1-C-O	0.0	0.82	0. 0	0.0
C1-C2-C1-C	-3.185	-0.825	0.493	0.0
C1-C2-C1-C3	1.30	-0.05	0.20	0.0
H-C1-C2-C1	0.0	0.0	0.30	0.0
H-C3-C1-C	0.0	0.0	-0.10	0.0

Table 4.5: Dihedral parameters used in the simulations

The potential energy associated with the improper torsional dihedrals are modelled using the harmonic function:

$$U_{improper} = K_i(\varphi - \varphi_0)^2. \quad (4.6)$$

Here, φ_0 represents the equilibrium value of the improper torsional angle and K_i is the improper torsional stiffness. Their values for the C1-O-C-O system is provided in Table 4.6.

Improper Type	$\boldsymbol{K_i}$ $(\frac{\boldsymbol{Kcal}}{\boldsymbol{mol.rad^2}})$	$\boldsymbol{\varphi_0(deg)}$
C1-O-C-O	10.5	180

Table 4.6: Improper dihedral parameters used in the simulations

Below we describe the key parameters used for modeling the PMMA brushes:All the force field parameter of the PMAA brush is taken from OPLS database. A schematic of the PMAA monomer is given in figure 4.10. The difference with PAA is that, one H connected to the C (connected to COO-) is replaced with a methyl group.

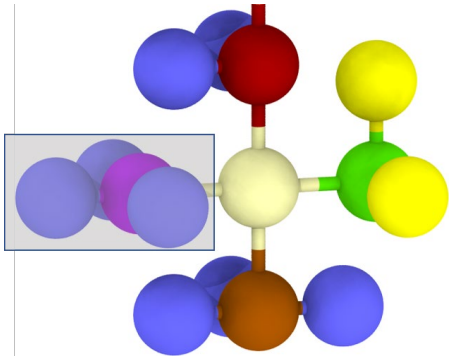

Figure 4.10: A schematic of the PMAA monomer**.** The replacing methyl group is shown with a rectangular box.

To check the generality of the overscreening, we have performed a few more simulations with grafting density, salt concentration, and PE brushes that are different as compared to those studied and discussed in the main paper. Key specifics of these new simulations are listed below:

System i: A nanochannel grafted with PAA polyelectrolyte (PE) brushes with a grafting density of $\mathbf{0.03/\sigma^2}$ (with Na^+ screening counterions) in presence of 0.1 M NaCl added salt. To conduct these simulations 80 PE brushes were grafted in an 8*5 array. Other parameters of the simulations remain same as that of the main simulations reported in our main paper.

System ii: A nanochannel grafted with PAA polyelectrolyte (PE) brushes with a grafting density of $0.05/\sigma^2$ (with Na^+ screening counterions) in presence of **0.2 M NaCl added salt**. To conduct these simulations, 120 PE brushes were grafted in a 10*6 array. Other parameters of the simulations remain same as that of the main simulations reported in our main paper.

System iii: A nanochannel grafted with **Polymethacrylic acid (PMAA)** brushes with a grafting density of $0.05/\sigma^2$ (with Na^+ screening counterions) in presence of 0.1 M NaCl added salt. To conduct this simulation, 120 PMMA PE brushes were grafted in a 10*6 array. Other parameters of the simulations remain same as that of the main simulations reported in our main paper.

As discussed in the result and discussion section, in an experimental setup, there can be a reservoir of solution connected to a nanochannel. To check the effect of reservoir in the overscreening scenario, we have performed one more simulation as shown in figure 4.8(a). In this system, the nanochannel grafted with PAA brushes (with a grafting density of $0.05/\sigma^2$ *and having with* Na^+ *ions as screening counterions and an added 0.1 M NaCl salt*) is connected to two reservoirs at its two ends and approximately $1/5^{th}$ of the total water stays in the nanochannel (and the rest is within the two reservoirs). Initially the salt ions are distributed randomly in the nanochannel and in the reservoirs. A total 156 brushes are grafted in the nanochannel. The changes in the brush height and ion distributions are monitored to check for equilibrium.

4.4 Conclusion

In summary, our study shows (a) overscreening within the PE brush layer for zero or small electric field even in presence of monovalent counterions, (b) coion-dictated EOS velocity for smaller electric field, and (c) counterion-dictated EOS velocity field for larger electric field (which also indicates an electric field strength mediated switching of the direction of EOS transport) in nanochannels grafted with PE brushes. All these facets are dictated by an intricate interplay of the electric field driven (a) reduction in brush height caused by the electric field mediated preferential alignment of the brushes, (b) variation in velocities (mobilities) of coions (Cl^-) and counterions (Na^+), and (c) variation in residence times of the water molecules within the first solvation shells of the Cl^- and Na^+ ions. We anticipate that the findings of this chapter will not only inspire future, well-resolved atomistic exploration of electrohydrodynamics of functionalized nanochannels unraveling physics at the interface of soft matter, chemistry, fluid mechanics, and nanoscience, but will also enable designing nanodevices with a better and easy control over the associated flows.

Chapter 5: Counterion Specific Ion Distribution and Electroosmotic Flow in a Polyelectrolyte Brush Grafted Nanochannel

Abstract: *Controlling ion distribution in a PE (polyelectrolyte) brush grafted nanochannel is central to the use of such channels in energy generation, sensing, current rectification, etc. Here, we have performed all-atom molecular dynamics (MD) simulations to understand the ion distribution inside a PE brush grafted nanochannel for counterions (screening the PE charges) of different valences and sizes. We probe the cases where the PE (fully charged Polyacrylic acid) brushes are screened by Na^+, Cs^+, Ca^{2+}, Ba^{2+}, and Y^{3+} counterions: for each of these cases, we consider an added salt with Cl^- ion as coion and the same corresponding cation as the counterion. We have found that counterion valence and size dictate the number of ions present in the brush-free bulk. Counterions with a greater valence and a smaller size prefer to remain localized inside the brush layer as compared to counterions with a smaller valence and a larger ionic radius. We have also found that there are invariably more coions (Cl^-) in the bulk than counterions (for counterions such as Na^+, Ca^{2+}, Ba^{2+}, Y^{3+}): this is a manifestation of the overscreening (OS) behavior. On the other hand, the monovalent nature, as well as the larger size of the Cs^+ ion ensures that the number of Cs^+ remains higher than the Cl^- ions inside the brush-free bulk: therefore, there is no OS behavior for the case of the Cs^+ ions. For all these different types of counterions, we have explained the corresponding ion distribution behaviors by discussing the electrostatic interactions and entropy changes associated with the presence of the counterions inside and outside PE brush layer. We have also found that the application of a large electric field (E=1 V/nm) alters the ion distribution in a nanochannel grafted with PE brush neutralized with Na^+, Ba^{2+} counterions. The electric field enables few counterions to leave the brush layer and go to the bulk: this makes the OS of the PE brush layer disappear and the number of counterions in*

the bulk more than the number of coions. For smaller electric fields (E=0.1 V/nm), these effects are not evident for the nanochannel grafted with PE brush neutralized with Na^+, Ba^{2+} counterions. On the other hand, no such electric-field-mediated disappearance of OS is observed (for any value of the electric field) for the case of nanochannel grafted with PE brushes screened by Ca^{2+} and Y^{3+} ions; we attribute this to the very strong attachment of these two types of counterions to the negatively charged monomers (which enforce them to remain attached to the PE brush molecules even in the presence of the strong applied electric field). These specific ion distributions ensure that in presence of an applied electric field strength of 0.1 V/nm, there is coion-dominated electroosmotic (EOS) flow for the case of PE-brush-grafted nanochannel with PE brushes screened with Na^+, Ca^{2+}, Ba^{2+}, and Y^{3+} counterions (and having the added chloride salt with the corresponding cation). For the same reason, at E=1 V/nm, there is counterion-dominated EOS flow for for the case of PE-brush-grafted nanochannel with PE brushes screened with Cs^+ counterions (and having the added CsCl salt). On the other hand, the disappearance of the OS effect and the presence of a greater number of counterions inside the brush-free bulk ensures that at E=1 V/nm, EOS flow in PE-brush-grafted nanochannel become counterion-dominated (and hence the flow direction is reversed) for the case of Na^+, Ba^{2+} screening counterions. Finally, there is no change in EOS flow direction at E=1 V/nm for the case of Cs^+ counterions (i.e., the flow still remains counterion-dominated) and the Ca^{2+} and Y^{3+} ions (i.e., the flow still remains coion-dominated).

5.1 Introduction

Over the past couple of decades, nanochannels have attracted significant attention from scientist and engineers because of their immense potential for novel nanoscale applications [153-156]. In a nanochannel, the channel height is typically below 100 nm, which introduces new nanoscale phenomena that would be unattainable in a larger channel. Functionalizing nanochannels (for example, by grafting the inner walls of the nanochannel with polyelectrolyte (PE) brushes), can be utilized (by leveraging the environmental-stimuli responsiveness of the PE brushes) for applications such as bioanalayte sensing [14, 131], fabrication of ionic diodes [48, 135], nanofluidic current rectification [84, 85], oil recovery [18], targeted nanoparticle-based delivery [16, 17], etc. Most of these applications rely on the manner in which the PE brushes interact with the mobile ions (e.g., ions serving as counterions screening the PE brush charge as well as the ions of the added salt) present inside the nanochannel leading to unique ion distributions inside the nanochannel dictated by the valence and size of these ions.

When electrolytes come near a charged surface, free ions (of charges opposite to that of the charged surface) from the electrolyte try to neutralize the charged surface and form an electric double layer (EDL) [157]. Under such circumstances, the charge within the EDL is always expected to be of the same sign as that of the charged surface where the EDL has been induced. Sometimes when these oppositely charged ions are multivalent in nature, there is an overcompensation of this screening of the surface charge and the result is a charge within the EDL that is the opposite sign to that of the surface charge. This phenomenon is known as charge inversion and the overcompensation caused by the multivalent counterions is known overscreening (OS). Although historically OS has been attributed to be caused by multivalent counterions only, evidence of monovalent (Rb^+) counterion mediated OS has recently been found through

experiments and quantum simulations [148]. Our recent study also shows that a nanochannel grafted with PE brush can create an ideal environment for monovalent-counterion-induced OS effect [see chapter 4].

Ion distribution inside a nanochannel can dictate how the electrolyte solution will respond to an applied electric field [158]. Electric field imparts force to the charged ions; in response, the ions, depending on their charges, move along or opposite to the direction of the electric field. These ions can carry water in their solvation shells: therefore, their motion in presence of the applied electric field eventually leads to an electroosmotic (EOS) flow of the solution (as long as there is an imbalance in the extent to which the positive and negative ions, on the basis of the disparities in their numbers or their interactions with the water, can carry the water molecules with them). As the PE brush has the potential to control the ion distribution in a nanochannel, it can also control the strength and direction of the EOS flow. As we know from our previous studies (chapter 2 and 4) that an electric field can modify the brush structure and ion distribution for Na^+ counterions; it is possible that the electric field modifies the ion distribution for other ions also. So, understanding the PE-brush-supported ion distribution for different screening counterions and how they change under an electric field can be vital for understand the electroosmotic flow in a PE brush grafted nanochannel for cases where the PE brushes are screened with counterions of different sizes and valence.

In this chapter, we employ all-atom molecular dynamics simulations to study the ion distribution in PE brush grafted nanochannels for the case where counterions of different valences screen the PE brush charge. Our aim is to identify the manner in which the counterion size and valence dictate the ion distribution (especially the OS effect) inside the brush-grafted nanochannel. Therefore, we probe the cases where the PE brushes are screened by Na^+, Cs^+, Ca^{2+}, Ba^{2+}, and Y^{3+}

counterions: for each of these cases, we consider an added salt with Cl^- ion as coion. Our simulations show that ion distribution in a PE brush grafted nanochannel strongly depends on counterions size, valence, and more importantly on the philicity of the counterions to the PE layer. We have also discussed the occurrences of overscreening for Na^+, Ca^{2+}, Ba^{2+}, Y^{3+} counterions and lack of it for Cs^+. We have discussed possible enthalpic and entropic contributions coming from counterion-PE interactions, counterion solvation size, etc. We have also found that electric fields can alter the ion distribution for Na^+, Ba^{2+} counterions. Our study shows that EOS flow direction follows the relative density of coion and counterions in the brush-free bulk; overscreening leads to coion-dominated flow and otherwise counterion-dominated flow. We plan to include free energy calculation at the end of this project.

5.2 Results and Discussion

Equilibrium ion distribution in a PE brush grafted nanochannel

We have considered fully ionized Polyacrylic acid (PAA) chains ($H[-CH_2-CH(COO^-)-]nCH_3$) as the polyelectrolytes and explicitly-modeled water molecules act as the solvent in our nanochannel (shown in Fig. 5.1). Different screening counterions, namely Na^+, Cs^+, Ca^{2+}, Ba^{2+}, Y^{3+} are separately considered to neutralize the PE's negative charges. We have also added 0.1 M concentration of chloride salt (which is the chloride salt of same counterions as the screening counterions). This implies that for the case where the PE brushes are screened by the Na^+ (Ca^{2+}) screening counterions, we have considered the addition of 0.1 M NaCl ($CaCl_2$) salt, and so on. PE chains are grafted with a grafting density of $0.05/\sigma^2$ [σ=3.5 Å is the Lennard Jones (LJ) distance parameter of the backbone carbon atoms of the PE chains] with each chain having 49 backbone carbon atoms (24 repeating units). 25 chains are grafted one a given wall of the nanochannel in a

5×5 (X × Y) array. Further details about the simulation have been provided in the Methods section.

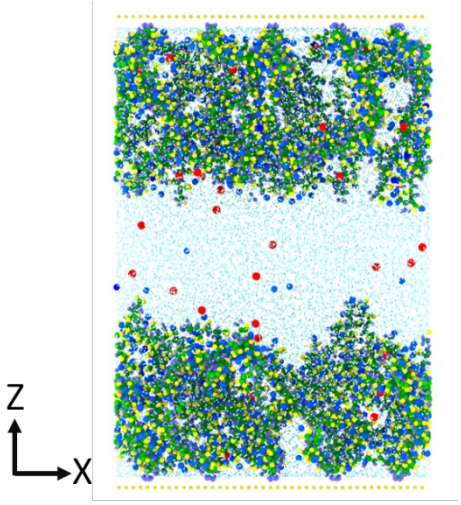

Figure 5.1: Snapshot of the simulation system studying in this chapter (shown here for Na^{+}) Blue circles are the counterions and reds are coion. Other circles are atoms of PE. Green small dots indicate water.

The main focus of this chapter is to understand the ion distribution inside a nanochannel consisting of a single layer of grafted PE brushes on each of its opposing walls. In figure 5.2, we have plotted the counterion and coion distribution inside the nanochannel for different cases of added counterions (and corresponding added salt). Counterions remain mostly localized inside the brush layer (in order to neutralize the negative charges of the PE brush layer): this can be observed by noting a larger number density of counterions inside and near brush layers. The propensity of counterion to stays inside the brush layer creates a depletion of counterion in the brush free bulk. In an ideal bulk (without any influence coming from nearby environment), the number density of coion and counterion should be same. Interestingly, the figures in the insets of Fig. 5.2(a-e), show that such coion and counterion parity is not present. It can be also observed that density in the bulk is also not similar for all the ions considered in this study.

We have calculated the averaged number density of coion and counterion in the bulk, shown in figure 5.3 (a). It can be seen from the bar-plot that that the number density in the bulk is

decreasing with an increase in the valance. One can also understand the effect of counterion size; increasing the counterion size, for counterions of given valence, increases the number density in the bulk.

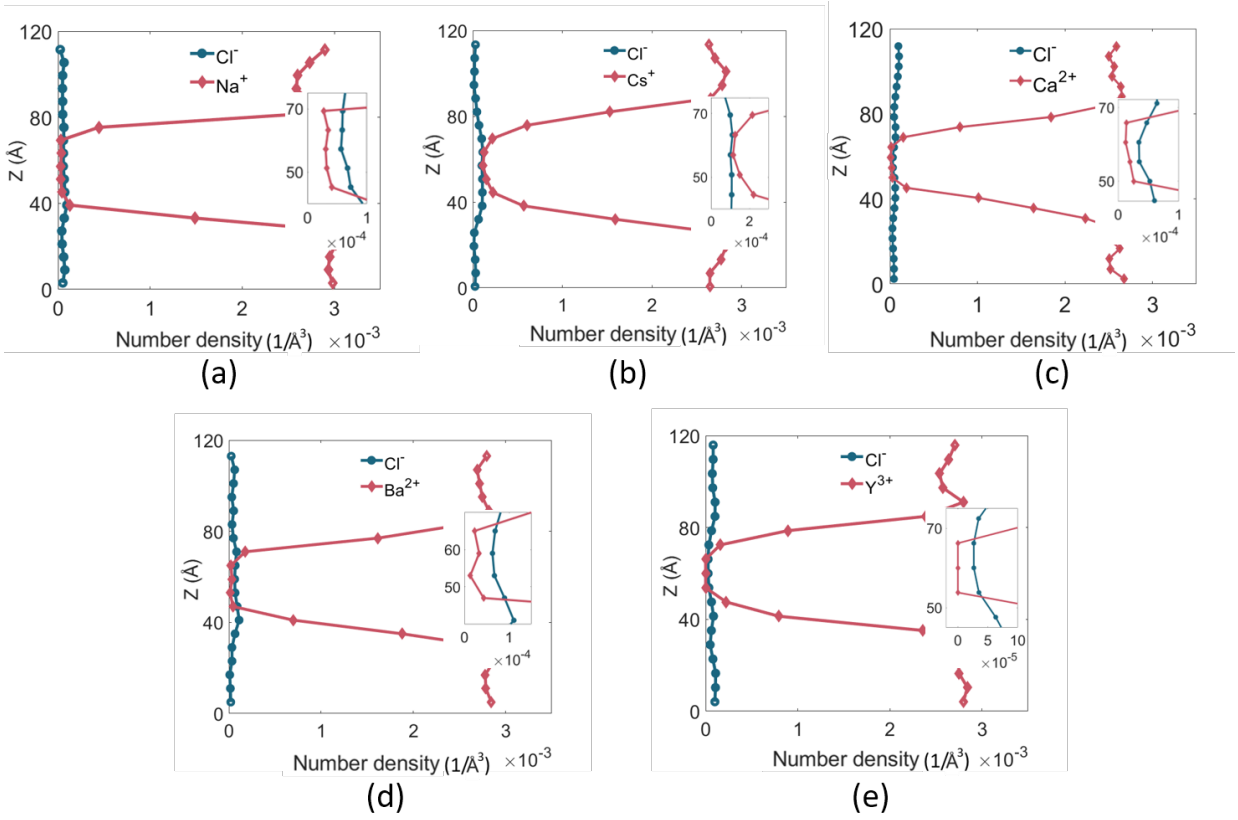

Figure 5.2: Mobile ion distribution in the simulation systems for different counterions. Counterion type is given in the legend. Ion distribution near bulk regions is shown in insets.

So, why number density in the brush free bulk behaves this way? Broadly, two possible things can control the number of ions inside the brush layer. Firstly, we are decreasing the number of counterions (needed to neutralize the same amount of PE brush charges) when we are increasing its valance. When the required number of counterions to neutralize the negative charges is high (e.g., for monovalent counterions); they create a higher osmotic pressure inside the brush layer. As the osmotic pressure is higher for monovalent ions, they create a scenario that prevent the

excess ions from entering the brush layer. This higher osmotic pressure is suggested to be one of the reasons for higher brush height for monovalent salt. Also, counterion loses entropy when they enter the brush layer as they get attracted to the PE monomer electrostatically. This electrostatically attracted (to the PE monomer) state of the counterion is entropically less favorable as compared to its state where it is more mobile and solvated by water molecules in the brush-free bulk. As monovalent counterions are higher in numbers inside the brush layer, the loss of entropy that they suffer (by remaining electrostatically attracted to the charged PE monomers) is much more than that suffered by the multivalent counterions. These effects combine to ensure that as compared to multivalent counterions, a greater number (or percentage) of monovalent counterions prefer to remain within the brush-free bulk.

Second, increasing the valence and decreasing the size of a counterion increases its charge density. Higher charge density indicates that a counterion can remain bound to the PE monomer more strongly. As a result, they are more prone to stay inside the brush layer. Here, Cs^+ stays in

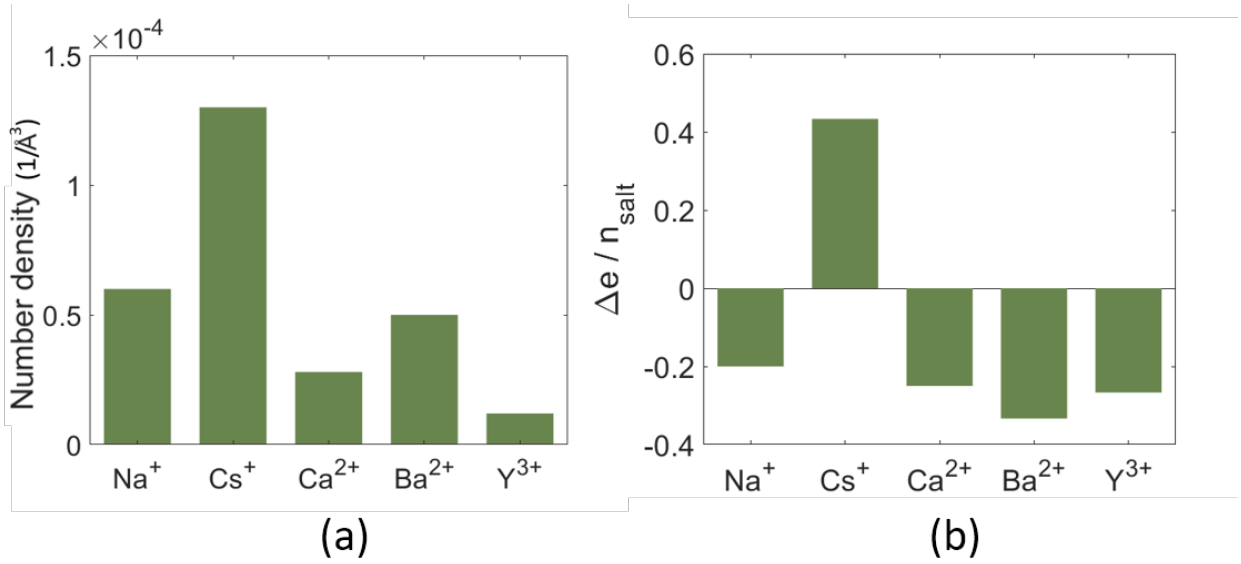

Figure 5.3: (a) Average number density of ion in the brush free bulk. (b) Difference in charges (normalized by the number of Cl^- ions present in the system), $\frac{\Delta e}{n_{salt}}$, in the brush free bulk layer. A negative value of $\frac{\Delta e}{n_{salt}}$ indicates the occurrence of overscreening.

the bulk more than any other counterions. In our previous study we have shown that because of its very low charge density, Cs^+ ion doesn't condense to the PE chain fully. Their lower charge density makes them less favorable to the PE chains, as compared to other counterions. Size and valance can also influence the entropic effects (associated with the water in the solvation shell of the ions). Cs^+ ion has a larger solvation shell as compared to Na^+ ion (similarly Ba^{2+} has a larger solvation shell then Ca^{2+} ion): as a result, Cs^+ has more water in its solvation shell than Na^+ (similarly for Ba^{2+} ion has more water in its solvation shell than the Ca^{2+} ion). If Cs^+ wants to stay inside the brush layer, the water bound to its solvation shell will also be trapped inside the brush layer. Such trapping means that more water will lose entropy inside the brush layer, making such trapping unfavorable. This effect, therefore, also contributes to larger counterions (with larger solvation shell) showing a greater propensity to stay in the bulk.

As entropy can be an important contributor in dictating ion distribution, we would like to explain the influence of entropy in details here. Counterions are added to the system to neutralize the PE charges. Outside the brush layer, the counterions are solvated by water: these solvation shells of the ions (with the ions being in the brush-free bulk) can be formed and broken quickly. Also, these counterions and solvated water can occupy different possible locations and orientations; accordingly, they have a greater probability to occupy different states when the counterions are outside the brush layer. On the contrary, when a counterion gets condensed to the PE chain, it loses its probability to occupy different states and its motion is essentially dictated by the motion of the PE chain or monomers. This restricted motion of the counterion leads to an entropic loss when the counterion enters the brush layer. When one increases the valence of counterions, the number of counterions required to neutralize the PE charges reduces. As a result, a fewer number of multivalent counterions will lose their entropy when they are inside the PE layer

and condensed to the PE chains. This entropic contribution (or lesser entropic penalty) is found to drive the replacement of monovalent counterions by multivalent counterions in a PE brush layer [159]. Accordingly, a greater number of monovalent counterions prefer to remain in the bulk with the multivalent counterions remaining within the brush layer and solvating the PE chains. This entropic argument is also used to discuss (qualitatively and quantitively) the cases of other systems [160] where ion condensation on PE chains is important: for example, entropic contribution is found to dictate the ion condensation in cationic and anionic chains in a PE melt and can lead to the formation of coacervates [161].

We have also tried to quantify the inequality in the number density of counterions and coions by plotting the net charge (Δe) in the brush free bulk (figure 5.3(b)). This net charge is normalized by number of added coion in the salt. We can see that, except for Cs^+, the net charge in the brush free bulk is negative for all ions considered here. Negative charges in the brush free bulk tells us that there are more coion in the bulk than counterions. As the total system is charge neutral, it also means that there are more counterions inside the brush layer than it needed to neutralize negative PE charges. This phenomenon is called as overscreening (OS). Our simulation, therefore, suggests that there will be OS in a PAA brush grafted nanochannel for Na^+, Ca^{2+}, Ba^{2+}, and Y^{3+} ions We are clearly not seeing any OS for Cs^+. These differences in the charges can also be visualized from the insets of figure 5.2.

We can see that Cs^+ is showing large $|\Delta e/n_{salt}|$ compared to other ions. From figure 5.3(a), we know that Cs^+ has the highest number density in the bulk, so the high $|\Delta e/n_{salt}|$ is coming from a large number of ions. On the other hand, the number density is very low in the bulk for multivalent ions; this implies that OS inside the PE brush layer is triggered by only a small number of ions present in the bulk. For multivalent ions, the bulk is composed of higher ratio of coion to

counterion number which is enough to create significant overscreening effect. In fact, there are almost no Y^{3+} counterion in the bulk (figure 5.2 (e)) and the number of Ca^{2+} is also very low in the bulk (figure 5.2 (c)).

Na^{+}, Ca^{2+}, Ba^{2+}, and Y^{3+} are highly attracted to charged PAA monomers and they get fully condensed to the O of the monomer [see Chapter 3]. This condensation to the PE can be thought similar to the formation of Stern layer; layer of counterions trying to neutralize the surface charges. When the charge density is high (high valance, smaller size), counterions can overcompensate the initial surface charge, or for our case, PE brush charge. On the other hand, Cs^{+} ion doesn't condense to the PE monomer fully and a large portion of the Cs^{+} ions can neutralize the PE monomers by having them in the second solvation shell. Neutralizing by second solvation shell means that a large portion of the Cs^{+} counterions don't stay inside the brush layer and they remain in the brush free bulk. This excess Cs^{+} ion overwhelm the number of added Cl^{-} in the bulk, which means no overscreening for the case of PE brushes being screened by the Cs^{+} counterion and having CsCl as the added salt.

Electroosmotic flow in a PE brush grafted nanochannel

Simulation systems remain almost similar to the previous section. Instead of 25, 60 chains are grafted in one layer of the nanochannel in a 12×5 (X × Y) array as shown in figure 5.4. We have applied electric fields of strengths 0.1 and 1 V/nm in the axial (or X) direction. When an electric field $\boldsymbol{E}$ is applied to the system, a force of $q_i\boldsymbol{E}$ acts on the atom i having a charge of q_i. Further details about the simulation have been provided in the Methods section.

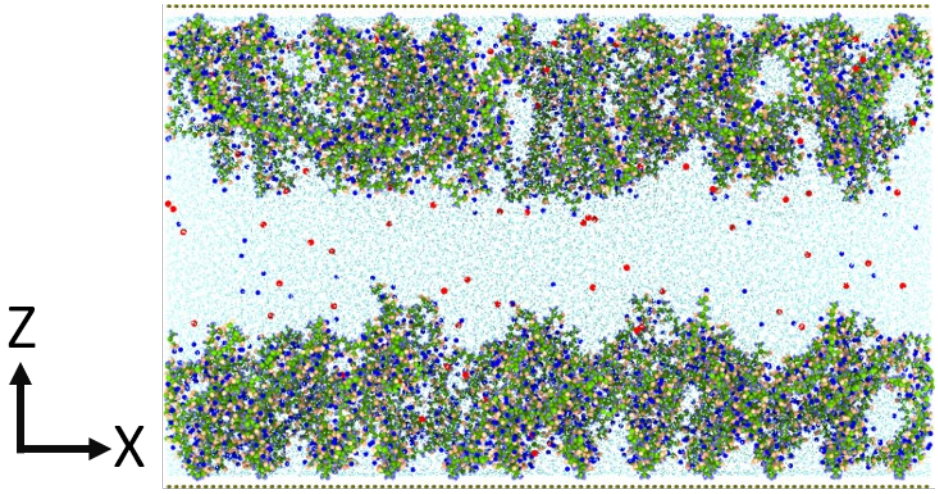

Figure 5.4: Snapshot of the simulation system (shown here for Na^+). Blue circles are the counterions and reds are coion. Other circles are atoms of PE. Green small dots indicate water.

We started our analysis by looking into the ion distributions inside the nanochannel. The average number density of ions in the bulk (averaged over coions and counterions) is shown in figure 5.5 (a). The number density in equilibrium remains similar to that of the previous section (figure 5.3 (a)); increasing valence and decreasing size of the counterion reduces the ion number density in the bulk. Interestingly, when an axial electric field is applied, ion density in the brush-free bulk increases. The application of an electric field decreases the PE brush height inside the nanochannel (shown in chapters 2 and 4). This reduction of the brush height squeezes out the ions from inside the brush layer to the brush-free bulk: this leads to higher ion density in the bulk. Ion-specific interactions (like we discussed in chapter 2: ion-monomer dipole under external electric field, etc.) can also influence the overall density change in the bulk by controlling how many counterions are able to leave the counterion-monomer complex.

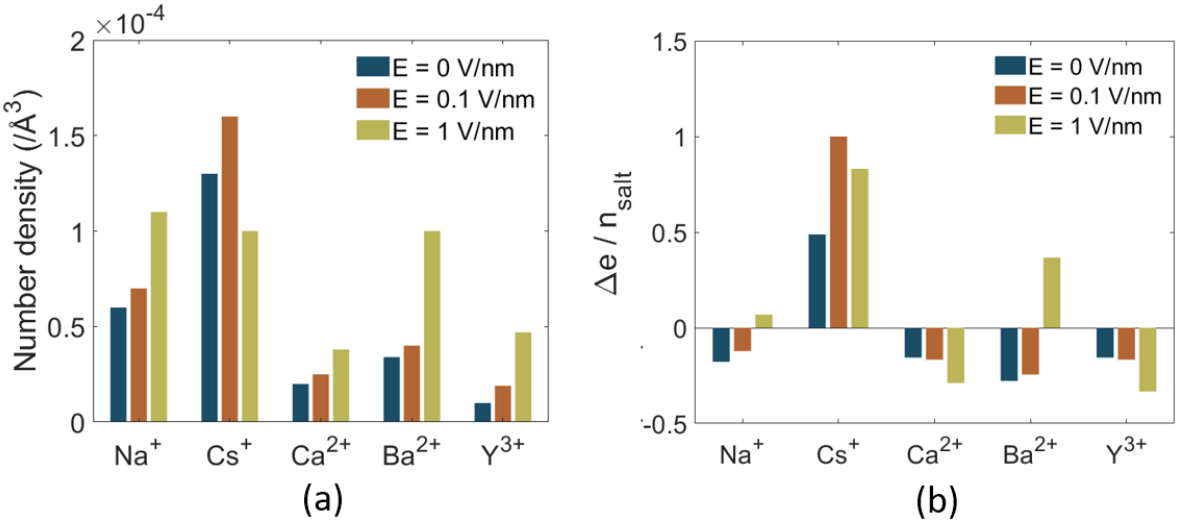

Figure 5.5: (a) Average number density of ion in the brush free bulk. (b) Difference in charges (normalized by the number of Cl^- ions present in the system), $\frac{\Delta e}{n_{salt}}$, in the brush free bulk layer. A negative value of $\frac{\Delta e}{n_{salt}}$ indicates the occurrence of overscreening.

We have quantified the inequality in the number density of counterion and coion, as a function of the applied electric field, by plotting the net charge (Δe) in the brush-free bulk (figure 5.5(b)). This net charge is normalized by the number of added coion in the salt. Similar to section 5.2.1, we are seeing overscreening for Na^+, Ca^{2+}, Ba^{2+}, and Y^{3+} ions (particularly for small electric field strength of 0.1 V/nm) and no overscreening for Cs^+. However, for a larger electric field (E=1 V/nm), the OS disappears and Δe becomes positive for Na^+ and Ba^{2+} ions. It is also elucidated that $\Delta e/n_{salt}$ increases for the case of Na^+, Cs^+, and Ba^{2+} ions with the application of applied electric field. This indicates that more counterions are going to the brush-free bulk than coions. On the other hand, $\Delta e/n_{salt}$ decreases for Ca^{2+}, Y^{3+}; more coions are released from the brush layer than counterion. These two types of behavior can be discussed from the electrostatic interaction perspective. Ca^{2+}, Y^{3+} show the strongest attachment to the PE monomers because of their high valence and smaller size. As they are very strongly attached to the PE monomer, even the strongest

possible applied electric fields are not strong enough to disrupt their strong attachment. Because of this, we do not see much Ca^{2+}, Y^{3+} ions leaving the brush layer. Instead, a few coions leave the brush layer and go to the bulk, which eventually decreases the $\Delta e/n_{salt}$.

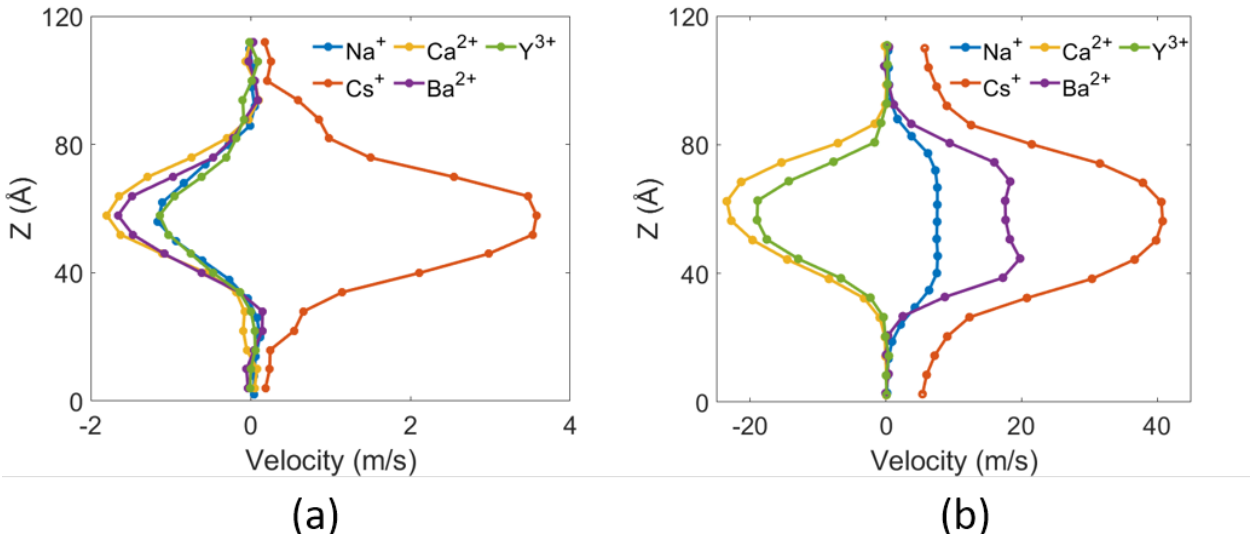

Figure 5.6: Velocity of the water (solvent) molecules along the system height for (a) E = 0.1 V/nm and (b) E = 1 V/nm.

Along with changing the ion distributions inside the nanochannel, the electric field also introduces an electroosmotic (EOS) flow. We have plotted the EOS velocity inside the nanochannel in figure 5.6. We can see that the EOS flow follows the trend in the ion distribution in the brush-free bulk. EOS is coion-dominated for Na^+, Ca^{2+}, Ba^{2+}, and Y^{3+} ions and counterion dominated for Cs^+ when the applied electric field is 0.1 V/nm. Na^+, Ca^{2+}, Ba^{2+}, and Y^{3+} shows overscreening in this electric field. As the numbers of coions are higher in the bulk for these simulations; more waters will be present in the solvation shells of coions. As coions move in the opposite directions to the applied electric field, the solution will also move in the opposite to the electric field direction. The opposite is true for Cs^+ ion: a higher number of Cs^+ makes flow in the same direction as the applied electric field. When the electric field is changed from 0.1 to 1 V/nm,

the flow direction for Na^+ and Ba^{2+} changes from coion-dominated to counterion-dominated, since the OS disappears at this electric field strength for these two types of counterions [see Fig. 5.5(b)]. As the number of counterions increases in the bulk, the solutions follow the direction of counterions. As no such ion distribution alteration is observed for Ca^{2+} and Y^{3+}, flow is still in the direction opposite to the applied electric field.

Finally, the velocity is almost zero inside the brush layer for Na^+, Ca^{2+}, Ba^{2+}, and Y^{3+}. A finite velocity is observed inside the brush layer only for Cs^+. We have seen in chapter 3, Cs^+ is not fully condensed in the PE chain. As a portion of Cs^+ is not strongly condensed (on the PE brush layer) and is able to move relatively freely, they can respond to the applied electric field independently (i.e., without following the behavior of the PE brushes). This independent motion of the Cs^+ ions introduces a finite velocity even inside the brush layer. On the other hand, other counterions are strongly bound to the PE monomer: as they cannot move independently inside the brush layer, the flow is almost negligible inside the brush layer.

We have calculated the free energy of counterion binding to PE monomers: such free energy calculations can provide valuable information about ion distributions and their modifications under applied electric field. Umbrella sampling is used to calculate the free energy of counterion binding to PE monomer. A PE chain with 6 monomers is grafted to a surface: the PE chain is neutralized by different counterions (please see a partial snapshot of the system in figure 5.7). We have selected a monomer and a counterion condensed on the corresponding monomer. We kept the backbone carbon atom of the monomer fixed in its position and moved the counterion away from it. The free energy curves are provided in figure 5.7. Y^{3+} ion shows the highest energy penalty to leave the PE chain: in other words, Y^{3+} ion shows the maximum energy favorability in its condensed state (on the PE backbone). Ca^{2+} ion also shows a larger free energy

favorability (as compared to Na^+, Cs^+, and Ba^{2+} ions) in remaining condensed on the PE backbone. This free energy curves support the findings reported in Fig. 5.5(b): the large energy favorability of the Y^{3+} and Ca^{2+} ions in remaining condensed on the PE backbone implies that the applied electric field is not sufficient to make the Y^{3+} and Ca^{2+} ions to leave the PE, and therefore, there is no electric-field-driven reversal of the overscreening behavior for the case of PE brushes screened by Ca^{2+} and Y^{3+} ions.

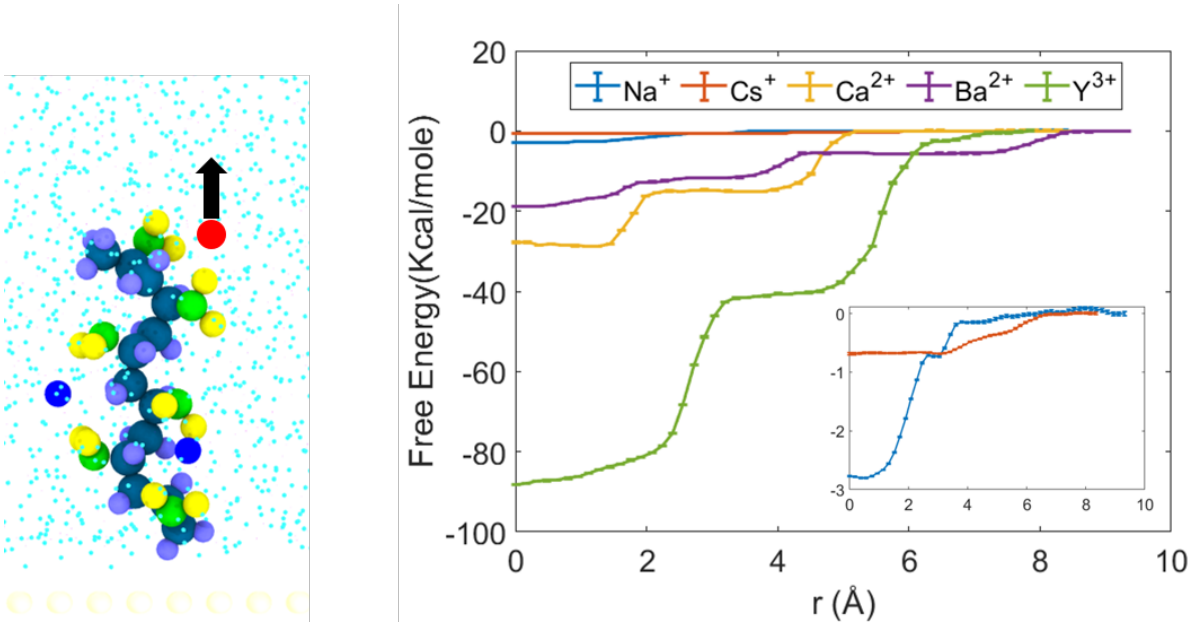

Figure 5.7: (Left) Snapshot of the simulation system used in free energy calculation. Blue circles show counterions (this particular system is for Ca^{2+}), red circle is the counterion which is displaced to perform the umbrella sampling. (Right) Calculated free energy as a function of the counterion reaction coordinate for different counterions.

5.3 Methods

We simulate fully charged Polyacrylic acid (PAA) chains grafted in two opposing layers. Different counterions, namely Na^+, Cs^+, Ca^{2+}, Ba^{2+}, Y^{3+} are separately considered (as screening counterions) to neutralize the polyelectrolyte (PE) segmental charge in a solvent of explicit SPC/E

water [67]. In addition, we add 0.1 M Chloride salt in the system. PE chains are grafted with a grafting density of $0.05/\sigma^2$ (σ=3.5 Å, is the LJ distance parameter of backbone carbon atoms). This grafting density of PAA chains is within the range of experimentally reported [60] grafting densities. Each chain has 49 backbone carbon atoms. Purely repulsive walls are placed at the top and the bottom of the system to prevent the mobile atoms from escaping the system. The particle trajectories are calculated using the Velocity-Verlet algorithm, with a time step of 2 fs. Non-bonded interactions were modelled as the sum of a shifted-truncated 12-6 Lennard Jones potential (U_{LJ}) with a cut-off distance of 13Å. To calculate the long-range Columbic interactions, PPPM (particle-particle particle-mesh) algorithm [68] is used. The bonds and angles of water molecules are conserved with the help of the SHAKE algorithm [69]. Periodic boundary conditions are applied in x and y directions, while the fixed boundary condition is incorporated in z direction. Simulations are performed in LAMMPS [70] and OVITO is used to visualize the simulation system [71].

Counterions, coions and waters are randomly distributed in the system. After creating the initial configuration, the systems are first run in the NP_zT ensemble (the subscript Z means that only the system height in Z direction is allowed to change) to obtain the correct simulation box heights at 300 K and 1 atm with the help of Nosé-Hoover thermostat and barostat [79,80]. Subsequently, the systems are equilibrated in the NVT ensemble to obtain the correct equilibrium configuration by incorporating the Langevin thermostat [81]. Each simulation is performed until the brush height starts fluctuating around a constant value. After equilibration, we performed the production run for 20ns. We also checked the autocorrelation function of the end point of PE chains in the production period: the autocorrelation function started fluctuating around zero very quickly which indicates proper statistical sampling in total 20ns production run [figure 5.7].

We have used OPLS-AA force field [72] to model the interaction parameters for the PAA chains. The bonded and non-bonded parameters for the PAA chains were taken from the OPLS database. The Lennard Jones (LJ) parameters for the monovalent counterions were taken from Joung and Cheathan [73]. Parameters for multivalent counterions were employed from Li *et al.* [113,114]. These parameters are very accurate for monovalent and multivalent ions in an aqueous system.

In this production period, the brush height fluctuates around a constant value, confirming the attainment of equilibrium. This production period is considered to be 20 ns for the simulations for all cases of counterions both in absence and presence of the added salt (see Table 5.1). We also checked the autocorrelation function of the end point of PE chains in this production run. The autocorrelation function for a variable Y is given by $C_Y(t) = \frac{(<Y(t)-\langle Y\rangle)(Y(0)-\langle Y\rangle>)}{<Y^2>-<Y>^2}$, where $\langle Y\rangle$ denotes the mean value of Y. We plot the autocorrelation function for average end-point brush height $C_e(t)$ corresponding to the cases of different screening counterions in Figure 5.8. Given autocorrelations are shown for the simulation performed for section 5.2.1.

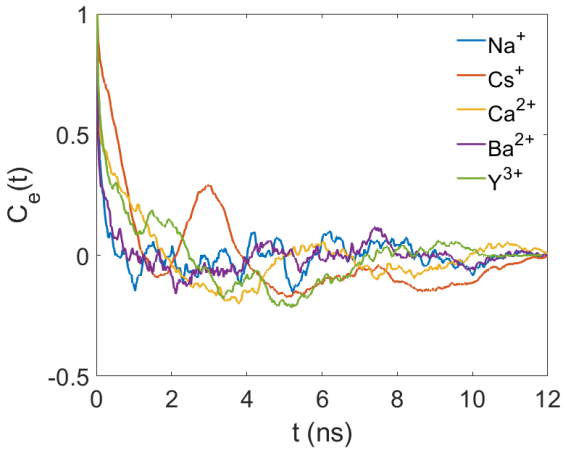

Figure 5.8: Autocorrelation function of the end point of PE chains for different simulations.

Same procedure is followed for the simulations of electroosmotic flow also. After initial

equilibration, we have applied the electric field under the NVT ensemble to remove the heat dissipated due to the flow. Only polymers are thermostatted in the entire system, this mimics the experimental scenario where temperature can be controlled form the outer surface. Each non-equilibrium simulation is performed again until the brush height starts fluctuating around a new modified value. After equilibration, we performed the production run for 20ns.

To calculate free energy calculations in our main simulation setup a condensed counterion have been chosen. This ion is pulled out from the chain to the bulk by specifying the reaction coordinate in Z direction that varies by 0.5 Å in every successive reaction coordinate. These ions were constrained to their windows by a harmonic potential with spring constant. Generally, all these simulations lasted for 4 ns and the data collected from the last 3 ns was used for analysis. We have checked the probability near reaction coordinates and ensured than every possible position is sampled. The axial positions of the sample molecules were outputted every 20 fs and the weighted histogram analysis method (WHAM) [151, 152] was used to analyze the data generated from umbrella sampling.

The Lennard-Jones (LJ) potential (U_{LJ}) used in the simulations is expressed as:

$$U_{LJ} = 4\epsilon_{ij}\left[\left(\frac{\sigma_{ij}}{r_{ij}}\right)^{12} - \left(\frac{\sigma_{ij}}{r_{ij}}\right)^{6}\right], \quad (5.1)$$

while the Coulombic pairwise interaction (U_{Coul}) used in the simulation is expressed as:

$$U_{Coul} = \frac{q_i q_j}{4\pi\epsilon_0\epsilon_1 r_{ij}}. \quad (5.2)$$

In these equations, ϵ_{ij} is the depth of the LJ potential well between atoms i and j, σ_{ij} is the distance between atoms i and j, q_i and q_j are charges of the i^{th} and j^{th} atoms, r_{ij} is the distance between atoms i and j, $\in_0$ is the permittivity of vacuum and $\in_1$ the relative permittivity of the background

(taken to be 1). Geometric mixing rules were used for calculating the LJ interactions between the different atom types. For mobile-ion-mobile-ion and mobile-ion-water interactions, we used the Lorentz-Berthelot mixing rules to be consistent with Joung et al. [73] and Li et al. [113,114].

In Fig. 5.9, we have provided a schematic representation of the fully ionized Polyacrylic acid molecule. Parameters required for eqs. 5.1 and 5.2 for atom mentioned in figure 5.8 is shown

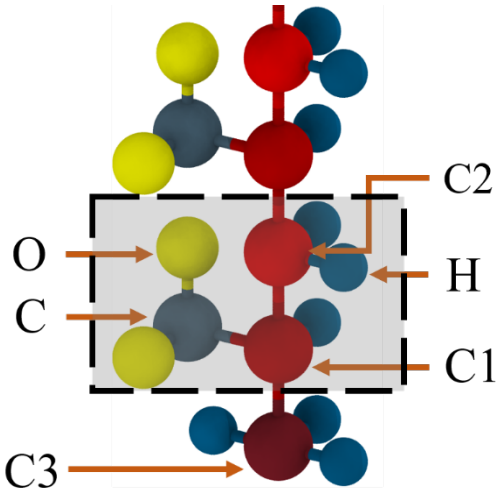

Figure 5.9. A partial schematic representation of the fully ionized PAA molecule. Different atom types are indicated with arrows. Polyelectrolyte's (PE's) repeating unit is indicated with the shaded box.

in Table 5.1.

Atom Type	**Charge** (e)	**Mass** (amu)	$\epsilon\ (Kcal/mole)$	σ (Å)
C3 (CH_3)	-0.18	12.011	0.066	3.50
C2 (CH_2)	-0.12	12.011	0.066	3.50
C1 (CH, Attached to COO-)	-0.16	12.011	0.066	3.50
C (COO-)	0.70	12.011	0.105	3.75
H	0.06	1.008	0.03	2.50
O (COO-)	-0.80	15.999	0.210	2.96
O_w (H_2O)	-0.8476	15.999	0.155354	3.166
H_w (H_2O)	0.4238	1.008	0	0
Na	1.00	22.99	0.3526418	2.1595

Cs	1.00	132.9	0.0898565	3.6010
Ca	2.00	40.078	0.04560206	2.7083
Ba	2.00	137.327	0.23380842	3.2518
Y	3.00	88.906	0.02759	2.5996
Cl	-1.00	35.453	0.012785	4.83
Continuous LJ Wall (Parameters remain unchanged for interaction with all atom types)	0.00	15.00794	0.1947	3.00 (LJ cut off length is 3.36 Å)

Table 5.1: Charge, mass and LJ parameters for all the different atom types

Harmonic bond style is used to calculate the potential energy for bond:

$$U_{bond} = K_b(r - r_0)^2. \qquad (5.3)$$

Here, r_0 is the equilibrium bond length and K_b is bond stiffness. The values for r_0 and K_b for all bond types are provided in Table 5.2.

Bond Type	$K_b, (\frac{Kcal}{mol.Å^2})$	$r_0, (Å)$
C2-H	340.0	1.09
C2-C1	268.0	1.529
C1-H	340.0	1.09
C3-H	340.0	1.09
C-C1	317.0	1.522
C1-C3	268.0	1.529
C-O	656.0	1.25
O_w-H_w	-	1.00

Table 5.2: Bond parameters used in the simulations

The potential energy for the finite angle between different bonds is calculated using the

following harmonic equation:

$$U_{angle} = K_a(\theta - \theta_0)^2. \qquad (5.4)$$

Here, θ_0 is the equilibrium value of the angle and K_a is the angle stiffness. The values for θ_0 and K_a for different angles are provided in Table 5.3.

Angle Type	$K_a, (\frac{Kcal}{mol.rad^2})$	$\theta_0(deg)$
H-C2-H	33.00	107.8
H-C2-C1	37.5	110.7
C2-C1-H	37.5	110.7
C1-C3-H	37.5	110.7
H-C3-H	33.00	107.8
H-C1-C	35.0	109.5
O-C-O	80.0	126.00
C2-C1-C	63.0	111.1
C3-C1-C	63.0	111.1
H_w-O_w-H_w	-	109.47
C2-C1-C2	58.35	112.7
C2-C1-C3	58.35	112.7
C1-C-O	70.0	117.0
C3-C1-H	37.5	110.7
C1-C2-C1	58.35	112.7

Table 5.3: Angle parameters used in the simulations

The potential energy associated with the 4-atom dihedral torsion interactions is given by

$$U_{dihedral} = \frac{1}{2}K_1[1 + cos(\emptyset)] + \frac{1}{2}K_2[1 - cos(2\emptyset)] + \frac{1}{2}K_3[1 + cos(3\emptyset)] + \frac{1}{2}K_4[1 - cos(4\emptyset)]. \qquad (5.5)$$

Here, K_1, K_2, K_3, and K_4 are the four Fourier coefficients for torsional interactions, and $\emptyset$ is the torsional angle. Values of K_1, K_2, K_3, and K_4 are provided in Table 5.4.

Dihedral type	K_1, $(Kcal/mole)$	K_2, $(Kcal/mole)$	K_3, $(Kcal/mole)$	K_4, $(Kcal/mole)$
H-C2-C1-H	0.0	0.0	0.30	0.0
H-C2-C1-C	0.0	0.0	-0.10	0.0
H-C2-C1-C2	0.0	0.0	0.30	0.0
H-C2-C1-C3	0.0	0.0	0.30	0.0
H-C1-C-O	0.0	0.0	0.00	0.0
H-C1-C3-H	0.0	0.0	0.30	0.0
C2-C1-C-O	0.0	0.82	0.00	0.0
C2-C1-C2-C1	1.30	-0.05	0.20	0.0
H-C3-C1-C2	0.0	0.0	0.30	0.0
C3-C1-C-O	0.0	0.82	0. 0	0.0
C1-C2-C1-C	-3.185	-0.825	0.493	0.0
C1-C2-C1-C3	1.30	-0.05	0.20	0.0
H-C1-C2-C1	0.0	0.0	0.30	0.0
H-C3-C1-C	0.0	0.0	-0.10	0.0

Table 5.4: Dihedral parameters used in the simulations

The potential energy associated with the improper torsional dihedrals are modelled using the harmonic function:

$$U_{improper} = K_i(\varphi - \varphi_0)^2. \quad (5.6)$$

Here, φ_0 represents the equilibrium value of the improper torsional angle and K_i is the improper torsional stiffness. Their values for the C1-O-C-O system is provided in Table 5.5.

Improper Type	$\boldsymbol{K_i}\ (\frac{Kcal}{mol.rad^2})$	$\varphi_0(deg)$
C1-O-C-O	10.5	180

Table 5.5: Improper dihedral parameters used in the simulations

5.4 Conclusion:

In this chapter, we show how ions are distributed in a polyelectrolyte brush grafted nanochannel by using all-atom molecular simulation. We consider Na^+, Cs^+, Ca^{2+}, Ba^{2+}, Y^{3+} counterions and found a clear trend of ion density in the bulk between two layers of PE with counterion size and valence. Counterion with higher valance and smaller size prefer to stay inside the PE brush layer more, so a depletion of ions in the bulk is observed. We also see overscreening is happening in the nanochannel except for Cs^+. Incomplete condensation of Cs^+ in the PE chains explains this behavior. This overscreening for Na^+, Ca^{2+}, Ba^{2+}, and Y^{3+} counterions manifest a coion-dominated electroosmotic flow in 0.1 V/nm electric field. High electric field of 1 V/nm diminishes the overscreening for Na^+ and Ba^{2+}, as a result, counterion-dominated electroosmotic flow is observed. No such alteration of ion distribution is observed for Ca^{2+}, Y^{3+} counterions because of stronger electrostatic interaction between PE monomer and Ca^{2+}, Y^{3+} counterions. So, we discover that flow is always coion-dominated for Ca^{2+}, Y^{3+} counterions.

Chapter 6: Conclusion and Future Scope

In this dissertation we employ atomistic simulations to study how polyelectrolyte brushes respond to two most important stimuli; (a) type of counterions that screen the charges of the PE brushes and (b) external electric fields. We also elucidate how these responses can modify ion distribution around polyelectrolytes and as a result, electroosmotic flow in nanochannels grafted with such brushes. In this chapter, we discuss the major contribution of this work to the existing body of knowledge.

- Probe how axial electric field changes the conformation of a PE brush layer. We find the critical role of the PE monomer's charge density (more specifically the strength of the monomer-counterion complex) in dictating the bending or tilting mediated brush height reduction in presence of the applied electric field. Condensation of counterions to PE chains (for the case when the charge density of the PE monomer is high) limits the independent movement of the PE chains or counterions, resulting in a bending of the PE chains. On the other hand, mutually independent responses of the PE monomer and the counterions (for the case when the charge density of the PE monomer is small) ensure the tilting of the PE brushes opposite to the applied electric field. This newly found understanding of PE brushes response to axial electric field can be very useful for explaining previously observed results in PE grafted systems.
- Simulate the PE brushes neutralized with counterions of different valences and sizes. We found that bridging of two or more negative monomers, mediated by counterions, is not a sole function of the counterion valence; rather it is combination of the counterion size and valence. We study how counterion condensation to the PE chain, possibility of firm second solvation shell, and solvation shell size affect the bridging interactions. We also discuss

how these bridging interactions behave dynamically. This study, therefore, refines the generally perceived notion of valence dependent bridging interaction and brings counterion size in the limelight.

- How grafted PE brush control ion distribution inside a nanochannel, how electric field changes the ion distribution, how electroosmotic flow behaves near PE brush? We answer these questions in chapter 4. We find PE brushes neutralized with Sodium ions can introduce overscreening inside the nanochannel and electric field can modify this ion distribution by controlling the brush height, and counterion-monomer interaction. Electrostatic flow direction reversal from coion-dominated to counterion-dominated can be achieved by merely changing the electric field strength. We discuss the effect of the time of water residence in the ion solvation shell and the electrophoretic mobility of ions in governing the overall electroosmotic flow. This study presents new understanding in the theory of overscreening and electroosmotic flow in PE-brush-functionalized nanochannels.
- Probe the distribution of ions in a PE brush grafted nanochannel where counterions of different valence and sizes neutralize the PE charges. We found that smaller counterions with high valence prefer to stay inside the PE brush layer more than the counterions of larger size and smaller valence. Proper condensation of counterion to the PE chains helps to introduce overscreening in the nanochannel. We also find that the applied electric field can alter the overscreening behavior inside the nanochannel if it can break the effect of the monomer-counterion interaction. Various ion distributions associated with different counterions eventually lead to a broad range of electroosmotic flow behavior.

Most importantly, this dissertation shows the importance of accounting of the chemical details for understanding the behavior of the PE brush systems. So far, coarse-grained simulations, along

with theoretical calculations, have served as the main tool to understand the PE brush grafted system. Throughout this thesis, we show the importance of accounting for the chemical details of PE monomer, ions, water, monomer-ion solvation structure, ion dynamics, charges, and sizes of different atoms. Consideration of these granular details can help to unravel novel and intriguing scientific phenomena, which help to move forward overall soft matter research.

Finally, this dissertation raises important questions and shows future directions. New ideas and understandings obtained from this dissertation can transfer to other soft charged systems. One can expect systems such as polyelectrolyte gels, coacervates, etc. to demonstrate interesting ion dependent behaviors (for situations where granular chemical details of the different components of the system are been accounted for) and this thesis can be a good guide for initiating such research. Secondly, pH of the solution can control different aspects of a PE brush grafted system; for example, it can control the charge density in the PE by controlling degree of ionization. Understanding the effect of solution pH can be very helpful for greater atomistic quantifications. Third, the study of positively charged or cationic brushes (this thesis has only considered anionic brushes), which can introduce diverse PE-water interactions and PE-counterion solvation structures, and can responds to perturbations differently, can be a topic of significant interest. Fourth, our thesis can serve as the foundational basis for probing in an all-atom framework the behavior of poly-zwitterionic PEs which consists of a combination of an anionic and a cationic group (and therefore is expected to manifest a myriad of different ion condensation and bridging behaviors). Finally, the different fundamental analyses conduced in our thesis point to the possibilities where an all-atom understanding of the behavior of PE brushes can be leveraged to design devices with better lubrications, energy generation, motion control capabilities.

Appendix A

Effect of the added salt in the electric-field-response of the PE brushes

In chapter 2, we have made the following inference: *in presence of the applied axial electric field, the counterion distribution around an oxygen of a respective monomer ($O_{Carboxylate}$ or $O_{Sulfonate}$) of the PE dictates the conformation of the PE layer.* Given that the brush conformation is a result of this local arrangement of ions, instead of global, the effect of salt concentration (on the brush configuration) should be minimal as long as the majority of the salts ions remain within the brush-free bulk.

Here we provide simulation results that attempt to investigate what happens to the salt ions in presence and in absence of the applied axial electric field and in the process attempts to test the above idea (i.e., *majority of the salts ions remain within the brush-free bulk*). In our simulations, we have 864 counterions (Na^+ ions) to neutralize the anionic brush (for the case of PAA brushes). We have also added 0.2M NaCl salt which corresponds to 170 Na^+ and 170 Cl^- ions. In Fig. A1 we present the ion distributions in the simulation system. Fig. A1(a) shows that there are very few Cl^- ions inside the brush layer both in the presence and in the absence of the applied electric field. In Fig. A1(b), we quantify the variation of the net charges (Δ_q) for the entire domain (for this purpose, we also account for the local charges of the PE brush molecules), i.e., both inside the brush layer and inside the brush-free bulk. *We find nearly perfect electroneutrality in the brush-free bulk both in presence and in absence of the applied electric field.* There are as many as 170 Na^+ and 170 Cl^- ions from the salt and we find $\Delta_q \approx 3$ in the bulk (confirming this near perfect electroneutrality) in presence of the applied electric field. Given that almost all of the Cl^- ions from the salt is within the brush-free bulk, this near electroneutrality in the brush-free bulk implies that almost all the Na^+ ions added from the salt must also remain within the brush-free bulk (i.e., these

Na^+ ions from the salt will rarely enter the brush layer either in presence or in absence of the electric field). *Therefore, we can infer that given that the majority of the salt ions remain within the brush-free bulk and do not enter the PE brush layer, the salt concentration will have insignificant effect in determining the configuration of the PE brush molecules in the presence of the applied electric field.*

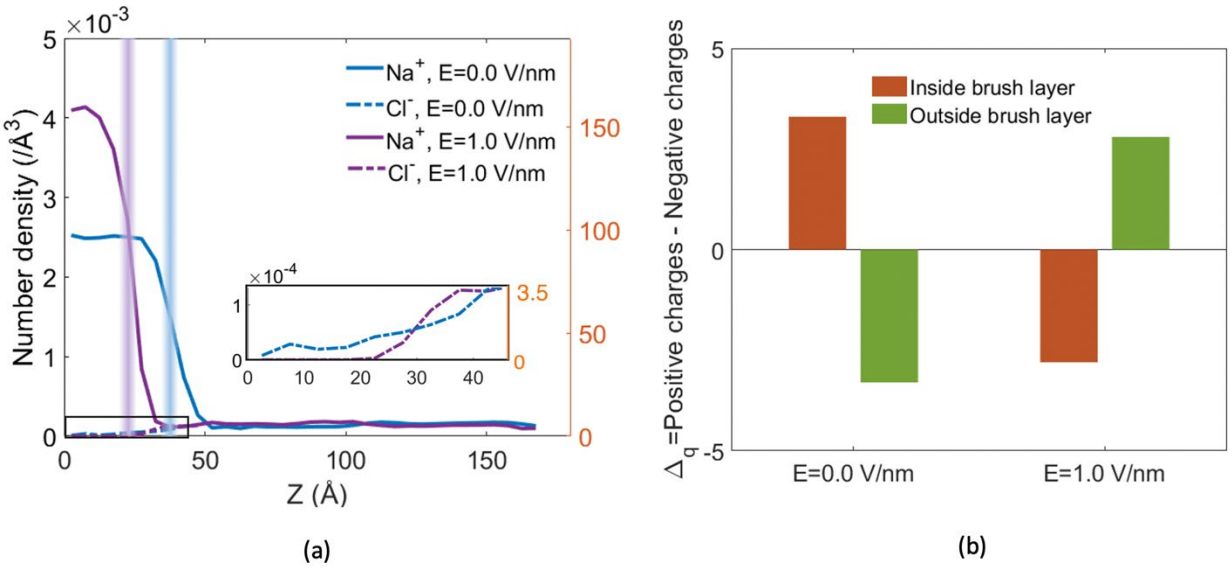

Figure A1: (a) Mobile ion distribution along simulation box height. Left axis shows the number density and right axis shows number of ions in a slab of 5 Å along the Z axis in the simulation box. Number densities as well as the total number of Cl^- ions inside and near the brush layer are zoomed in the inset. The inset axes have the same units as main figure. (b) Variation of the net charge $\Delta_q =$ $\boldsymbol{Total\ number\ of\ postive\ charges - Total\ number\ of\ negative\ charges}$ inside and outside the PE brush layer. In consideration of the total number of charges, we account for the charges of the PE brushes, counterions, and salt ions. Perfect electroneutrality would imply $\Delta_q = \mathbf{0}$. Both the figures provide the results for the PAA brushes. Shaded vertical lines in part (a) indicate the average brush height.

Appendix B

Some important supporting information related to chapter 3 is presented here.

Ion distribution properties

As mentioned in the chapter 3, we have used the first valley of the $O_{Carboxylate}$-counterion radial distribution function (RDF) as the cutoff value for the bridging. Here we are presenting these RDF for different counterions.

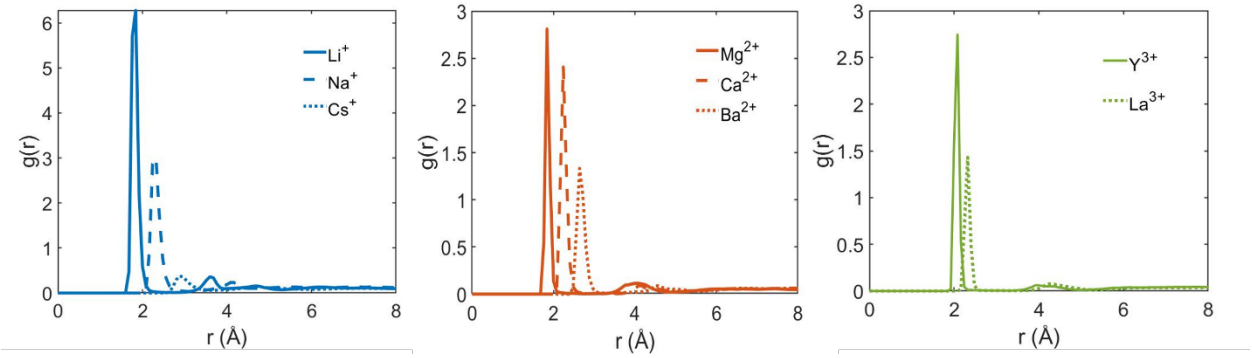

Figure B.1: $O_{Carboxylate}$-counterion radial distribution function (RDF)

We have discussed in the main chapter first peaks in the probability density distribution (ρ(r)) follows the LJ size of the respective counterions. Here we are tabulating the values of the locations of first peak in ρ(r) and the LJ size of each counterions.

Counterion type	First peak in ρ(r)	LJ radius
Li^+	1.84	1.4094
Na^+	2.3	2.1595
Cs^+	2.88	3.6010
Mg^{2+}	1.84	2.294955
Ca^{2+}	2.24	2.7083
Ba^{2+}	2.64	3.2518
Y^{3+}	2.08	2.5996

La^{3+}	2.32	2.903

Table B.1: First peak in ρ(r) and size of different counterions (all in Angstrom)

Persistence length:

We have used worm like chain (WLC) model to calculate the persistence lengths of the PE molecules in the "brush"-like state. According to the WLC model [162]

$$\langle R^2 \rangle = 2PL\left[1 - \frac{P}{L\left(1-e^{-\frac{L}{P}}\right)}\right]. \quad \text{(B.1)}$$

Where $\langle R^2 \rangle$ is the average of end-to-end distances if the PE chains over the production period, P is the persistence length, and L is the contour length.

The persistence lengths for the PE brushes for different simulations corresponding to the different screening counterions in presence and in absence of the added salt are tabulated in table B.2.

Counterion Type	P (Å), without salt	P (Å), with salt
Li^+	14.5	13.1
Na^+	14.3	12.4
Cs^+	14.2	12.9
Mg^{2+}	15.3	15.5
Ca^{2+}	15.5	15.71
Ba^{2+}	14.15	14.01
Y^{3+}	12.8	11.8
La^{3+}	15.2	15.01

Table B.2: The persistence lengths of the PE brushes in the presence of the different counterions without and with the added salt (0.4 M concentration of the chloride of the corresponding counterions) for different simulations

Polarizability:

To check the effect of polarizability, we have performed a simulation with Y^{3+} counterion using 12-6-4 lj parameter [114]. In figure B.2 we show the brush height, interchain bridging and CDF.

	12-6	12-6-4
Brush height	36 Å	37.5 Å
Interchain Bridging	0.13	0.17

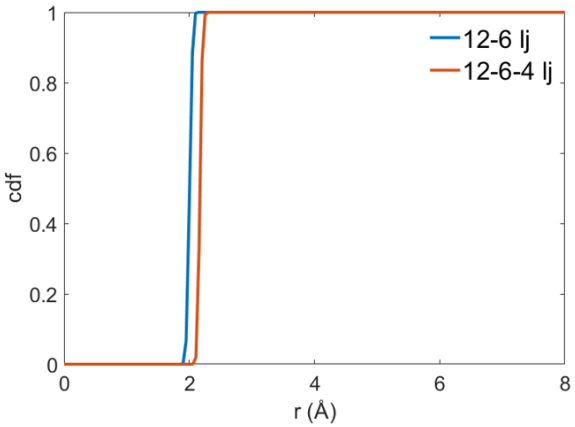

Figure B.2: Effect of polarizability of Y^{3+} counterion.

Appendix C

In this appendix, few important results and discussion related to chapter 4 is discussed.

Brush properties:

In Figure C.1(A), we have plotted the transverse backbone carbon distributions as a function of the applied electric field. These distributions are analogous to the monomer distribution profile. This figure elucidates the reduction in brush height and the increase in monomer density with an enhancement in the strength of the applied electric field. Average brush profiles are shown in Figure C.1(B). This plot shows that as there is a very small flow inside the brush layer, which creates a negligible drag, and hence there is no significance tilt along the electric field. Other than tilting in a particular direction, brushes become sparse along x direction, which is depicted in

chapter 5.

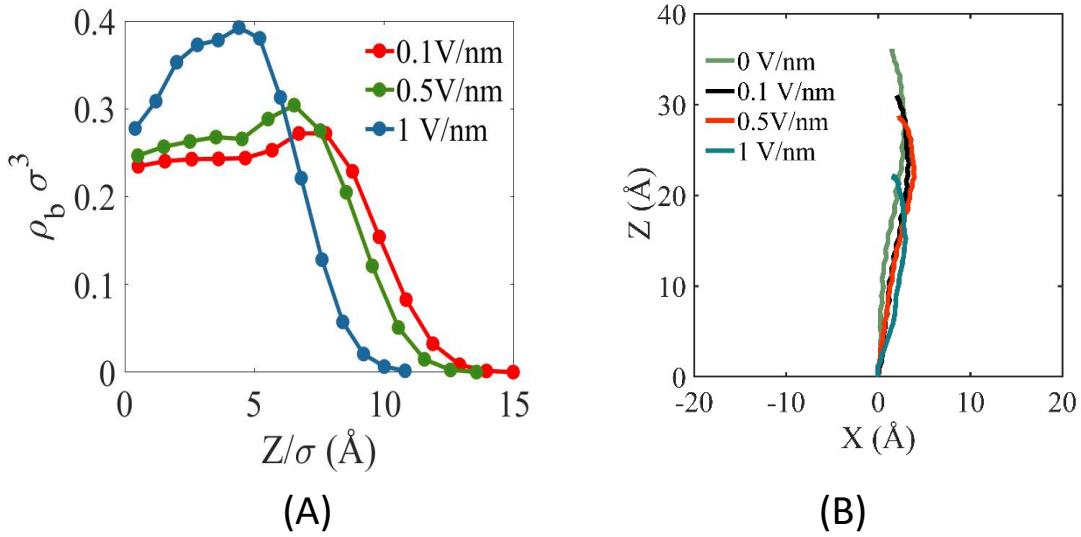

Figure C.1: Brush behavior in different electric field. (A) Backbone carbon distribution profiles with different applied electric field. $\boldsymbol{\rho}_b\sigma^3$ is the normalized number density of backbone carbon. (B) Average backbone carbon profile of the brush under different electric field strengths.

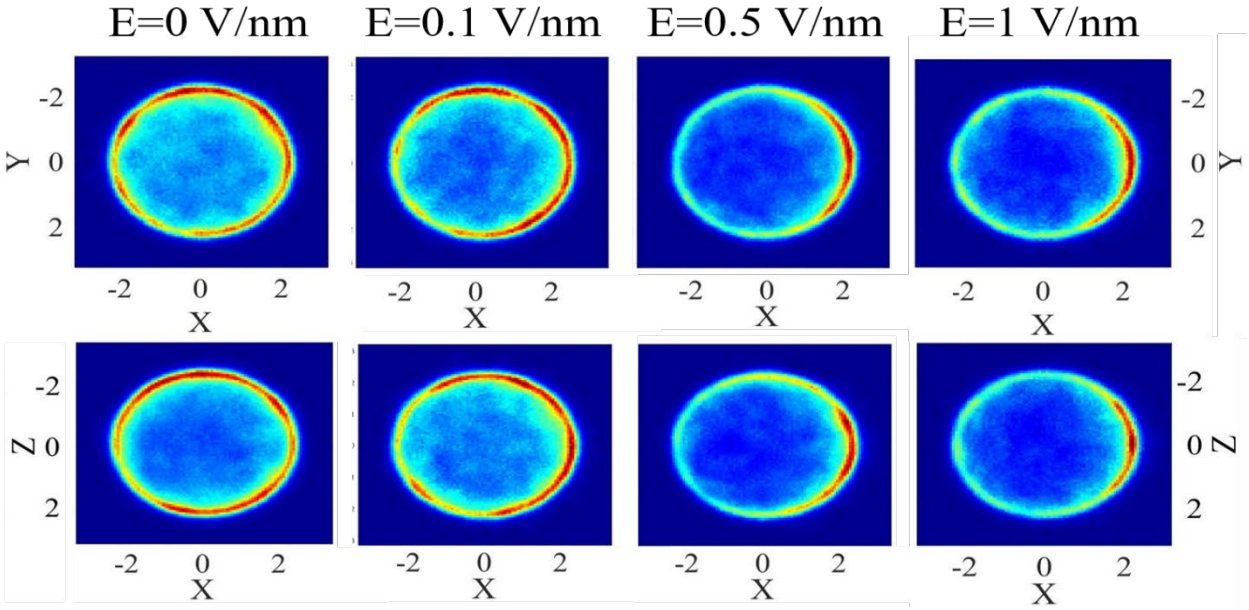

Figure C.2: O^--Na^+ ion-pair (or the PE-brush-counterion) contour for different strengths of the axial electric field.

O^--Na^+ ion-pair (or the PE-brush-counterion) contours, contributing to the brush height reduction, are shown in Figure C.2. An increase in the PE-functional-group-counterion polarization with an increase in the electric field can be observed from this figure.

Water Distribution:

Water (solvent) densities for three cases (i.e., cases with different values of the applied electric field) are shown in Figure C.3. It can be observed that, when brush height gets reduced (with increasing electric field), the density of water inside the brush layer gets reduced too. It also indicates that at a larger electric field strength, water molecules gets squeezed out of the brush which carries ions.

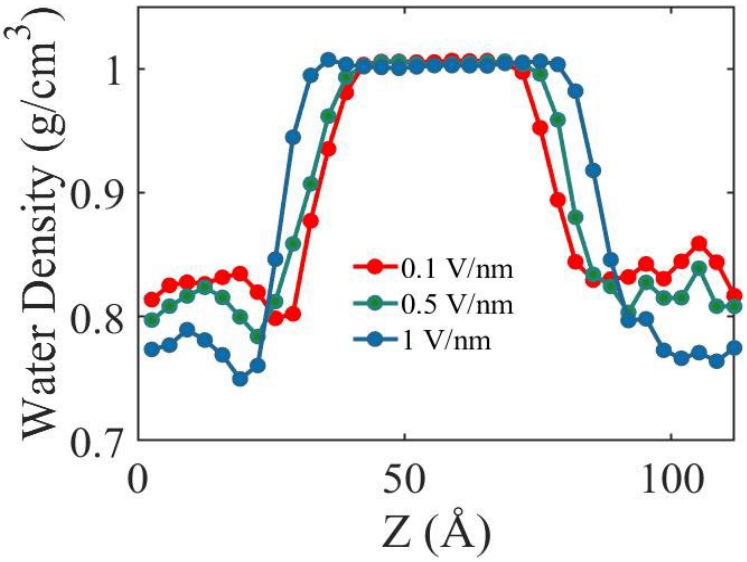

Figure C.3: Water density distribution along the z axis for different axial electric field strengths.

Ionic Properties:

Distribution and velocity profiles of both the ions at an electric field strength of 0.5 V/nm are plotted in Figures C.4(A) and C.4(B), respectively. Here along with the higher concentration of

coions in the bulk, the velocity of coions are also greater than the velocity of counterions: this

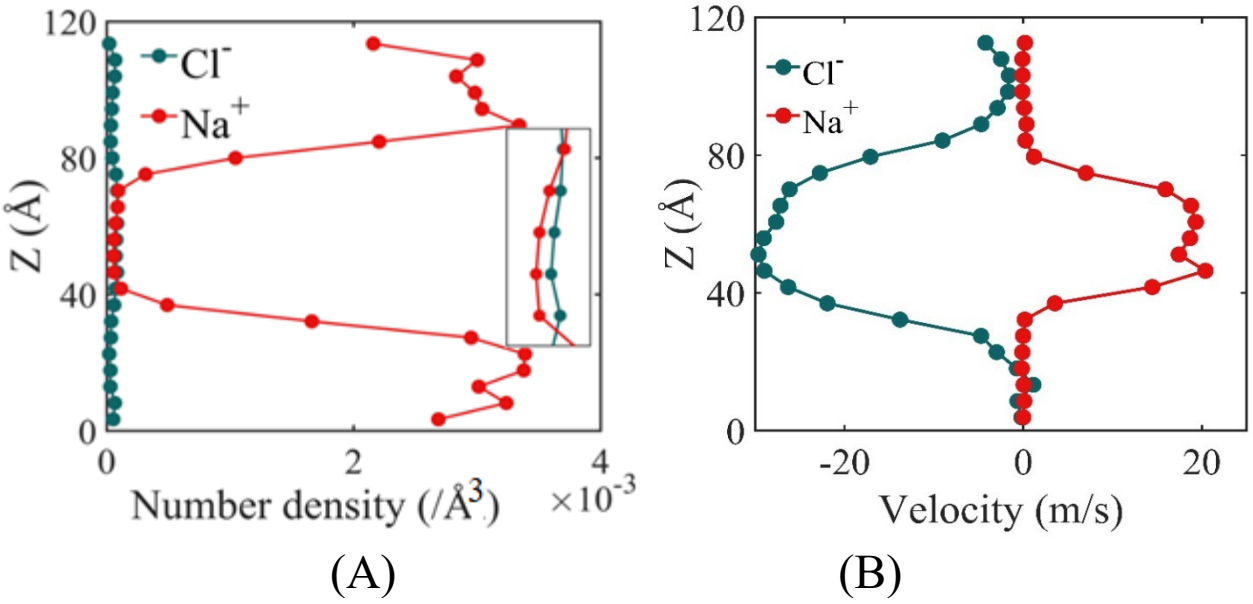

Figure C.4: (A) Number density of ions in the system for |E|=0.5 V/nm. Number density near the bulk region is zoomed in the inset. (B) Coion and Counterion's velocity profile at |E|=0.5 V/nm.

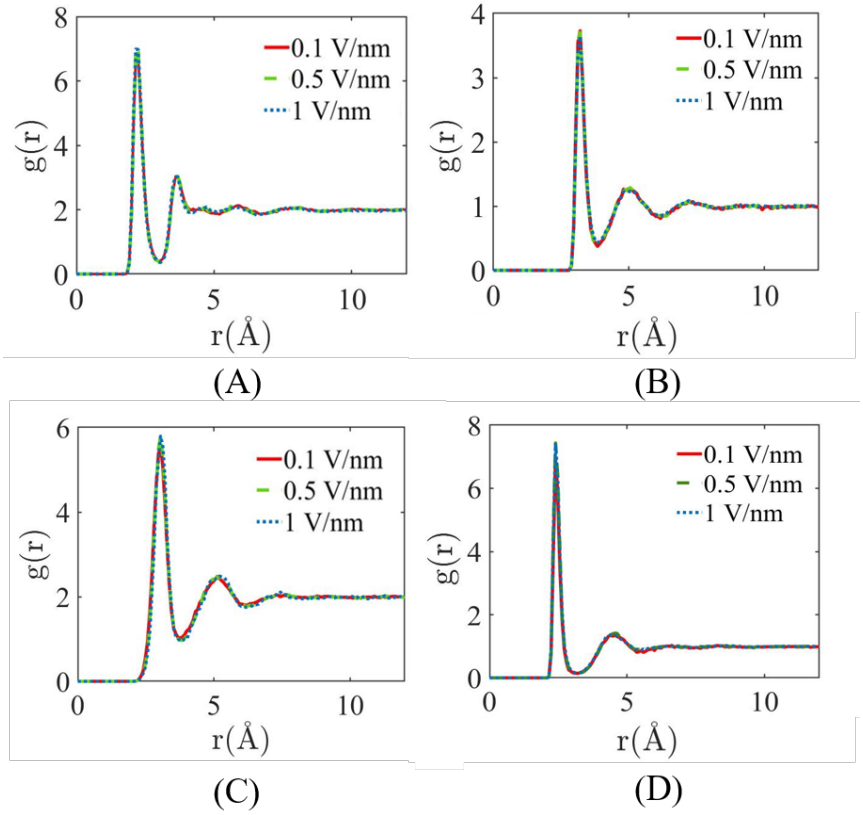

Figure C.5: (A) Cl^--H, (B) Cl^--O, (C) Na^+-H, and (D) Na^+-O RDF in bulk region for different strengths of |E|=0.5 V/nm for different strengths of |E|.

helps to drive the solvent in the negative directions (i.e., the direction of the motion of coions). Therefore, we obtain a coion-dictated EOS transport.

In Figure C.5 we show the different radial distribution functions (RDF) between O and H of water with Cl^- and Na^+ ions in the bulk region. It can be observed that the application of an external electric field does not have any measurable effect on the RDF. We have used the first minima of these RDF as the solvation shell radius to calculate the residence time autocorrelation function. These radii values are tabulated in Table C.1:

RDF type	Cl^--H	Cl^--O	Na^+-H	Na^+-O
Radius (Å)	3.00	3.84	3.76	3.20

Table C.1: Solvation shell radius from RDF

In Figure C.6, we depict the residence time autocorrelation function for |**E**|=0.5 V/nm. Here too, the time scale for water leaving the first solvation shell of ion is higher for Na^+.

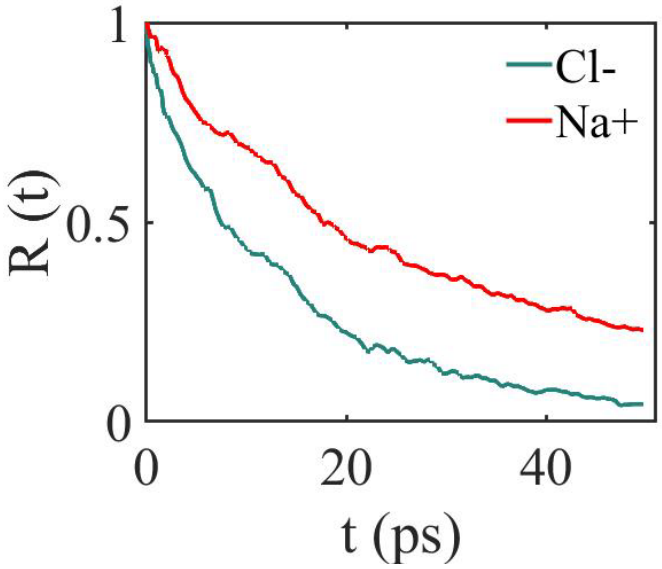

Figure C.6: Residence time autocorrelation function in the bulk region for |E|=0.5 V/nm.

Counterions present inside the PE brush layer are not fully solvated by the water molecules. On the contrary, some of the water molecules of the first solvation shell of the ion are replaced by the O (oxygen atoms) of the negatively charged monomers of the PE chains. Therefore, the solvation number (O_{total}) of the counterions is made up by the contribution from water (O_{water}) and O of the COO^- ($O_{carboxylate}$) groups of the PAA brushes. Such a phenomenon was observed in our previous all-atom MD simulation study that considered PAA brushes in presence of Na^+ counterions but in the absence of any confinement. Here we study this phenomenon for the cases of nanoconfined PAA brushes in presence of either Na^+ or Cs^+ counterions and report the solvation number of the counterions (O_{total}) and the corresponding contributions from water (O_{water}) and O of the COO^- ($O_{carboxylate}$) (see table C.2).

Counterion type	O_{total}	O_{water}	$O_{carboxylate}$
Na^+	6.03	2.88	3.15
Cs^+	9.26	7.84	1.42

Table C.2: Solvation number analysis of Na^+ and Cs^+ inside brush layer.

References:

1. Muthukumar, M. 50th Anniversary Perspective: A Perspective on Polyelectrolyte Solutions. *Macromolecules* **2017**, 50, 9528−9560.
2. Chen, G.; Sachar, H. S.; Das, S. Efficient Electrochemomechanical Energy Conversion in Nanochannels Grafted with End-charged Polyelectrolyte Brushes at Medium and High Salt Concentration. *Soft Matter* **2018**, 14, 5246–5255.
3. Lee, S.; Spencer, N. D. Sweet, hairy, soft, and slippery, *Science* **2008**, 319, 575.
4. Fantner, G. E.; Hassenkam, T.; Kindt, J. H.; Weaver, J. C.; Birkedal, H.; Pechenik, L.; Cutroni, J. A.; Cidade, G. A. G.; Stucky, G. D.; Morse, D. E.; Hansma, P. K. Sacrificial Bonds and Hidden Length Dissipate Energy as Mineralized Fibrils Separate During Bone Fracture, *Nat. Mater.* **2005**, 4, 612.
5. Cheng, X.; Pan, J.; Zhao, Y.; Liao, M.; Peng, H. Gel Polymer Electrolytes for Electrochemical Energy Storage, *Adv. Energy Mater.* **2017**, 8, 1702184.
6. Liu, Z.; Yin, Z.; Wang, J.; Zheng, Q.; Polyelectrolyte Dielectrics for Flexible Low-Voltage Organic Thin-Film Transistors in Highly Sensitive Pressure Sensing*, Adv. Funct. Mater*. **2019**, 29, 1806092.
7. Bronder, T. S.; Jessing, M. P.; Poghossian, A.; Keusgen, M.; Schöning, M. J.; Detection of PCR-Amplified Tuberculosis DNA Fragments with Polyelectrolyte-Modified Field-Effect Sensors, *Anal. Chem.* **2018**, 90, 7747.
8. Aytar, B. S.; Prausnitz, M. R.; Lynn, D. M. Rapid Release of Plasmid DNA from Surfaces Coated with Polyelectrolyte Multilayers Promoted by the Application of Electrochemical Potentials, *ACS Appl. Mater. Interfaces* **2012**, 4, 2726.
9. Wu, D.; Zhu, L.; Li, Y.; Zhang, X.; Xu, S.; Yang, G.; Delair, T. Chitosan-based Colloidal Polyelectrolyte Complexes for Drug Delivery: A Review, *Carbohydr. Polym*. **2020**, 238, 116126.
10. Gbadamosi, A. O.; Junin, R.; Manan, M. A.; Yekeen, N.; Agi, A.; Oseh, J. O.; Recent Advances and Prospects in Polymeric Nanofluids Application for Enhanced Oil Recovery, *J. Ind. Eng. Chem.* **2018**, 66, 1.
11. Virga, E.; de Grooth, J.; Žvab, K.; de Vos, W. M. Stable Polyelectrolyte Multilayer-Based Hollow Fiber Nanofiltration Membranes for Produced Water Treatment, *ACS Appl. Polym. Mater*. **2019**, 1, 2230.
12. Tamer, T. M.; Hassan, M. A.; Valachová, K.; Omer, A. M.; El-Shafeey, M. E. A.; Eldin, M. S. M.; Šoltés, L.; Enhancement of Wound Healing by Chitosan/Hyaluronan Polyelectrolyte Membrane Loaded with Glutathione: in vitro and in vivo Evaluations, *J. Biotechnol.* **2020,** 310, 103.
13. Ali, M.; Schiedt, B.; Neumann, R.; Ensinger, W. Biosensing with Functionalized Single Asymmetric Polymer Nanochannels. *Macromol. Biosci.* **2010**, 10, 28−32.

14. Umehara, S.; Karhanek, M.; Davis, R. W.; Pourmand, N. Label-Free Biosensing with Functionalized Nanopipette Probes. *Proc. Natl. Acad. Sci.* **2009**, 106, 4611−4616.

15. Motornov, M.; Sheparovych, R.; Lupitskyy, R.; MacWilliams, E.; Hoy, O.; Luzinov, I.; Minko, S. Stimuli-Responsive Colloidal Systems from Mixed Brush-Coated Nanoparticles. *Adv. Funct. Mater.* **2007**, 17, 2307–2314.

16. Yang, Q.; Li, L.; Zhao, F.; Han, H.; Wang, W.; Tian, Y.; Wang, Y.; Ye, Z.; Guo, X. Hollow Silica–Polyelectrolyte Composite Nanoparticles for Controlled Drug Delivery. *J. Mater. Sci.* **2019**, 54, 2552–2565.

17. Saraswathy, M.; Gong, S. Recent Developments in the Co-Delivery of Sirna and Small Molecule Anticancer Drugs for Cancer Treatment. *Mater. Today* **2014**, 17, 298–306.

18. ShamsiJazeyi, H.; Miller, C. A.; Wong, M. S.; Tour, J. M.; Verduzco, R. Polymer-Coated Nanoparticles for Enhanced Oil Recovery. *J. Appl. Polym. Sci.* **2014**, 131, 40576.

19. Manzato, C.; Foster, A. S.; Alava, M. J.; Laurson, L. Friction control with nematic lubricants via external fields, *Phys. Rev. E*, **2015**, 91, 012504.

20. Drummond, C. Electric-Field-Induced Friction Reduction and Control. *Phys. Rev. Lett.* **2012**, 109, 154302.

21. Zhang, P.; Qian, J.; Yang, Y.; An, Q.; Liu, X.; Gui, Z. Polyelectrolyte Layer-by-Layer Self-Assembly Enhanced by Electric Field and their Multilayer Membranes for Separating Isopropanol–Water Mixtures. *J. Membr. Sci.* **2008**, 320, 73-77.

22. Zhang, P.; Qian, J.; An, Q.; Liu, X.; Zhao, Q.; Jin, H. Surface Morphology and Pervaporation Performance of Electric Field Enhanced Multilayer Membranes. *J. Membr. Sci.* **2009**, 328, 141-147.

23. Yin, M.; Qian, J.; An, Q.; Zhao, Q.; Gui, Z.; Li, J. Polyelectrolyte Layer-by-Layer Self-Assembly at Vibration Condition and the Pervaporation Performance of Assembly Multilayer Films in Dehydration of Isopropanol. *J. Membr. Sci.* **2010**, 358, 43-50.

24. Li, Y.; Sun, Y.; Xiao, Y.; Gao, G.; Liu, S.; Zhang, J.; Fu, J. Electric Field Actuation of Tough Electroactive Hydrogels Cross-linked by Functional Triblock Copolymer Micelles. *ACS Appl. Mater. Interfaces* **2016**, 8, 26326-26331.

25. Zolfagharian, A.; Kaynak, A.; Khoo, S. Y.; Kouzani, A. Z. Polyelectrolyte Soft Actuators: 3D Printed Chitosan and Cast Gelatin. *3D Print Addit. Manuf.* **2018**, 5, 138-150.

26. Blyakhman, F. A.; Safronov, A. P.; Shklyar, T. F.; Filipovich, M. A. To the Mechanism of Polyelectrolyte Gel Periodic Acting in the Constant DC Electric Field. *Sens. Actuator A Phys*. **2015**, 229, 104-109.

27. Roy, T.; Szuttor, K.; Smiatek, J.; Holm, C.; Hardt, S. Electric-field-induced Stretching of Surface-tethered Polyelectrolytes in a Microchannel. *Phys. Rev. E.* **2017**, 96, 032503.

28. Netz, R. R. Nonequilibrium Unfolding of Polyelectrolyte Condensates in Electric Fields. *Phys. Rev. Lett*. **2003**, 90, 128104.

29. Suma, A.; Di Stefano, M.; Micheletti, C. Electric-Field-Driven Trapping of Polyelectrolytes in Needle-Like Backfolded States. *Macromolecules* **2018**, 51, 4462-4470.

30. Yuan, J.; Antila, H. S.; Luijten, E. Structure of Polyelectrolyte Brushes on Polarizable Substrates. *Macromolecules* **2020**, 53, 2983-2990.

31. Gordievskaya, Y. D.; Kramarenko, E. Y. Effect of Counterion Size on the Structure of a Flexible Polyelectrolyte Chain in Low-polar Solvents. *Polym. Sci., Ser. C* **2018,** 60, 37−48.

32. Gordievskaya, Y. D.; Gavrilov, A. A.; Kramarenko, E. Y. Effect of Counterion Excluded Volume on the Conformational Behavior of Polyelectrolyte Chains. *Soft Matter*, **2018**, 14, 1474-1481

33. Yu, J.; Mao, J.; Yuan, G.; Satija, S.; Jiang, Z.; Chen, W.; Tirrell, M. Structure of Polyelectrolyte Brushes in the Presence of Multivalent Counterions. *Macromolecules* **2016**, 49, 5609−5617.

34. Xu, X.; Mastropietro, D.; Ruths, M.; Tirrell, M.; Yu, J. Ion-Specific Effects of Divalent Ions on the Structure of Polyelectrolyte Brushes. *Langmuir* **2019**, 35, 15564−15572.

35. Allen, F. J.; Griffin, L. R.; Alloway, R. M.; Gutfreund, P.; Lee, S. Y.; Truscott, C. L.; Welbourn, R. J. L.; Wood, M. H., Clarke, S. M. An Anionic Surfactant on an Anionic Substrate: Monovalent Cation Binding, *Langmuir* **2017**, *33*, 7881−7888.

36. Allen, F. J.; Truscott, C. L.; Gutfreund, P.; Welbourn, R. J. L.; Clarke, S. M. Potassium, Calcium, and Magnesium Bridging of AOT to Mica at Constant Ionic Strength, *Langmuir* **2019**, *35*, 5753−5761.

37. Chang C.-C.; Yang, R.-J. Electrokinetic Mixing in Microfluidic Systems. *Microfluid. Nanofluid*. **2007,** *3*, 501–525.

38. Shestopalov, I.; Tice, J. D.; Ismagilov, R. F.; Multi-Step Synthesis of Nanoparticles Performed on Millisecond Time Scale in a Microfluidic Droplet-Based System. *Lab Chip* **2004**, *4*, 316–321.

39. Pamme, N. Continuous Flow Separations in Microfluidic Devices. *Lab Chip* **2007**, *7*, 1644–1659.

40. Weisgrab, G.; Ovsianikov, A.; Costa, P. F. Functional 3D Printing for Microfluidic Chips *Adv. Mater. Technol.* **2019**, *4*, 1900275.

41. Esfandyarpour, R.; DiDonatoc, M. J.; Yangd, Y.; Durmus, N. G.; Harrisd, J. S.; Davis, R. W. Multifunctional, Inexpensive, and Reusable Nanoparticle-Printed Biochip for Cell Manipulation and Diagnosis. *Proc. Natl. Acad. Sci. USA* **2017**, *114*, E1306–E1315.

42. Chen, G.; Das, S. Scaling Laws and Ionic Current Inversion in Polyelectrolyte-Grafted Nanochannels. *J. Phys. Chem. B* **2015***, 119*, 12714–12726.

43. Chen, G.; Das, S. Electroosmotic Transport in Polyelectrolyte-Grafted Nanochannels with pH-Dependent Charge Density. *J. Appl. Phys.* **2015,** *117*, 185304.

44. Cao, Q.; You, H. Electroosmotic Flow in Mixed Polymer Brush-Grafted Nanochannels. *Polymers* **2016**, *8*, 438.

45. Cao, Q.; Tian, X.; You, H. Electrohydrodynamics in Nanochannels Coated by Mixed Polymer Brushes: Effects of Electric Field Strength and Solvent Quality. *Model. Simul. Mater. Sci. Eng*. **2018**, *26*, 035003.

46. Cao, Q. Anisotropic Electrokinetic Transport in Channels Modified with Patterned Polymer Brushes. *Soft Matter* **2019**, *15*, 4132–4145.

47. J. Yu, N. E. Jackson X. Xu, Y. Morgenstern, Y. Kaufman, M. Ruths, J. J. de Pablo, M. Tirrell, Multivalent Counterions Diminish the Lubricity of Polyelectrolyte Brushes, *Science* **2018**, *360,* 1434–1438.

48. Vilozny, B.; Wollenberg, A. L.; Actis, P.; Hwang, D.; Singaram, B.; Pourmand, N. Carbohydrate-actuated nanofluidic diode: Switchable current rectification in a nanopipette, *Nanoscale* **2013**, 5, 9214−9221.

49. Ali, M.; Ramirez, P.; Nasir, S.; Cervera, J.; Mafe, S.; Ensinger, W. Ionic circuitry with nanofluidic diodes, *Soft Matter***, 2019**,15, 9682-9689.

50. Ali, M.; Neumann, R.; Ensinger, W.; Sequence-Specific Recognition of DNA Oligomer Using Peptide Nucleic Acid (PNA)-Modified Synthetic Ion Channels: PNA/DNA Hybridization in Nanoconfined Environment, *ACS Nano* **2010**, 4, 7267–7274

51. Buchsbaum, S. F.; Nguyen, G.; Howorka, S.; Siwy, Z. S. DNA-Modified Polymer Pores Allow pH- and Voltage-Gated Control of Channel Flux, *J. Am. Chem. Soc.* **2014**, 136, 9902–9905

52. Zhou, C.; Mei, L.; Sub, Y.-S.; Yeh, L.-H.; Zhang, X.; Qian, S. Gated ion transport in a soft nanochannel with biomimetic polyelectrolyte brush layers, *Sensors and Actuators B: Chemical*, **2016**, 229, 305-314.

53. Mahinthichaichan, P.; Tsai, C. C.; Payne, G. F.; Shen, J. Polyelectrolyte in Electric Field: Disparate Conformational Behavior Along an Aminopolysaccharide Chain. *ACS Omega* **2020**, *5*, 12016-12026.

54. Kobayashi, M.; Terada, M.; Takahara, A. Polyelectrolyte Brushes: A Novel Stable Lubrication System in Aqueous Conditions. *Faraday Discuss.* **2012,** *156*, 403-412.

55. Ma, S.; Zhang, X.; Yu, B.; Zhou, F. Brushing up Functional Materials. *NPG Asia Mater.* **2019**, *11*, 24.

56. Hsu, H.-P.; Paul, W.; Binder, K.; Standard Definitions of Persistence Length Do Not Describe the Local "Intrinsic" Stiffness of Real Polymer Chains. *Macromolecules* **2010,** *43*, 3094-3102.

57. Xia, P.; Zhang, L.; Li, F. Learning Similarity with Cosine Similarity Ensemble. *Information Science* **2015,** *307*, 39-52.

58. Cheng, C. H. A.; Kellogg, L. H.; Shkoller, S.; Turcotte, D. L. A liquid-Crystal Model for Friction. *Proc. Natl. Acad. Sci. U.S.A.* **2008,** *105*, 7930-7935.

59. Yu, Y.; Yao, Y.; van Lin, S.; de Beer, S. Specific Anion Effects on the Hydration and Tribological Properties of Zwitterionic Phosphorylcholine-Based Brushes. *Eur. Polym. J* , **2019**, *112*, 222-227.

60. Hollingsworth, N. R.; Wilkanowiczbc, S. I.; Larson, R. G. Saltand pH-Induced Swelling of a Poly (acrylic Acid) Brush via Quartz Crystal Microbalance w/Dissipation (QCM-D). *Soft Matter* **2019,** *15*, 7838−7851.

61. Tran, Y.; Auroy, P. Synthesis of Poly (styrene sulfonate) Brushes. *J. Am. Chem. Soc.* **2001,** *123,* 3644-3654.

62. Saitta, A. M.; Saija, F.; Giaquinta, P. V. Ab Initio Molecular Dynamics Study of Dissociation of Water under an Electric Field. *Phys. Rev. Lett.* **2012,** *108,* 207801.

63. Stuve, E. M. Ionization of Water in Interfacial Electric Fields: An Electrochemical View. *Chem. Phys. Lett.* **2012,** *519,* 1-17.

64. Scovell, D. L.; Pinkerton, T. D.; Medvedev, V. K.; Stuve, E.M. Phase Transitions in Vapor-Deposited Water Under the Influence of High Surface Electric Fields. *Surf. Sci.* **2000,** *457,* 365-376.

65. Ly, H. K.; Sezer, M.; Wisitruangsakul, N.; Feng, J. J.; Kranich, A.; Millo, D.; Weidinger, I. M.; Zebger, I.; Murgida, D. H.; Hildebrandt, P. Surface-Enhanced Vibrational Spectroscopy for Probing Transient Interactions of Proteins with Biomimetic Interfaces: Electric Field Effects on Structure, Dynamics and Function of Cytochrome C. *FEBS J.* **2011,** *278,* 1382-1390.

66. Heng, J. B.; Aksimentiev, A.; Ho, C.; Marks, P.; Grinkova, Y. V.; Sligar, S.; Schulten, K.; Timp, G. The Electromechanics of DNA in a Synthetic Nanopore. *Biophys. J.* **2006,** *90*, 1098-1106.

67. Berendsen, H. J. C.; Grigera, J. R.; Straatsma, T. P. The Missing Term in Effective Pair Potentials. *J. Phys. Chem.* **1987,** *91*, 6269–6271.

68. Hockney, R. W.; Eastwood, J. W. *Computer Simulations Using Particles*; McGraw-Hill International Book Co, New York, 1981.

69. Ryckaert, J.-P.; Ciccotti, G.; Berendsen, H. J. Numerical Integration of the Cartesian Equation of Motion of a System with Constraints: Molecular Dynamics of n-Alkanes. *J. Comput. Phys.* **1977***, 23*, 327–341.

70. Plimpton, S. Fast Parallel Algorithms for Short-range Molecular Dynamics. *J. Comput. Phys*. **1995**, *117,* 1–19.

71. Stukowski, A. Visualization and Analysis of Atomistic Simulation Data with OVITO–the Open Visualization Tool. *Model. Simul. Mater. Sci. Eng.* **2010**, *18*, 015012.

72. Jorgensen, W. L.; Maxwell, D. S.; Tirado-Rives, J. Development and Testing of the OPLS All-Atom Force Field on Conformational Energetics and Properties of Organic Liquids. *J. Am. Chem. Soc.* **1996,** *118*, 11225–11236.

73. Joung, I. S.; Cheatham III, T. E. Determination of Alkali and Halide Monovalent Ion Parameters for Use in Explicitly Solvated Biomolecular Simulations. *J. Phys. Chem. B* **2008,** *112*, 9020–9041.

74. Odegard, G. M.; Clancy, T. C.; Gates, T. S. Prediction of Mechanical Properties of Polymers with Various Force Fields *46th AIAA/ASME/ASCE/AHS/ASC Structures, Structural Dynamics and Materials Conference,* Austin, 2005.

75. Smith, M. D.; Rao, J. S.; Segelken, E.; Cruz, L. Force-Field Induced Bias in the Structure of Aβ21–30: A Comparison of OPLS, AMBER, CHARMM, and GROMOS Force Fields. *J. Chem. Inf. Model.* **2015**, *55*, 2587-2595.

76. Sharma, P.; Roy, S.; Karimi-Varzaneh, H. A. Validation of Force Fields of Rubber through Glass-Transition Temperature Calculation by Microsecond Atomic-Scale Molecular Dynamics Simulation. *J. Phys. Chem. B* **2016**, *120*, 1367-1379.

77. Hu, Z.; Jiang, J. Assessment of Biomolecular Force Fields for Molecular Dynamics Simulations in a Protein Crystal. *J. Comput. Chem.* **2009***, 31,* 372-380.

78. Joung, I. S.; Cheatham III, T. E. Molecular Dynamics Simulations of the Dynamic and Energetic Properties of Alkali and Halide Ions Using Water-Model-Specific Ion Parameters *J. Phys. Chem. B* **2009**, 113, 13279–13290.

79. Hoover, W. G. Canonical Dynamics: Equilibrium Phase-Space Distributions. *Phys. Rev. A* **1985**, *31*, 1695–1697.

80. Nosé, S. A Unified Formulation of the Constant Temperature Molecular Dynamics Methods. *J. Chem. Phys*. **1984**, *81*, 511–519.

81. Schneider, T.; Stoll, E. Molecular-Dynamics Study of a Three-Dimensional One-Component Model for Distortive Phase Transitions. *Phys. Rev. B* **1987***, 17*, 1302–1322.

82. Qiao, B.; Cerda, J.J.; Holm, C. Poly (styrenesulfonate)-Poly (diallyldimethylammonium) Mixtures: Toward the Understanding of Polyelectrolyte Complexes and Multilayers via Atomistic Simulations. *Macromolecules* **2010,** *43,* 7828-7838.

83. Das, S.; Banik, M.; Chen, G.; Sinha S.; Mukherjee, R. Polyelectrolyte brushes: theory, modelling, synthesis and applications. *Soft Matter* **2015**, *11*, 8550−8583.

84. Ali, M.; Yameen, B.; Cervera, J.; Ramírez, P.; Neumann, R.; Ensinger, W.; Knoll, W.; Azzaroni, O. Layer-by-layer Assembly of Polyelectrolytes into Ionic Current Rectifying Solid-state Nanopores: Insights from Theory and Experiment. *J. Am. Chem. Soc*. **2010**, *132*, 8338−8348.

85. Yameen, B.; Ali, M.; Neumann, R.; Ensinger, W.; Knoll, W.; Azzaroni, O. Single Conical Nanopores Displaying pH-Tunable Rectifying Characteristics. Manipulating Ionic Transport with Zwitterionic Polymer Brushes. *J. Am. Chem. Soc*. **2009**, *131*, 2070−2071.

86. Stuart, M. A. C.; Huck, W. T. S.; Genzer, J.; Muller, M.; Ober, C.; Stamm, M.; Sukhorukov, G. B.; Szleifer, I.; Tsukruk, V. V.; Urban, M.; Winnik, F.; Zauscher, S.; Luzinov, I.; Minko, S. Emerging Applications of Stimuli-responsive Polymer Materials. *Nat. Mater.* **2010**, *9*, 101-113.

87. Mei, Y.; Lauterbach, K.; Hoffmann, M.; Borisov, O. V.; Ballauff, M.; Jusufi, A. Collapse of Spherical Polyelectrolyte Brushes in the Presence of Multivalent Counterions. *Phys. Rev. Lett.* **2006**, *97*, 158301.

88. Xu, Y.; Bolisetty, S.; Drechsler, M.; Fang, B.; Yuan, J.; Harnau, L.; Ballauff, M.; Müller, A. H. E. Manipulating Cylindrical Polyelectrolyte Brushes on the Nanoscale by Counterions: Collapse Transition to Helical Structures. *Soft Matter* **2009**, *5*, 379−384.

89. Farina, R.; Laugel, N.; Yu, J.; Tirrell, M. Reversible Adhesion with Polyelectrolyte Brushes Tailored via the Uptake and Release of Trivalent Lanthanum Ions. *J. Phys. Chem. C* **2015**, *119*, 14805−14814.

90. Nap, R. J.; Park, S. H.; Szleifer, I. Competitive Calcium Ion Binding to End-tethered Weak Polyelectrolytes, *Soft Matter,* **2018,** *14*, 2365-2378.

91. Ezhova, A.; Huber, K. Contraction and Coagulation of Spherical Polyelectrolyte Brushes in the Presence of Ag+, Mg2+, and Ca2+ Cations. *Macromolecules* **2016,** *49*, 7460−7468.

92. Jackson, N. E.; Brettmann, B. K.; Vishwanath, V.; Tirrell, M.; Pablo, J. J. d.; Comparing Solvophobic and Multivalent Induced Collapse in Polyelectrolyte Brushes, *ACS Macro Lett.* **2017**, *6*, 155−160.

93. Yu, J.; Jackson, N. E.; Xu, X.; Brettmann, B. K.; Ruths, M.; Pablo, J. J. d.; Tirrell, M. Multivalent Ions Induce Lateral Structural Inhomogeneities in Polyelectrolyte Brushes, *Sci. Adv.* **2017**, *3:* eaao1497.

94. Mei, Y.; Hoffmann, M.; Ballauff, M.; Jusufi, A.; Spherical Polyelectrolyte Brushes in the Presence of Multivalent Counterions: The effect of Fluctuations and Correlations as Determined by Molecular Dynamics Simulations*, Phys. Rev. E* **2008**, 77, 031805.

95. Wang, X.; Lee, S. Y.; Miller, K.; Welbourn, R.; Stocker, I.; Clarke, S.; Casford, M.; Gutfreund, P.; Skoda, M. W. A. Cation Bridging Studied by Specular Neutron Reflection. *Langmuir* **2013**, *29*, 5520− 5527.

96. Li, Y.; Hao, Q.H.; Xia, S.Y.; Yan, D.X.; Tan, H. G. Morphologies of Spherical Bidisperse Polyelectrolyte Brushes in the Presence of Trivalent Counterions. *Chemical Physics,* **2020** *539,* 110941.

97. Higgs, P. G.; Orland, H. Scaling Behavior of Polyelectrolytes and Polyampholytes: Simulation by an Ensemble Growth Method. *J. Chem. Phys*. **1991,** *95*, 4506-4518.

98. Mintis, D.G.; Mavrantzas, V. G. Effect of pH and Molecular Length on the Structure and Dynamics of Short Poly(acrylic acid) in Dilute Solution: Detailed Molecular Dynamics Study. *J. Phys. Chem. B* **2019**, 123, 4204−4219.

99. Brettmann, B.; Pincus, P.; Tirrell, M. Lateral Structure Formation in Polyelectrolyte Brushes Induced by Multivalent Ions. *Macromolecules,* **2017**, 50, 1225−1235.

100. Sachar, H. S.; Pial, T. H.; Chava, B. S.; Das, S. All-atom Molecular Dynamics Simulations of Weak Polyionic Brushes: Influence of Charge Density on the Properties of Polyelectrolyte Chains, Brush-supported Counterions, and Water Molecules. *Soft Matter*, **2020**, *16*, 7808-7822.

101. Lee, S. H.; Rasaiah, J. C. Molecular Dynamics Simulation of Ion Mobility. 2. Alkali Metal and Halide Ions Using the SPC/E Model for Water at 25 °C. *J. Phys. Chem.* **1996**, *100*, 1420-1425.

102. Yu, h.; Whitfield, T. W.; Harder, E.; Lamoureux, G.; Vorobyov, I.; Anisimov, V. M.; MacKerell Jr. A. D.; Roux, B. Simulating Monovalent and Divalent Ions in Aqueous Solution Using a Drude Polarizable Force Field. *J Chem Theory Comput.* **2010,** *6*, 774–786.

103. Piquemal, J. -P.; Perera, L.; Cisneros, G. A.; Ren, P.; Pedersen, L. G.; Darden, T. A. Towards Accurate Solvation Dynamics of Divalent Cations in Water Using the Polarizable Amoeba Force Field: From Energetics to Structure. *J. Chem. Phys.* **2020**, *125*, 054511.

104. Smirnov, P. R.; Trostin, V. N. Structural Parameters of Close Surroundings of Sr2+ and Ba2+ Ions in Aqueous Solutions of Their Salts. *Russ J Gen Chem,* **2011** *81*, 282–289.

105. Lindqvist-Reis, P.; Lamble, K.; Pattanaik, S.; Persson, I.; Sandström, M. Hydration of the Yttrium(III) Ion in Aqueous Solution. An X-ray Diffraction and XAFS Structural Study. *J. Phys. Chem. B* **2000**, *104*, 2, 402–408.

106. Na1slund, J.; Lindqvist-Reis, P.; Persson, I.; Sandström, M. Steric Effects Control the Structure of the Solvated Lanthanum(III) Ion in Aqueous, Dimethyl Sulfoxide, and N,N¢-Dimethylpropyleneurea Solution. An EXAFS and Large-Angle X-ray Scattering Study. *Inorg. Chem.* **2000,** *39,* 4006-4011.

107. Díaz-Moreno, S.; Ramos, S.; Bowron, D. T.; Solvation Structure and Ion Complexation of La^{3+} in a 1 Molal Aqueous Solution of Lanthanum Chloride. *J. Phys. Chem. A* **2011**, 115, 6575–6581.

108. Sachar, H. S.; Pial, T. H.; Desai, P. R.; Etha, S. A.; Wang, Y.; Chung, P. W.; Das, S. Densely Grafted Polyelectrolyte Brushes Trigger "Water-in-Salt"-like Scenarios and Ultraconfinement Effect. *Matter* **2020**, *2*, 1509–1521.

109. Liu, L.; Pincus, P. A.; Hyeon, C. Heterogeneous Morphology and Dynamics of Polyelectrolyte Brush Condensates in Trivalent Counterion Solution. *Macromolecules* **2017**, 50, 1579−1588.

110. Andreev, M.; Pablo,J. J. d.; Chremos,A.; Douglas, J. F.; Influence of Ion Solvation on the Properties of Electrolyte Solutions, *J. Phys. Chem. B,* **2018**, *122*, 4029−4034.

111. He, G.L.; Merlitz, H.;Sommer, J.U. Molecular Dynamics Simulations of Polyelectrolyte Brushes Under Poor Solvent Conditions: Origins of Bundle Formation, *J. Chem. Phys.* **2014**, 140, 104911.

112. Carrillo, J.M.Y.; Dobrynin, A.V. Morphologies of Planar Polyelectrolyte Brushes in a Poor Solvent: Molecular Dynamics Simulations and Scaling Analysis, *Langmuir*, **2009**, 25, 13158–13168.

113. Li, P.; Roberts, B. P.; Chakravorty, D. K.; Merz Jr, K. M. Rational Design of Particle Mesh Ewald Compatible Lennard-Jones Parameters for +2 Metal Cations in Explicit Solvent, *J. Chem. Theory Comput.,* **2013,** 9, 2733–2748.

114. Li, P.; Song, L. F.; Merz Jr, K. M.; Parameterization of Highly Charged Metal Ions Using the 12-6-4 LJ Type Nonbonded Model in Explicit Water, *J. Phys. Chem. B,* **2015**, 119, 883-895.

115. Fernández, C.D.R.; Campos, H.M.; Lago, E.L. Fuente, R.D.L.; Varela, L. M. Microstructure, Dynamics and Optical Properties of Metal-doped Imidazolium-based Ionic Liquids. *J. Mol. Liq.* **2020**, 317, 113866.

116. Luna, J. M. V.; Azaceta, E.; Hamad, S.; Roldán, J.M.O.; Zaera, R.T.; Calero, S.; Anta, J.A. Molecular Dynamics Analysis of Charge Transport in Ionic-Liquid Electrolytes Containing Added Salt with Mono, Di, and Trivalent Metal Cations. *ChemPhysChem* **2018**, 19, 1665 – 1673.

117. Plümper, O.; Botan, A.; Los, C.; Liu, Y.; Malthe-SØrenssen, A.; Jamtveit, B. Fluid-Driven Metamorphism of The Continental Crust Governed by Nanoscale Fluid Flow. *Nat. Geosci.* **2017**, *10*, 685–690.

118. Zhu, Y.; Zhan, K.; Zhu, X. Interface Design of Nanochannels for Energy Utilization. *ACS Nano* **2018,** 12, 908–911.

119. van der Heyden, F. H. J.; Bonthuis, D. J.; Stein, D.; Meyer, C.; Dekker, C. Electrokinetic Energy Conversion Efficiency in Nanofluidic Channels. *Nano Lett***. 2006**, 6, 2232–2237.

120. Venkatesan, B. M.; Bashir, R. Nanopore Sensors for Nucleic Acid Analysis. *Nat. Nanotechnol.* **2011**, 6, 615–624.

121. Miles, B. N.; Ivanov, A. P.; Wilson, K. A.; Dogan, F.; Japrung, D.; Edel, J. B. Single Molecule Sensing with Solid-State Nanopores: Novel Materials, Methods, and Applications. *Chem. Soc. Rev.* **2013**, 42, 15–28.

122. Fang, R.; Zhang, H.; Yang, L.; Wang, H.; Tian, Y.; Zhang, X.; Jiang, L. Supramolecular Self-Assembly Induced Adjustable Multiple Gating States of Nanofluidic Diodes. *J. Am. Chem. Soc.* **2016**, 138, 16372–16379.

123. Liu, M.; Zhang, H.; Li, K.; Heng, L.; Wang, S.; Tian, Y.; Jiang, L. A Bio-Inspired Potassium and pH Responsive Double-Gated Nanochannel. *Adv. Funct. Mater***. 2015**, 25, 421–426.

124. Huang, X.; Kong, X. Y.; Wen, L.; Jiang, L. Bioinspired Ionic Diodes: From Unipolar to Bipolar. *Adv. Funct. Mater***. 2018**, 28, 1801079.

125. Zhang, Z.; Wen, L. P.; Jiang, L. Bioinspired Smart Asymmetric Nanochannel Membranes. *Chem. Soc. Rev.* **2018,** 47, 322–356.

126. Chen, L.-C.; Wu, C.-C.; Wu, R.-G.; Chang, H.-C. Electroosmotic Flow Control in Microfluidic Chips Using a Self-Assembled Monolayer as the Insulator of a Flow Field-Effect Transistor, *Langmuir* **2012,** 28, 11281–11285.

127. Oh, Y.-J.; Gamble, T. C.; Leonhardt, D.; Chung, C.-H.; Brueck, S. R. J.; Ivory, C. F.; Lopez, G. P.; Petseva, D. N.; Han, S. M. Monitoring FET Flow Control and Wall Adsorption of Charged Fluorescent Dye Molecules in Nanochannels Integrated into a Multiple Internal Reflection Infrared Waveguide. *Lab Chip* **2008**, 8, 251–258.

128. Hayes, M. A.; Kheterpal, I.; Ewing, A. G. Effects of Buffer pH on Electroosmotic Flow Control by an Applied Radial Voltage for Capillary Zone Electrophoresis. *Anal. Chem.* **1993**, 65, 27–31.

129. Barker, S. L. R.; Ross, D.; Tarlov, M. J.; Gaitan, M.; Locascio, L. E. Control of Flow Direction in Microfluidic Devices with Polyelectrolyte Multilayers. *Anal. Chem.* **2000,** 72, 5925–5929.

130. Stroock, A. D.; Weck, M.; Chiu, D. T.; Huck, W. T. S.; Kenis, P. J. A.; Ismagilov, R. F.; Whitesides, G. M. Patterning Electro-Osmotic Flow with Patterned Surface Charge. *Phys. Rev. Lett.* **2000**, 84, 3314–3317.

131. Celebi, A. T.; Cetin, B.; Beskok, A. Molecular and Continuum Perspectives on Intermediate and Flow Reversal Regimes in Electroosmotic Transport. *J. Phys. Chem. C* **2019**, 123, 14024–14035.

132. Gao, X.; Zhao, T.; Li, T. Controlling Flow Direction in Nanochannels by Electric Field Strength. *Phys. Rev. E* **2015**, 92, 023017.

133. Ali, M.; Yameen, B.; Neumann, R.; Ensinger, W.; Knoll, W.; Azzaroni, O. Biosensing and Supramolecular Bioconjugation in Single Conical Polymer Nanochannels. Facile Incorporation of Biorecognition Elements into Nanoconfined Geometries. *J. Am. Chem. Soc.* **2008**, 130, 16351–16357.

134. Ali, M.; Ramirez, P.; Mafe, S.; Neumann, R.; Ensinger, W. A pH-Tunable Nanofluidic Diode with a Broad Range of Rectifying Properties. *ACS Nano* **2009**, 3, 603–608.

135. Wu, P.; Sun, T.; Jiang, X.; Kondrat, S. Hydrodynamic Properties of Polymers Screening the Electrokinetic Flow: Insights from a Computational Study. *Polymers* **2019,** 11, 1038.

136. Haywood, D. G.; Harms, Z. D.; Jacobson, Stephen C. Electroosmotic Flow in Nanofluidic Channels. *Anal. Chem.* **2014**, 86, 11174−11180.

137. Wu, D.; Qin, J.; Lin, B. Self-Assembled Epoxy-Modified Polymer Coating on a Poly(dimethylsiloxane) Microchip for EOF Inhibition and Biopolymers Separation. *Lab Chip* **2007**, 7, 1490–1496.

138. Paratore, F.; Boyko, E.; Kaigala, G.V.; Bercovici, M. Electroosmotic Flow Dipole: Experimental Observation and Flow Field Patterning. *Phys. Rev. Lett.* **2019,** 122, 224502.

139. English, N. J.; Waldron, C. J. Perspectives on External Electric Fields in Molecular Simulation: Progress, Prospects and Challenges. *Phys. Chem. Chem. Phys.* **2015,** 17, 12407–12440.

140. Netz, R. R. Polyelectrolytes in Electric Fields, *J. Phys. Chem. B* **2003,** 107, 8208–8217.

141. Winkler, R. G.; Gold, M.; Reineker, P. Collapse of Polyelectrolyte Macromolecules by Counterion Condensation and Ion Pair Formation: A Molecular Dynamics Simulation Study. *Phys. Rev. Lett.* **1998**, 80, 3731.

142. Cassone, G.; Creazzo, F.; Giaquinta, P.V.; Saija, F.; Saitta, A.M.; Ab Initio Molecular Dynamics Study of an Aqueous NaCl Solution Under an Electric Field. *Phys. Chem. Chem. Phys.* **2016,** 18, 23164–23164.

143. Wright, M.R. An Introduction to Aqueous Electrolyte Solutions, Wiley, Chichester, UK, 2007.

144. Larentzos, J. P.; Criscenti, L. J.; A Molecular Dynamics Study of Alkaline Earth Metal−Chloride Complexation in Aqueous Solution. *J. Phys. Chem. B* **2008,** 112, 14243–14250.

145. Li, H.; Erbas¸ A.; Zwanikken, J.; Cruz, M. O. d. l. Ionic Conductivity in Polyelectrolyte Hydrogels, *Macromolecules* **2016**, 49, 9239−9246.

146. Heyden, F. H. J. v. d.; Stein, D.; Besteman, K.; Lemay, S. G.; Dekker., C. Charge Inversion at High Ionic Strength Studied by Streaming Currents. *Phys. Rev. Lett,* **2006**, 96, 224502.

147. Besteman, K.; Zevenbergen, M. A. G.; Lemay, S. G.; Charge Inversion by Multivalent Ions: Dependence on Dielectric Constant and Surface-charge Density. *Phys. Rev. E* **2005,** 72, 061501.

148. Krishnamoorthy, K.; Hoffmann, K.; Kewalramani, S.; Brodin, J. D.; Moreau, L. M.; Mirkin, C. A.; Cruz, M. O. d. l.; Bedzyk, M. J. Defining the Structure of a Protein−Spherical Nucleic Acid Conjugate and Its Counterionic Cloud, *ACS Cent. Sci.* **2018**, 4, 378−386.

149. Peng R.; Li, D. Electroosmotic Flow in Single PDMS Nanochannels, *Nanoscale* **2016**, 8, 12237–12246.

150. Shafiei, M.; von Domaros, M.; Bratko, D.; Luzar, A. Anisotropic Structure and Dynamics of Water Under Static Electric Fields. *J. Chem. Phys.* **2019** 150, 074505

151. Grossfield, A. WHAM: The Weighted Histogram Analysis Method, version 2.0.9, Grossfield lab website, University of Rochester (http://membrane.urmc.rochester.edu/content/wham).

152. Kumar, S.; Bouzida, D.; Swendsen, R. H.; Kollman, P. A.; Rosenberg, J. M. The Weighted Histogram Analysis Method for Free-Energy Calculations on Biomolecules. I. *The Method, J. Comput. Chem*. **1992**, 13, 1011–1021.

153. Chantiwas, R.; Park, S.; Soper, S. A.; Kim, B. C.; Takayama, S.; Sunkara, V.; Hwangc, H.; Cho, Y.-K. Flexible fabrication and applications of polymer nanochannels and nanoslits. *Chem. Soc. Rev.,* **2011**, 40, 3677–3702

154. Soozanipour, A.; Sohrabi, H.; Abazar, F.; Khataee, A.; Noorbakhsh, A.; Asadnia, M.; Kafrani, A. T.; Majidi, M. R.; Razmjou, A. Ion Selective Nanochannels: From Critical Principles to Sensing and Biosensing Applications. *Adv.Mater. Technol*.**2021**, 6, 2000765

155. Zhang, X.; Liu, H.; Jiang, L. Wettability and Applications of Nanochannels. *Adv.Mater.***2019**, 31, 1804508

156. Tagliazucchi, M.; Szleifer, I. Transport mechanisms in nanopores and nanochannels: can we mimic nature? *Materials Today***, 2015,** 18, 131-142

157. Gonella, G.; Backus, E. H. G.; Nagata, Y.; Bonthuis, D. J.; Loche, P.; Schlaich, A.; Netz, R. R.; Kühnle, A.; McCrum, I. T.; Koper, M. T. M.; Wolf, M.; Winter, B.; Meijer, G.; Campen, R. K.; Bonn, M. Water at charged interfaces. *Nat. Rev. Chem.* **2021**, 5, 466–485.

158. Li, J.; Peng, R.; Li, D. Effects of ion size, ion valence and pH of electrolyte solutions on EOF velocity in single nanochannels. *Anal. Chim. Acta,* **2019**, 1059, 68-79

159. Yu, J.; Mao, J.; Yuan, G.; Satija, S.; Chen, W.; Tirrell, M. The Effect of Multivalent Counterions to the Structure of Highly Dense Polystyrene Sulfonate Brushes. Polymer, **2016,** 98 448-453.

160. Liu, S.; Muthukumar, M. Langevin Dynamics Simulation of Counterion Distribution Around Isolated Flexible Polyelectrolyte Chains. *J. Chem. Phys.,* **2002** 116, 9975-9982

161. Chang, L.-W.; Lytle, T. K.; Radhakrishna, M.; Madinya, J. J.; Vélez, J.; Sing, C. E.; Perry, S. L. Sequence and Entropy-Based Control of Complex Coacervates. *Nat. Commun*. **2017**, 8, 1273.

162. Mintis, D.G.; Mavrantzas, V. G. Effect of pH and Molecular Length on the Structure and Dynamics of Short Poly(acrylic acid) in Dilute Solution: Detailed Molecular Dynamics Study. *J. Phys. Chem. B* **2019**, 123, 4204−4219.